Higher brightness beams from the SPS for the HL-LHC era

THÈSE N^O 7498 (2017)

PRÉSENTÉE LE 9 MARS 2017
À LA FACULTÉ SCIENCES DE BASE
LABORATOIRE DE PHYSIQUE DES ACCÉLÉRATEURS DE PARTICULES
PROGRAMME DOCTORAL EN PHYSIQUE

ÉCOLE POLYTECHNIQUE FÉDÉRALE DE LAUSANNE

POUR L'OBTENTION DU GRADE DE DOCTEUR ÈS SCIENCES

PAR

Francesco Maria VELOTTI

acceptée sur proposition du jury:

Prof. H. M. Rønnow, président du jury
Prof. L. Rivkin, Dr C. Bracco, directeurs de thèse
Dr R. Assmann, rapporteur
Dr V. Kain, rapporteuse
Dr M. Seidel, rapporteur

(EPFL
ÉCOLE POLYTECHNIQUE
FÉDÉRALE DE LAUSANNE

Suisse
2017

"Study hard what interests you the most
in the most undisciplined, irreverent
and original manner possible."
— Richard Feynman

Abstract

The need to push the LHC beyond its limits and increase the deliverable luminosity to the experiments by about one order of magnitude has driven the ongoing injector and HL-LHC upgrades. The higher luminosity requires to increase the beam brightness, which directly translates in the need to adapt the different machine protection systems. Among all the foreseen upgrades, the transfer line collimators (TCDI) and the LHC injection protection systems will be revised. In particular, the guaranteed protection is evaluated in this Ph D work, together with the specification for the minimum shielded aperture in case of injection failures. A detailed model is also developed which insures a more reliable and efficient procedure for the validation of the TCDI setup within the required accuracy.

The physics beyond colliders will also be pushed over its current limits in the HL-LHC era. SHiP, a new proposed fixed target experiment served by the SPS is under study. The unprecedented level of requested protons on target per year needs an assessment of the present SPS slow extraction. The main performance limitation of this technique is the activation of the area surrounding the extraction elements due to losses. The possibilities to optimise the present slow extraction as well as new ideas are investigated in order to preserve today's performances while reducing the extraction losses.

Key words: HL-LHC, SPS, injection, transport, extraction, slow extraction

Résumé

Le besoin de pousser le LHC au delà de ses limites et d'augmenter la luminosité fournie aux expériences d'au moins un ordre de grandeur a été le moteur de l'amélioration des injecteurs et HL-LHC. Une plus haute luminosité nécessite d'augmenter la brillance du faisceau, ce qui se traduit directement par le besoin d'adapter les différents systèmes de protection des machines. Parmi toutes les améliorations prévues, les collimateurs des lignes de transfert (TCDI) et les systèmes de protection des injections dans le LHC seront étudiés. En particulier, le niveau de protection garanti est analysé dans ce travail de thèse, ainsi que la spécification de l'ouverture minimale blindée en cas de problème d'injection. Un modèle détaillé est également développé, assurant une procédure plus fiable et plus efficace pour la validation de la configuration des TCDI avec la précision requise. La physique au delà des accélérateurs sera aussi poussée plus loin que ses limites actuelles dans l'ère du HL-LHC. SHiP, une nouvelle expérience à cible fixe alimentée depuis le SPS est actuellement au stade d'étude. Le niveau de protons sans précédent requis sur cible par an nécessite une évaluation de l'extraction lente actuelle du SPS. La principale limitation de performance de cette technique est l'activation de la zone avoisinant les éléments d'extraction due aux pertes. Les possibilités d'optimisation de l'actuelle extraction lente ainsi que de nouvelles idées sont étudiées dans le but de préserver les performances d'aujourd'hui tout en réduisant les pertes dues aux extractions.

Mots clefs : HL-LHC, SPS, injections, extraction, extraction lente

Contents

Contents

List of Figures

List of Tables

CHAPTER 1

Introduction

The Large Hadron Collider (LHC) at CERN (Conseil Europeen pour la Recherche Nucleaire) is the world's largest particle accelerator and the most powerful ever built, in terms of beam energy. Based on 3.5 and 4 TeV data accumulated in 2011 and 2012, ATLAS (A Toroidal LHC Apparatus) and CMS (Compact Muon Solenoid), two of the main experiments served by the LHC, announced the observation of a particle compatible with the Higgs boson, the cornerstone of the Standard Model (SM) of particle physics, on July 4th 2012.

After an upgrade campaign during a Long Shut-down (LS1) of more than two years, the LHC restarted in 2015 and operated at higher energy (6.5 TeV) and double intensity (3.7×10^{14} protons) than before LS1. The physics program after LS1 consists in investigating the properties of the Higgs boson, consolidating the validity of the SM and searching for new physics at higher energy frontiers.

The performance of a collider is usually quantified by its luminosity. For a Gaussian beam, the luminosity can be written as a combination of three terms:

$$\mathcal{L} = \frac{I_b^2 n_b}{\epsilon_N} \frac{F}{\beta^*} \frac{f_{rev}\gamma}{4\pi}, \tag{1.1}$$

where I_b is the intensity per bunch, n_b the number of bunches per beam, f_{rev} the revolution frequency, ϵ_N the normalised transverse emittance, β^* is the beta function at the interaction point and F is a geometric correction factor. Due to its direct dependence on the beam intensity and being inversely proportional to the beam beam size at the interaction points, the instantaneous luminosity scales linearly with the beam brightness ($B \equiv \frac{I_b n_b}{\sqrt{2(\epsilon_x^2 + \epsilon_y^2)}}$, for non-circular beams).

In the future, the LHC will then go through another major upgrade to push the luminosity, hence the collision rate, by about one order of magnitude beyond the design value of $\mathcal{L}$ = 1×10^{34} cm^{-2}s^{-1}. This will increase the chances to observe rare processes, improve statistically marginal measurements and in general extend the LHC discovery potential. This High-Luminosity LHC (HL-LHC) upgrade requires substantial changes in the full

chain of the LHC injectors. The aim is to inject beams into the LHC with a brightness of $3.1 \times 10^{13}\,\mathrm{p(mm\,mrad)}^{-1}$ (2.3×10^{11} protons per bunch, $2.1\,\mathrm{mm\,mrad}$ transverse normalised emittance), a factor of two higher than the present maximum achieved. All the injectors need to be upgraded to reach the foreseen beam characteristics and an LHC Injector Upgrade (LIU) program has already started.

In order to reach the HL-LHC peak luminosity target of $7.5 \times 10^{34}\,\mathrm{cm}^{-2}\,\mathrm{s}^{-1}$, many limitations have to be be overcome. The LIU program will help to increase the first term of Eq. (1.1), while the HL-LHC upgrade is focused on the optimisation of the optics related term (F/β^*). Both LIU and HL-LHC comprise upgrades to withstand the higher beam brightness.

In the context of LIU, the reduction of the beam induced impedance in the SPS is one of the main upgrades to undertake. Impedance driven longitudinal instabilities are one of the main limitations to the beam brightness presently achievable in the SPS. The fast pulsed magnets (kickers), distributed along the SPS circumference, represent 40% of the total longitudinal impedance budget [1]. In order to have the possibility to remove one full set of extraction kicker, a new concept of extraction (*non-local* extraction[2]) is being studied; this would allow extracting both LHC beams with the same SPS kickers and thus reduce the machine impedance by about 7%. As the instabilities are general threshold effects this could be significant for the overall performance [3]. Feasibility studies of this non-local extraction concept are presented in this thesis, based on tracking simulations. Experimental results are presented for different SPS configurations.

Two $3\,\mathrm{km}$ long transfer lines (TL) transport the beam from the SPS to the LHC injection. The high brightness HL-LHC beams represents a machine protection challenge due to the high energy stored in the beam (up to $5\,\mathrm{MJ}$ per transfer, 30 times higher than the damage limit of the accelerator components). Each TL is presently equipped with six $1.2\,\mathrm{m}$ long collimators (TCDI) located at a well-defined phase advances, together with a set of injection protection collimators in the LHC ring itself, to protect the LHC aperture from particles injected with dangerously large amplitudes. A new TCDI design is required for the HL-LHC beams, together with a new optics and different TCDI locations [4]. An accurate setup (at $50\,\mu\mathrm{m}$ level) of the collimators is also needed to guarantee the required protection, and reliable and relatively fast procedure is needed to validate the overall system settings with the beam. In this thesis, the problem of evaluating the effective minimum protected aperture in case of an injection failure and the proposed new designs of the injection protection devices were addressed with tracking simulations. Beam measurements of the current LHC injection system were used to benchmark the simulation results. The existing set-up validation procedure of the TCDIs was also revised, improvements implemented and tested with beam.

In addition to the well-established LHC and HL-LHC experimental program, the future of CERN's non-collider program is also being defined [5]. In this context the SHiP

experiment [6], has been proposed at CERN. The focus of this proposal is to investigate the existence of three Heavy Neutral Leptons (HNL) to give experimental proof to the neutrino minimal Standard Model (νMSM) [7, 8] theory. High-intensity slow-extraction of $400\,\text{GeV}$ protons from the SPS is a pre-requisite for SHiP, but beam losses and activation of the SPS electrostatic extraction septum (ZS) could be a serious performance limitation. In fact, the number of protons to extract per year is a factor of two higher than ever achieved before in the SPS and a factor of four than ever reached with the third-integer slow extraction. Methods to reduce the losses during the extraction process are required, and theoretical and experimental studies on this topic are presented in this thesis. The SPS slow extraction was reviewed and a model for particle tracking was built and benchmarked with beam measurements. A new technique to significantly reduce the losses at the septum is presented, based on bent silicon crystals to channel the beam away from the ZS wires, together with theoretical concepts and a possible layout for beam tests.

CHAPTER 2

Single Particle Beam Dynamics

In this chapter, the basic of accelerator physics that will be used in this thesis are presented. The attention will be focused on transverse motion and the formalism used in literature for its description.

The content of this chapter is based on references [9, 10, 11, 12], unless explicitly specified.

2.1 Transverse motion

The motion of a charged particle in an accelerator can be described by the second law of dynamics and the *Lorentz force* when their relativistic vectors are conserved:

$$\vec{F} = m\vec{a} = \frac{d\vec{p}}{dt} = q(\vec{E} + \vec{v} \times \vec{B}). \tag{2.1}$$

Here, q is the particle charge and m its mass, $\vec{a}$, $\vec{p}$ and $\vec{v}$ are the acceleration, momentum and velocity respectively, and $\vec{E}$ and $\vec{B}$ are the electric and magnetic field. In general electric and magnetic fields are used to accelerate and guide particles, respectively (mainly for relativistic beams, $v \approx c$, which c speed of light in vacuum).

The beam dynamics is defined as the evolution of particle trajectories due to the influence of Lorentz forces. When the fields are independent or linearly dependent from particular particle position with respect to the ideal orbit, the formal description is known as *linear beam dynamics*. When this does not hold, one refers to as *non-linear beam dynamics*.

In order to describe the motion of the beam inside the accelerator, a local reference system with respect to the nominal machine orbit is needed (Fig. 2.1). Here s represents the longitudinal coordinate, $\hat{x}$ and $\hat{y}$ the transverse plane and ρ the local bending radius. In order to keep charged particles on the design orbit, magnetic fields deflect them as needed. This can be formally written as the balance of the centrifugal and the Lorentz force:

$$m\gamma v^2 \vec{k} + e[\vec{v} \times \vec{B}] = 0 \tag{2.2}$$
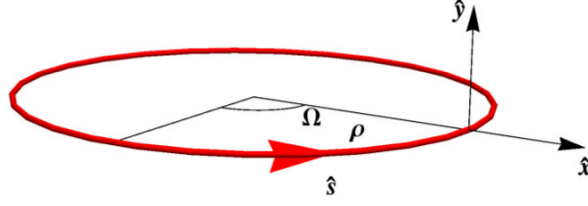
Figure 2.1 – Curvilinear coordinate system used for the description of transverse particle motion.

where $\vec{k} = (\frac{1}{\rho_x}, \frac{1}{\rho_y}, 0)$. Considering $\vec{B}$ perfectly orthogonal to the particle velocity $\vec{v}$, and that the transverse velocities are much smaller then the longitudinal one ($\vec{v_x} \ll \vec{v_s}$, $\vec{v_y} \ll \vec{v_s}$, $\vec{v_z} \equiv \vec{v_s}$), the bending radius can be isolated as:

$$\frac{1}{\rho} = \left| \frac{e}{p} B \right| \tag{2.3}$$

where $p = \gamma m c \beta$, with γ and β relativistic factors. Rearranging Eq. (2.3), the *magnetic beam rigidity* can be defined as $|B\rho| = \frac{p}{e}$.

In the curvilinear reference system of Fig. 2.1, the Hamiltonian for a relativistic particle under the influence of external magnetic field can be written as:

$$H(x, p_x, y, p_y, t, -E; s) = - \left(1 + \frac{x}{\rho} \right) \left[\sqrt{ \frac{E^2}{c^2} - m^2 c^2 - (p_x - qA_x)^2 - (p_y - qA_y)^2 } + qA_s \right] \tag{2.4}$$

with the components of the vector potential defined as $A_x(s)$, $A_y(s)$ and $A_s(s)$. The usual choice of the conjugate phase space variables was made:

- Horizontal displacement from the Closed Orbit (CO) x and corresponding momentum component p_x;

- Vertical displacement from the CO y and corresponding momentum component p_y;

- Time t and total energy E.

Due to the much smaller transverse momenta with respect to the total momentum,

Eq. (2.4) can be expanded to the second order in p_x and p_y:

$$H \approx - \left(1 + \frac{x}{\rho}\right) \left[p - \frac{(p_x - qA_x)^2 + (p_y - qA_y)^2}{2p} + qA_s\right], \tag{2.5}$$

where the H dependence from the conjugate phase space variables has been dropped only for simplicity.

For the assumption of having only transverse magnetic fields, $A_x = A_y = 0$, hence:

$$A_s = -B_0 \mathcal{R} \left[\sum_{n=0}^{\infty} \frac{b_n + ja_n}{n+1} (x + jy)^{n+1}\right] \tag{2.6}$$

where $\mathcal{R}[...]$ represents the real part and B_0 is the normalisation constant usually chosen as the main dipole field strength. In this way $B_0 b_0 = -(B\rho)/\rho$. The magnetic field can be expressed as the curl of the vector potential $\vec{B} = \nabla \times \vec{A}$, hence:

$$B_x = \frac{\partial A_s}{\partial y}, \qquad B_y = -\frac{\partial A_s}{\partial x}. \tag{2.7}$$

The latter can be rewritten in complex representation, yielding:

$$B_y(x,y) + jB_x(x,y) = B_0 \sum_{n=0}^{\infty} (b_n + ja_n)(x + jy)^n. \tag{2.8}$$

The normal, b_n, and the skew, a_n, components of the field can then be defined as:

$$a_n = \frac{1}{B_0 n!} \frac{\partial^n B_x}{\partial x^n}\bigg|_{x=y=0}, \qquad b_n = \frac{1}{B_0 n!} \frac{\partial^n B_y}{\partial x^n}\bigg|_{x=y=0}. \tag{2.9}$$

2.1.1 Linear beam dynamics

The Hamilton's equations are defined as

$$x' = \frac{\partial H}{\partial p_x}, \ p_x' = -\frac{\partial H}{\partial x}, \qquad y' = \frac{\partial H}{\partial p_y}, \ p_y' = -\frac{\partial H}{\partial y}, \tag{2.10}$$

where the prime sign indicates the total derivative with respect to s. Neglecting the synchrotron motion (much slower than the betatron one) and using the Hamiltonian derived in Eq. 2.5 with Eq. (2.10) and Eq. 2.7, the general betatron equation of motion can be written as:

$$x'' - \frac{\rho + x}{\rho^2} = -\frac{B_y}{B\rho} \frac{p_0}{p} \left(1 + \frac{x}{\rho}\right)^2,$$
$$y'' = \frac{B_x}{B\rho} \frac{p_0}{p} \left(1 + \frac{x}{\rho}\right)^2. \tag{2.11}$$

Here the higher-order terms have been neglected, $B\rho = p_0/q$ and p_0 is the momentum of the synchronous particle. Expanding the magnetic filed equations up to the first order, the Eq. (2.11) can be rewritten as the transverse linear equation of motion:

$$x'' + \left(\frac{1 - \delta_p}{\rho^2(1 + \delta_p)} + \frac{K_1(s)}{1 + \delta_p} \right) x = \frac{\delta_p}{\rho(1 + \delta_p)},$$
$$y'' - \left(\frac{K_1(s)}{1 + \delta_p} \right) y = 0, \tag{2.12}$$

where $K_1(s) = B_1/(B\rho)$ is the local normalised quadrupole gradient and $\delta_p \equiv \Delta p/p_0$ is the fractional momentum offset of a single particle. Also, the implicit assumptions that the dipole fields defines a closed orbit, i.e. $B_0/B\rho = 1\,\rho$, and that there are only horizontal dipoles have been made.

The solution to the inhomogeneous equation of motion has the form:

$$u(s) = u_{CO}(s) + u_\beta(s) + D_u(s)\delta_p, \tag{2.13}$$

where u represents one of the two transverse coordinates x or y, u_{CO} is the beam closed orbit, $x_\beta(s)$ is the solution of the associated homogeneous equation and $D_u\delta_p$ is the particular solution. Here, the *dispersion function $D_u(s)$* has been introduced. Thus $x_\beta(s)$ and $D_u(s)\delta_p$ satisfy the equations:

$$x_\beta'' + (K_u(s) + \Delta K_u)x_\beta = 0 \tag{2.14a}$$

$$D_u(s)'' + (K_u(s) + \Delta K_u)D_u = \frac{1}{\rho} + \mathcal{O}(\delta_p^2), \tag{2.14b}$$

where $K_u \equiv 1/\rho^2 + K_1(s)$ and $\Delta K_u(s) = [-\frac{2}{\rho^2} - K_1(s)]\delta_p + \mathcal{O}(\delta_p^2)$.

Solution of Hill's equations

The homogeneous equation of motion ($\delta_p = 0$) can be expressed as the well-known Hill's equations:

$$x'' + K_x(s)x = 0$$
$$y'' + K_y(s)y = 0. \tag{2.15}$$

Since $K_u(s)$ is a periodic function, the Floquet's theorem can be used and the solution of Eq. (2.15) can be expressed as a pseudo-harmonic oscillation:

$$u(s) = \sqrt{2J_u\beta_u(s)}\cos(\psi_u(s) - \psi_{u,0}),$$
$$u'(s) = -\sqrt{\frac{2J_u}{\beta_u(s)}}[\sin(\psi_u(s) - \psi_{u,0}) + \alpha_u(s)\cos(\psi_u(s) - \psi_{u,0})], \tag{2.16}$$
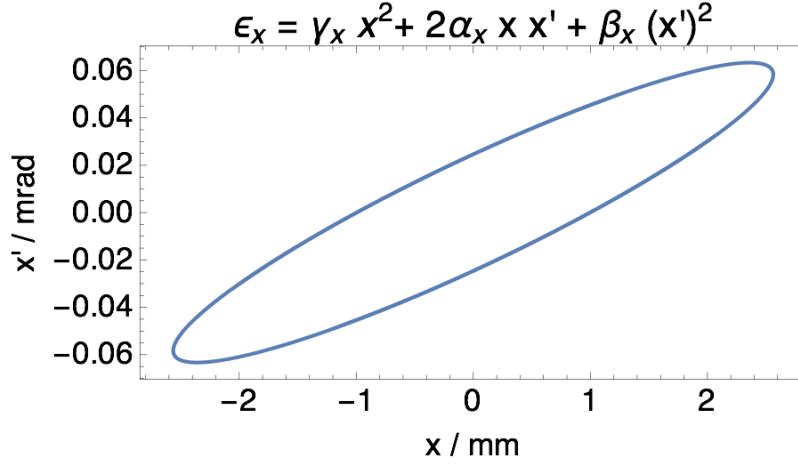
Figure 2.2 – Example of trajectory in trace-space.

where J_u is the invariant action, $\psi_{u,0}$ is the phase offset and α_u, β_u, ψ_u are the Courant-Snyder parameters. More explicitly β_u is the amplitude function (or β-function), $\alpha_u = -\beta_u'(s)/2$ represents the beam divergence and $\psi_u = \int_0^s \frac{1}{\beta_u(\tau)} d\tau$ is the betatron phase advance. Under these assumptions, the motion in trace space (u, u') is an ellipse of area $2\pi J_u$, as shown in Fig 2.2. From the general equation of an ellipse, the Courant-Snyder invariant is defined as

$$\epsilon_u \equiv 2J_u = \frac{1}{\beta_u} \left[u^2 + (\alpha_u x + \beta_u u')^2 \right] = \gamma_u u^2 + 2\alpha_u u u' + \beta_u u'^2, \tag{2.17}$$

where $\gamma_u \equiv \frac{1+\alpha_u^2}{\beta_u}$ and the explicit dependence on s has been dropped. Eq. (2.17) also defines the *single particle emittance*, where its parametric form is defined in Eq. (2.16). From the definition of β-function and phase advance, the betatron tune is introduced. It is defined as the number of betatron oscillations per machine revolution:

$$Q_u = \nu_u \equiv \frac{1}{2\pi} \oint \frac{1}{\beta_u(s)} ds. \tag{2.18}$$

It can be proved that Hill's equations can be solved and put in the form of a transfer matrix for each machine element. In this way, the betatron state-vector, $\vec{u}(s) = \begin{pmatrix} u \\ u' \end{pmatrix}$ can be calculated at any location knowing the initial conditions (at s_0) and the transfer matrix of the element $M(s|s_0)$:

$$\vec{u}(s) = M(s|s_0)\vec{u}(s_0). \tag{2.19}$$

Thanks to the Courant-Snyder formalism, a matrix that transforms the transverse phase space coordinates from one location s_1 of a generic accelerator (circular or beam-line) to

another location s_2 can be written as:

$$M(s_2|s_1) = \begin{pmatrix} \sqrt{\frac{\beta_2}{\beta_1}}(\cos(\Delta\psi) + \alpha_1\sin(\Delta\psi)) & \sqrt{\beta_1\beta_2}\sin(\Delta\psi) \\ -\frac{1+\alpha_1\alpha_2}{\sqrt{\beta_1\beta_2}}\sin(\Delta\psi) + \frac{\alpha_1-\alpha_2}{\sqrt{\beta_1\beta_2}}\cos(\Delta\psi) & \sqrt{\frac{\beta_1}{\beta_2}}(\cos(\Delta\psi) - \alpha_2\sin(\Delta\psi)), \end{pmatrix}$$

(2.20)

where the subscript 1 and 2 refer to the s_1 and s_2 locations, respectively and $\Delta\psi = \psi(s_2) - \psi(s_1)$.

Solution for off-momentum particles

For an off-momentum particle ($\delta_p \neq 0$), the solution of the traverse equation of motion is given by Eq. (2.13) and the particular solution $D_u(s)\delta_p$ satisfies the Eq. (2.14b). Neglecting now the chromatic perturbation term $\Delta K_u(s)$ and assuming that the bending magnets are only on the horizontal plane, the inhomogeneous equation for the dispersion function is written as:

$$D_x(s)'' + K_x(s)D_x(s) = \frac{1}{\rho}.$$

(2.21)

The solution of the latter will be composed by a particular and general solution. This can be written using the matrix formalism:

$$\begin{pmatrix} D_x(s_2) \\ D'_x(s_2) \\ 1 \end{pmatrix} = \mathcal{M}_x \begin{pmatrix} D_x(s_1) \\ D'_x(s_1) \\ 1 \end{pmatrix}$$

(2.22)

where

$$\mathcal{M}_x \equiv \begin{pmatrix} M_x(s_2|s_1) & \bar{d}_x \\ 0 & 1 \end{pmatrix}$$

(2.23)

and $\bar{d}_x$ is the vector representing the particular solution of Eq. (2.21).
Once the dispersion, and its derivative, are know, they can be put together with Eq. (2.20) as an additional column to obtain the actual particle displacement from the closed orbit.

Linear imperfections: dipole error

In order to evaluate the effect of linear magnet imperfections on the beam closed orbit, the Hill's equations can be rewritten adding a forcing term $\mp\frac{\Delta B_{y,x}}{B\rho}$, for x and y respectively, where $\Delta B_{x,y}$ is the magnetic field error of the form of Eq. (2.8).
For the case of a dipole field error $\theta = \Delta B dl/(B\rho)$ (with $\Delta B dl$ integrated field error) at a location s_0, the phase space coordinates (assuming an horizontal dipole) at the location

of the error are:

$$s_0^- \Rightarrow \begin{pmatrix} x_0 \\ x_0' - \theta \end{pmatrix}; \qquad s_0^+ \Rightarrow \begin{pmatrix} x_0 \\ x_0' \end{pmatrix}. \tag{2.24}$$

Imposing the closed orbit condition, i.e.

$$\begin{pmatrix} x_0 \\ x_0' - \theta \end{pmatrix} = M_{1\ turn} \begin{pmatrix} x_0 \\ x_0' \end{pmatrix} \tag{2.25}$$

the resulting particle phase space coordinates at s_0 are:

$$\begin{aligned} x_0 &= \frac{\beta_0 \theta}{2\sin(\pi\nu_x)} \cos(\pi\nu_x) \\ x_0' &= \frac{\theta}{2\sin(\pi\nu_x)} (\sin(\pi\nu_x) - \alpha_0 \cos(\pi\nu_x)). \end{aligned} \tag{2.26}$$

From the last equation is worth to notice that for ν_x integer there is a pole and this explains why integer working points (tunes) shall be avoided.

From Eq. (2.26), using the transport matrix defined in Eq. (2.20), the particle coordinates can be calculated anywhere in the machine. For more than one error and assuming them to be distributed all along the ring, the closed orbit $x_{CO}(s)$ at a generic location s can be calculated as:

$$x_{CO}(s) = \frac{\sqrt{\beta_x(s)}}{2\sin(\pi\nu_x)} \int_s^{s+C} \sqrt{\beta_x(\hat{s})} \frac{\Delta B(\hat{s})}{B\rho} \cos(\pi\nu_x + \psi_x(s) - \psi_x(\hat{s})) d\hat{s}. \tag{2.27}$$

To be noted that a dipole kick can also be obtained due to magnet misalignment via feed-down effects. For instance, a misaligned quadrupole can kick the beam by

$$\theta_q = K_u L \Delta u \tag{2.28}$$

where Δu is the displacement of the element on the u coordinate, K_u is the normalised quadrupole gradient and L is the element length.

Particle distributions

A particle beam is described using probability distributions. The most common way to treat particle beams is to use normal distributions in all transverse degrees of freedom. Defining a generic 2D probability density function (pdf) $f(u, u')$ such that

$\int_u \int_{u'} f(u, u') du du' = 1$, the first moments of the beam distribution can be calculated as:

$$\langle u \rangle = \int_u \int_{u'} u f(u, u') du du'; \tag{2.29a}$$

$$\langle u' \rangle = \int_u \int_{u'} u' f(u, u') du du'; \tag{2.29b}$$

$$\sigma_u^2 = \int_u \int_{u'} (u - \langle u \rangle)^2 f(u, u') du du'; \tag{2.29c}$$

$$\sigma_{u'}^2 = \int_u \int_{u'} (u' - \langle u' \rangle)^2 f(u, u') du du'; \tag{2.29d}$$

$$\sigma_{u,u'}^2 = \int_u \int_{u'} (u - \langle u \rangle)(u' - \langle u' \rangle) f(u, u') du du'. \tag{2.29e}$$

Here Eq. (2.29a, 2.29b) represent the averages, σ_u and $\sigma_{u'}$ the standard deviations (which also define the rms beam sizes) of the marginal distributions, and $\sigma_{u,u'}$ the correlation. From these quantities, the rms beam geometrical emittance can be calculated as:

$$\epsilon_u = \sqrt{\sigma_u^2 \sigma_{u'}^2 - \sigma_{u'}^2} = \epsilon_{N,u}/(\beta\gamma) \tag{2.30}$$

where the normalised emittance $\epsilon_{N,u}$ has been introduced.

2.1.2 Normalised coordinates

The general transport matrix given by Eq. (2.20) permits to evaluate the phase space coordinates at any machine location. It can be demonstrated that $M(s_2|s_1)$ can be decomposed as:

$$M(s_2|s_1) = B(s_2)R(s_2|s_1)B^{-1}(s_1) \tag{2.31}$$

where $R(s_2|s_1)$ is a rotation matrix of angle $\Delta\psi = \psi(s_2) - \psi(s_1)$ and $B(s)$ is the betatron amplitude matrix. Using Eq. (2.31) to rewrite Eq. (2.19) and rearranging the left and right hand side, this yields

$$B^{-1}(s_2)\vec{u}(s_2) = R(s_2|s_1)B^{-1}(s_1)\vec{u}(s_1), \tag{2.32}$$

where

$$B^{-1}(s) = \begin{pmatrix} \frac{1}{\sqrt{\beta(s)}} & 0 \\ \frac{\alpha(s)}{\sqrt{\beta(s)}} & \sqrt{\beta(s)} \end{pmatrix}. \tag{2.33}$$

Once the phase space coordinates are normalised with Eq. (2.33), the trajectories of particles in transverse phase space change from ellipses to circles (Fig. 2.3). In this thesis, the normalised transverse coordinates are identified with capitol letters or with a bar,
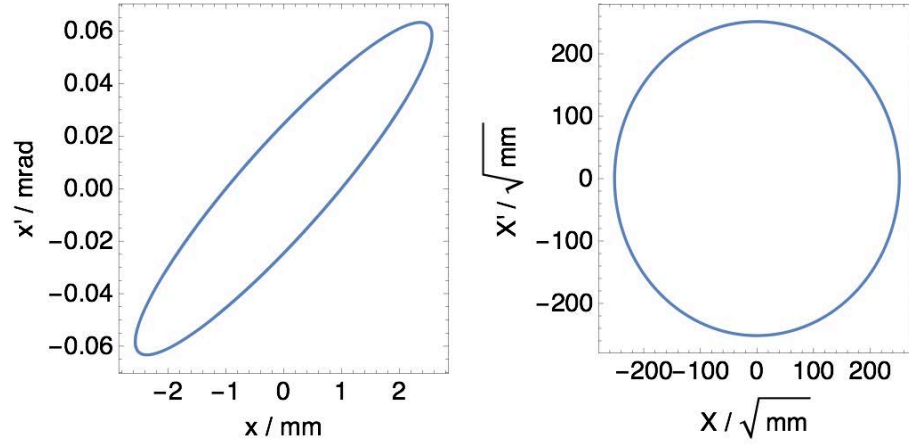
Figure 2.3 – Trace-space (left) compared with normalised phase-space (right).

e.g.:

$$\bar{x}(s) = \frac{x(s)}{\sqrt{\beta_x(s)}} \qquad \bar{x}'(s) = \frac{\alpha_x(s)x(s) + \beta_x(s)x'(s)}{\sqrt{\beta_x(s)}} \tag{2.34}$$

represent the normalise transverse horizontal coordinates.

Action-angle variable

A further transformation can be made to the normalised transverse coordinates, Eq. (2.34), to be able to write the Hamiltonian of our transformation in a much simpler way. The new coordinates system, the so-called action-angle variable is suited for harmonic oscillators as for charged particles in a strong focusing regime. The aim is to transform the normalised phase space coordinates $(\bar{x}, \bar{x}')$, with independent variable ψ, into (J, ψ).
The normalised phase space coordinates can be written as:

$$\begin{aligned}
\bar{u} &= \sqrt{2J_u}\cos(\psi - \phi); \\
\bar{u}' &= \sqrt{2J_u}\,sin(\psi - \phi),
\end{aligned} \tag{2.35}$$

where ϕ is an arbitrary phase. Solving for J_u and ψ_u the new action-angle description of particle motion can be derived. In these new coordinate system, the Hamiltonian for linear motion in an accelerator can be simply written as:

$$H = \nu_x J_x + \nu_y J_y. \tag{2.36}$$

Due the independence of the latter to the betatron phase, the action J_u results to be an invariant of motion (when applying the first Hamilton's equation Eq. (2.10)), as previously stated. Applying the second of Hamilton's equations, the frequency of the

oscillator is obtained:

$$\frac{\partial H}{\partial J_u} = \dot{\psi} = \nu_u,$$
(2.37)

this is indeed the transverse tune, as expected.

2.1.3 Non-linear beam dynamics

Chromaticity

The term that accounts for chromatic aberrations in Eq. (2.14b), which was previously neglected, is defined, for the two transverse planes respectively, as:

$$\Delta K_x(s) = -[\frac{2}{\rho^2} - K_1(s)]\delta_p + \mathcal{O}(\delta_p^2) \approx -K_1(s)\delta_p;$$
$$\Delta K_y(s) = K_1(s)\delta_p + \mathcal{O}(\delta_p^2) \approx K_1(s)\delta_p.$$
(2.38)

Essentially, the non-ideal momentum of a particle can be seen as an individual gradient error. This then translates in a tune shift, which can be calculated as:

$$\Delta\nu_u = \frac{1}{4\pi} \oint \beta_u(s)\Delta K_u(s)ds.$$
(2.39)

From the latter, the chromaticity is defined as the derivative of the transverse tune with respect to the momentum offset:

$$Q'_u = \frac{d\Delta\nu_u}{d\delta_p}.$$
(2.40)

Then, the *normalised chromaticity* is defined as:

$$\xi_u \equiv Q'_u/\nu_u$$
(2.41)

and it has a value of about 1 for a FODO lattice.

Eq. (2.39) agrees with the intuitive view that particles with larger momentum (higher rigidity) have smaller transverse tune, in fact the tune shift originated from the lattice quadrupoles is negative.

Sextupoles are mainly used to correct chromaticity. Due to the quadrupole feed-down effect created when particles with a CO different from zero pass through a sextupole, the tune of such particles is changed. This can be done in regions where the dispersion in non-zero exploiting the proportionality of the CO displacement with the momentum difference. Form the relations of the magnetic field of a sextupole and Eq. (2.13), assuming

$u_{CO} = 0$, the chromaticity for the two transverse planes can be written as:

$$
\begin{aligned}
Q'_x &= -\frac{1}{4\pi} \oint \beta_x [K_1(s) - K_2(s)D_x] ds, \\
Q'_y &= \frac{1}{4\pi} \oint \beta_y [K_1(s) - K_2(s)D_x] ds.
\end{aligned}
\tag{2.42}
$$

In the last equation is shown formally the reason why sextupoles placed in dispersive regions can be used to correct the chromaticity.

Sextupoles can also be used for other purposes, like slow extraction. In the next chapter, the use of strong sextupoles placed in non-dispersive regions to excite third-integer resonance for extraction proposes is shown.

Lie transformations

The matrices, which are used in linear dynamics to transform the set of transverse coordinates, cannot be used any more in a non-linear regime. In this case, maps need to be used for the transport of the transverse beam coordinates. The so-called *Hamiltonian resonance driving terms* can be calculated using perturbation theory.

The one-turn map in normalised coordinates for a linear accelerator is a simple rotation $\mathcal{R}$. To generalise this to the non-linear case, the assumption that all the non-linear thin kicks are evaluated all together and only once at the beginning of the machine can be made. This permits to write the one-turn non-linear map as:

$$
\mathcal{M} = e^{:h:} \mathcal{R},
\tag{2.43}
$$

where $e^{:h:}$ is a *Lie transformation* and h is the generator of the transformation. The Lie transformation is defined as the exponential of the Lie operator:

$$
e^{:f:} = \sum_{n=0}^{\infty} \frac{1}{n!} (: f :)^n
\tag{2.44}
$$

with the Lie operator defined as:

$$
: f :\, \equiv [f,] \Rightarrow\, : f : g = [f, g]
\tag{2.45}
$$

and

$$
[f, g] = \sum_{i=1}^{N} \left[\frac{\partial f}{\partial u_i} \frac{\partial g}{\partial p_{u,i}} - \frac{\partial f}{\partial p_{u,i}} \frac{\partial g}{\partial u_i} \right]
\tag{2.46}
$$

being the Poisson bracket. Such notation is very handy because particle coordinates can

be transported trough one element using the Lie transformation, i.e.

$$u(s_2) = e^{:f:}u(s_1), \qquad p_u(s_2) = e^{:f:}p_u(s_1), \tag{2.47}$$

where the generating function f is related to the Hamiltonian H of the element as $f = -LH$.

Thanks to this formalism, multiple elements can be put together just by multiplying the Lie transformations of each of them. This leads to the one-turn map including non-linear elements. For example, when away from a resonance and assuming that the non-linearities are distributed all along the machine, an *effective Hamiltonian* h_{eff} can be written. For example, truncating at the third order, the effective Hamiltonian can be written as:

$$
\begin{aligned}
h_{eff} = \nu_x J_x + \nu_y J_y + \frac{1}{2}\alpha_c \delta_p^2 + Q_x' J_x \delta_p + Q_y' J_y \delta_p + c_3 \delta^3 + \\
c_{xx} J_x^2 + c_{xy} J_x J_y + c_{yy} J_y^2 + c_{x2} J_x \delta_p^2 + c_{y2} J_y \delta_p^2 + c_4 \delta_p^4
\end{aligned}
\tag{2.48}
$$

and used to generate the transport map of the particle coordinates over one machine revolution as $e^{-:h_{eff}(J_x, J_y, \delta_p):}$. In the Eq (2.48), the physical meanings of the different coefficients (apart from the one already introduced) are:

- α_c, c_3 and c_4: linear and non-linear *momentum compactions* (see next section);

- c_{x2} and c_{y2}: second order chromaticities;

- c_{xx}, c_{xy}, c_{yy}: detuning with amplitude coefficients.

Non linear resonances

Non linear element contributions can be introduced in the transverse motion treatment as a perturbation of the Hamiltonian describing the transverse dynamics. For example, a sextupole in an otherwise linear lattice leads to:

$$H = \frac{1}{2}[x'^2 + K_x x^2 + y'^2 + K_y y^2] + V_3(x, y, s) \tag{2.49}$$

where $V_3(x, y, s) = \frac{1}{6}S(s)(x^3 - 3xy^2)$ is the perturbation of the linear Hamiltonian. Here, $S(s) = \frac{1}{(1+\delta_p)B\rho} \frac{\partial^2 B_y}{\partial x^2}\Big|_{x=y=0}$ with $\delta_p = 0$ for this specific case. A very simple and immediate way to see the effect of a sextupole on the beam dynamics is to include it as a single perturbation of the linear equation of motion. The effect of a sextupole on the transverse coordinates is:

$$\Delta x' = -\frac{1}{2}Sdl(x^2 - y^2); \qquad \Delta y' = Sdlxy. \tag{2.50}$$

Tracking particles with different amplitudes in a perfect linear accelerator plus a sextupole originates the Poincaré map $(\bar{x}, \bar{x}')$ as shown in Fig. 2.4 for different horizontal working points. The phase space is significantly distorted when a non linear element is introduced and the betatron oscillation frequency is close to a resonance. To note here is the effect of a sextupole when the tune goes closer to the third integer resonance. The stable area in phase space shrinks when the tune goes closer to an integer multiple of one third. Such specific case, due to the order of the resonance (the lower the faster particles become unstable), is also used in many accelerator facilities to continuously extract particles form a synchrotron.
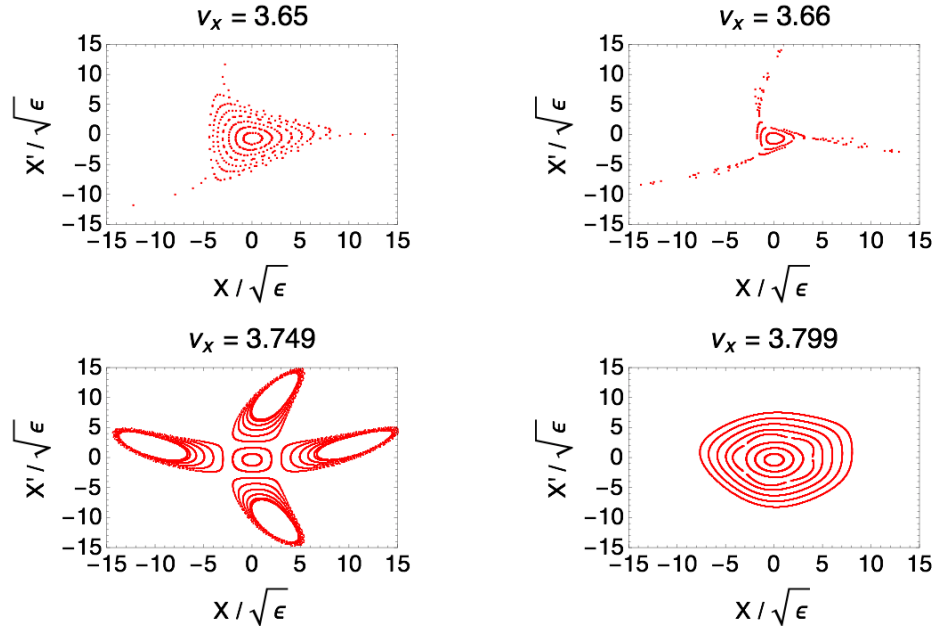
Figure 2.4 – Normalised horizontal phase-space portraits for a perfectly linear machine with a sextupole ($S_x = 0.5\,\mathrm{m}^{-2}$) and for four different tunes.

The tracking results shown in Fig. 2.4 can be plotted in action-angle variables to see how the action changes, and hence it is not an invariant of the motion anymore (Fig. 2.5). This is very specific for sextupoles, although such a procedure can be easily extended to higher order multipoles. The treatment of higher order elements will not be covered in this introduction.

The third order resonance can be described analytically transforming the perturbation term introduced in Eq. (2.49) in action-angle:

$$V_3 = -\frac{\sqrt{2}}{4} J_x^{1/2} J_y \beta_x^{1/2} \beta_y S(s)[2\cos(\psi_x) + \cos(\psi_x + 2\psi_y) + \cos(\psi_x - \psi_y)] + \frac{\sqrt{2}}{12} J_x^{3/2} \beta_x^{3/2} S(s)[\cos(3\psi_x) + 3\cos(\psi_x)]. \tag{2.51}$$

17
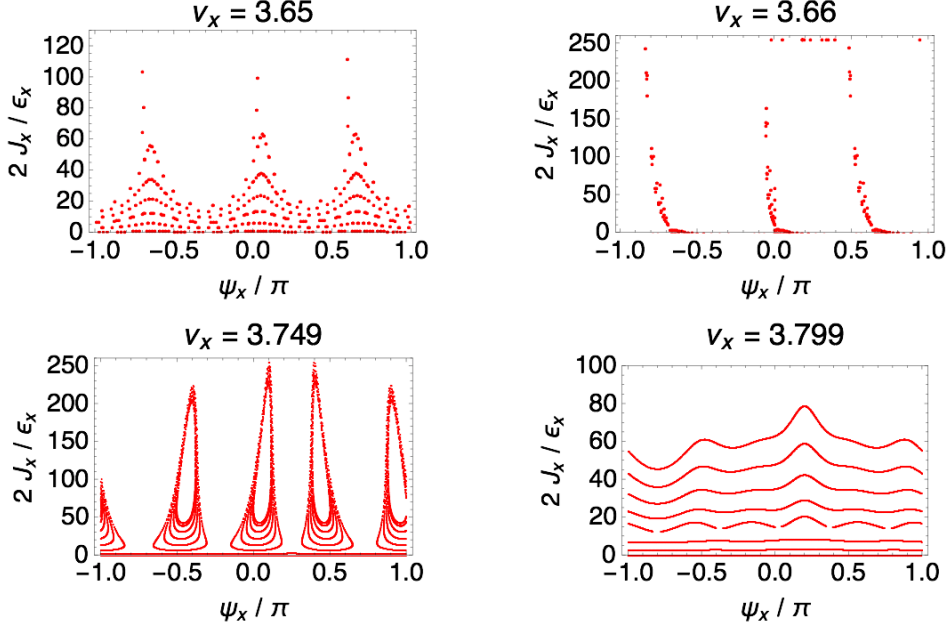
Figure 2.5 – Examples of action-angle space of Fig. 2.4.

Due to the periodicity of V_3 with s, it can be expanded in Fourier harmonics. Substituting the Eq. (2.51) in the Hamiltonian in Eq. (2.49) and expressing everything in action-angle variable, it yields:

$$
\begin{aligned}
H =&\nu_x J_x + \nu_y J_y + \sum_p G_{3,0,p} J_x^{3/2} \cos(2\psi_x - p\Omega + \zeta_{3,0,p})+ \\
&\sum_p G_{1,2,p} H_{1,2,p} J_x^{1/2} J_y \cos(\psi_x + 2\psi_y - p\Omega + \zeta_{1,2,p})+ \\
&\sum_p G_{1,-2,p} H_{1,-2,p} J_x^{1/2} J_y \cos(\psi_x - 2\psi_y - p\Omega + \zeta_{1,-2,p}) + \dots
\end{aligned}
\tag{2.52}
$$

where p is an integer that satisfies $n\nu_x + m\nu_y = p$ with m and n integers as well, $G_{n,m,p}$ and $\zeta_{n,m,p}$ are the Fourier amplitudes and phases of the Fourier components, $\Omega = s/R$ is the orbiting angle (R machine radius). The expansion has been truncated for brevity. The Hamiltonian near the third order resonance, $3\nu_x = p$, can be approximated as:

$$
H \approx \nu_x J_x + G_{3,0,p} J_x^{3/2} \cos(3\psi_x - p\Omega + \zeta_{3,0,p}).
\tag{2.53}
$$

The Fourier amplitude and phase are:

$$
G_{3,0,p} e^{j\zeta_{3,0,p}} = \frac{\sqrt{2}}{24\pi} \oint \beta_x^{3/2} S(s) e^{j[3\psi_x(s) - (3\nu_x - p)\Omega]} ds.
\tag{2.54}
$$

The Hamiltonian of Eq. (2.53) is now directly dependent from the phase advance, and hence the action is not an invariant any more. The transverse phase space will be distorted

by the non-linear resonance and the magnitude of such a distortion is proportional to the resonance strength $G_{3,0,p}$.

The Hamiltonian in Eq. (2.53) can be transformed in a new phase space

$$\psi = \psi_x - \frac{p}{3}\Omega + \frac{\zeta}{3}, \qquad J = J_x \tag{2.55}$$

using the generating function:

$$F_2 = (\psi_x - \frac{p}{3}\Omega + \frac{\zeta}{3})J. \tag{2.56}$$

This yields:

$$H = \delta J + G_{3,0,p}J^{3/2}\cos(3\psi), \tag{2.57}$$

where the *resonance proximity parameter* $\delta = \nu_x - p/3$ has been introduced. The Hamiltonian is now invariant and the particle motion in phase space will follow the contour lines of a constant Hamiltonian. From the latter, using Hamilton's equations the equation of motion in transverse phase space for the single $3\nu_x = p$ resonance can be derived.

2.2 Longitudinal motion

A way to accelerate charged particles is to use electric fields parallel to the particle velocity. For circular accelerators, radio frequency (RF) cavities can be used to provide the needed accelerating field every turn when the resonance condition is respected. The voltage in the RF is such that the field in the RF gap is:

$$\mathcal{E} = \mathcal{E}_0\sin(\omega_{rf}t + \phi_s), \tag{2.58}$$

where $\mathcal{E}_0$ is the amplitude of the electric field, ϕ_s is the phase of the *synchronous particle* with respect to the RF wave $(\sin(\omega_{rf}t))$. The RF angular frequency ω_{rf} is chosen as an integer multiple of the angular revolution frequency of the synchronous particle $\omega_0 = 2\pi\beta c/C$, where C is the machine circumference. In fact the angular RF frequency is:

$$\omega_{rf} = h\omega_0, \tag{2.59}$$

with h called *harmonic number*. Such a quantity represents the maximum number of bunches that can be accelerated in a synchrotron for a certain RF frequency.

In a synchrotron, at each turn, the energy gain ΔE that the synchronous particle receives

travelling through a cavity of length g is

$$
\begin{aligned}
\Delta E &= e \int_{-g/2}^{g/2} \mathcal{E}_0 \sin(\omega_{rf} t + \phi_s) ds \\
&= e \mathcal{E}_0 \beta c \int_{-g/(2\beta c)}^{g/(2\beta c)} \sin(\omega_{rf} t + \phi_s) dt = e \mathcal{E}_0 g T \sin(\phi_s),
\end{aligned}
\tag{2.60}
$$

where e is the charge of the particle and T is defined as the transit time factor:

$$
T = \frac{\sin(hg/(2R_0))}{hg/(2R_0)}.
\tag{2.61}
$$

Defining the actual voltage seen by the beam as:

$$
V = \mathcal{E}_0 g T,
\tag{2.62}
$$

the acceleration rate for a synchronous particle can be written as:

$$
\dot{E}_0 \equiv \frac{\mathrm{d}E_0}{\mathrm{d}t} = \frac{\omega_0}{2\pi} eV \sin(\phi_s).
\tag{2.63}
$$

The motion of particles, as seen in the previous section, depends also on their relative momentum offset with respect to the synchronous particle. The dispersion is the function that describes the motion of such particles, in fact the change in path length along a circular machine is written as:

$$
\Delta C = \oint \frac{x}{\rho(s)} ds = \delta_p \oint \frac{D_x(s)}{\rho(s)} ds.
\tag{2.64}
$$

The definition of *momentum compaction factor* α_c arises from the latter as:

$$
\alpha_c \equiv \frac{\Delta C / C}{\delta_p}
\tag{2.65}
$$

where C is the machine circumference. The fact that the path length depends on the individual momentum of the particles, also implies a dependence of the revolution frequency on the momentum offset. This can be written as:

$$
\frac{\Delta \omega}{\omega_0} = \frac{\Delta \beta}{\beta_0} - \frac{\Delta C}{C},
\tag{2.66}
$$

where the revolution frequency change has been expressed in relation to the change in path length and velocity. The derivative of the longitudinal particle momentum $p = \gamma m c \beta$ with respect to β is $\frac{\mathrm{d}p}{\mathrm{d}\beta} = p\gamma^2/\beta$, then the fractional change in velocity due to a different momentum is:

$$
\frac{\Delta \beta}{\beta_0} = \frac{1}{\gamma_0^2} \frac{\Delta p}{p_0}.
\tag{2.67}
$$

Using Eq. (2.66) and (2.67), the *slip factor* can be defined as:

$$\eta \equiv -\frac{\Delta\omega/\omega_0}{\delta_p} = \alpha_c - \frac{1}{\gamma_0^2} = \frac{1}{\gamma_t^2} - \frac{1}{\gamma_0^2}, \tag{2.68}$$

where the *gamma transition* (or transition energy) $\gamma_t \equiv 1/\sqrt{\alpha_c}$ was introduced. When $\gamma < \gamma_t$, the revolution frequency is larger for particles with positive energy offset. At the contrary, above transition energy, $\gamma > \gamma_t$, a particle with higher energy than the synchronous particle ($\delta_p > 0$) has a smaller revolution frequency; vice versa for $\delta_p < 0$. At transition energy, $\gamma = \gamma_t$, the revolution period is completely independent from the individual particle energy.

Longitudinal phase space

As previously done for the transverse case, the equation of motion can be retrieved from a Hamiltonian via Hamilton's equations. The Hamiltonian in the conventional longitudinal phase space (ϕ, δ_p), with ϕ phase of an individual particle with respect to the RF wave, can be written as

$$H = \frac{1}{2}h\omega_0\eta_0\delta_p^2 + \frac{\omega_0 eV}{2\pi\beta_0^2 E}[\cos(\phi) - \cos(\phi_s) + (\phi - \phi_s)\sin(\phi_s)], \tag{2.69}$$

where the time has been used as independent variable and the subscript "0" or "s" refers to the synchronous particle. The latter Hamiltonian is not consistent with the description of the transverse motion presented here, due to the discrepancy in the independent variable. It has to be taken into account that this is only an approximation, but it permits to describe the synchrotron motion by itself without introducing the coupling with the transverse one. Under this approximation, the linearised equation of motion becomes:

$$\frac{\mathrm{d}^2}{\mathrm{d}t^2}(\phi - \phi_s) = \frac{h\omega_0 eV\eta_0\cos(\phi_s)}{2\pi\beta^2 E}(\phi - \phi_s). \tag{2.70}$$

From the Eq. (2.70), the stability condition that arises reads:

$$\eta_0\cos(\phi_s) < 0. \tag{2.71}$$

This implies that below transition (where $\gamma < \gamma_t$ and $\eta_0 < 0$), the synchrotron motion is stable if $0 \leq \phi_s < \pi/2$. On the contrary, above transition ($\gamma > \gamma_t$ and $\eta_0 > 0$), the synchronous phase should be chosen as $\pi/2 > \phi_s \geq \pi$. In case of stationary bucket (no acceleration) for the same reasons, below transition the stable phase is $\phi_s = 0$ and above transition is $\phi_s = \pi$. This is highlighted in the Fig. 2.6 where the constant Hamiltonian of Eq. (2.69) in (ϕ, δ_p) phase space is represented.
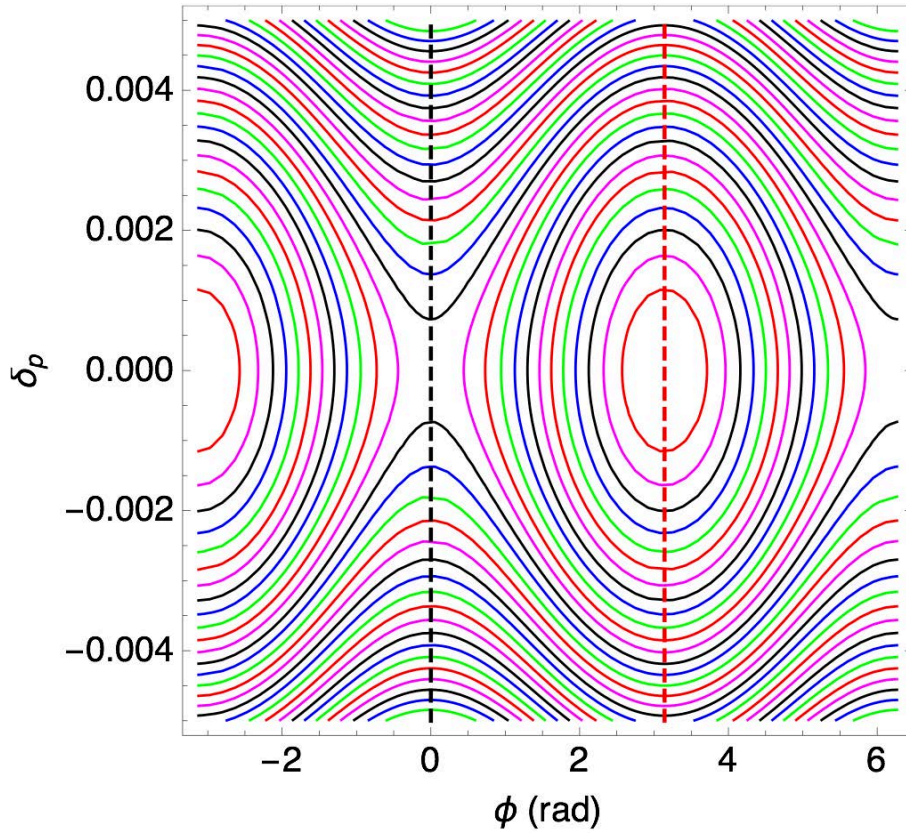
Figure 2.6 – Contour plot of the Hamiltonian of Eq. (2.69) above transition and for an arbitrary value of voltage. The black dashed line shows the unstable phase when operating above transition, instead the red shows the stable one for stationary bucket.

CHAPTER 3

The SPS and the LHC

The LHC is the largest particle accelerator of the world with its 26.659 km circumference. It is the last ring of the CERN accelerator complex and it is installed about 100 m underground. It is composed by eight straight sections (IRs) to host experiments and insertion elements (injection, extraction, etc.) and eight arcs. Four of the eight straight sections (IPs) host the LHC experiments: ATLAS (IP1), ALICE (IP2), CMS (IP5) and LHC-b (IP8). Two additional experiments, TOTEM and LHCf, are installed upstream and downstream of IP5 and IP1, respectively. In these regions, the two circulating beams (either made of protons or lead ions) are put into collisions when the maximum beam energy is reached.

In the LHC, beams are injected at 450 GeV and accelerated up to 7 TeV, making the LHC beams the most energetic in the world. Such beams need to be pre-accelerated before injection into the LHC. This takes place in the so-called *LHC injector chain*. Depending on the beam to deliver to the LHC (proton or lead ion), two different paths are possible (Fig. 3.1). For proton physics (majority of the year), the LHC injector chain is composed by:

- LINAC 2. A linear accelerator which accelerates protons up to 50 MeV.

- Proton Synchrotron Booster (PSB). It is composed by four superimposed rings where the beam is accelerated to 1.4 GeV.

- Proton Synchrotron (PS). The oldest accelerator at CERN (switched on in 1979); it accelerates beams up to 26 GeV. It is the first accelerator of the LHC injector chain which is shared between proton and lead beam production.

- Super Proton Synchrotron (SPS). It is the second largest machine of the CERN complex and accelerates particle beams up to a maximum of 450 GeV.

All these machines are interconnect to each other via transfer lines (TL). The TLs connecting the SPS and the LHC are about 3 km long. Due to the high stored energy in

the beam to be transported, they are the only TLs in the world to be equipped with a complete collimation system.

In this chapter, the main aspects of the SPS, the LHC and their TLs will be presented.

Figure 3.1 – The CERN accelerator complex.

3.1 Super Proton Synchrotron

The SPS is composed by 1317 room temperature electromagnets, including 744 main dipoles (each 6.2 m long) and 216 laminated quadrupoles. During its history, it has accelerated a variety of particles, i.e. sulphur and oxygen nuclei, electrons, positrons, protons and antiprotons.

The SPS has a circumference of 6911 m. It is a multi-propose accelerator, in the sense that provides high-energy particle beams to different users. Its main users are the LHC (450 GeV extraction), the North experimental Area (NA) and its experiments (400 GeV slowly extracted) and AWAKE [13]. Also, the SPS provides beam to an experimental facility, HiRadMat (High Radiation to Materials), where the effect of high energy and high intensity beams on materials or actual accelerator components is studied.

The SPS started to operate in 1976, and, from that date, it has been used to probe the inner structure of protons, investigate nature's preference for matter over antimatter, as

well as to seek exotic forms of matter. In 1983 the SPS reached the most famous result of its operation with the Nobel-prize winning discovery of the W and Z bosons when working as proton-antiproton collider.

The SPS is based on a periodic FODO lattice with a super-symmetry of six, where each period is formed by an arc of sixteen FODO cells with a central long straight section (LSS) of two cells. Insertion elements are installed in each LSS. The injection, the scraper and the dump systems are installed in LSS1. The LSS2 is dedicated to the slow extraction channel towards the NA and the LSS3 to the RF system (Fig. 3.2). The LSS4 and 6 host the fast extraction systems (Fig. 3.2) used to deliver beam to the LHC, AWAKE and to the HiRadMat area. In LSS5 instead, the UA9 experiment and other instrumentation are grouped.
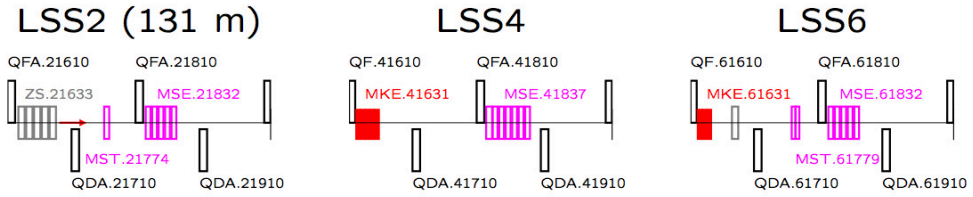
Figure 3.2 – Schematic view of the SPS LSS2, 4 and 6. These are the LSS where the extraction systems are installed.

The SPS is a cycled machine, meaning that each beam that is injected is stored only for a few tens of seconds (Fig. 3.3). This means that, depending on the different injected beam, and for its purposes, a different optics can be used. Three different optics are usually used during normal operations: Q20, Q26 and SFTPRO optics. The first is the one used to deliver beams to the LHC. Together with the Q26 (previous optics for LHC beams), are the optics used for high intensity bunched beams (LHC type). The SFTPRO optics is used for slow extraction towards the NA for fixed target physics. The main differences are listed in Table 3.1.
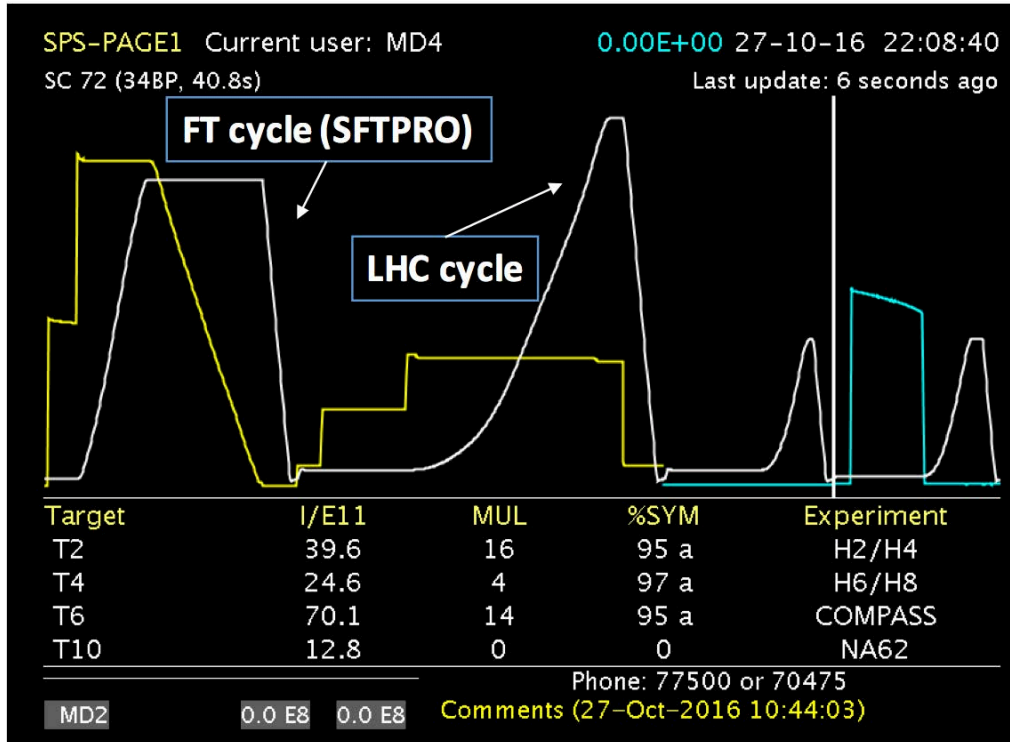
Figure 3.3 – Example of a typical SPS super cycle as shown from the SPS Page 1.
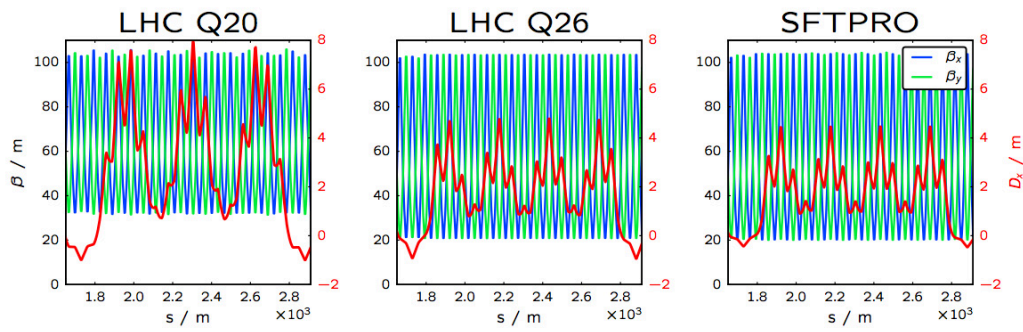
Figure 3.4 – Twiss functions the main SPS optics along one sextant: Q20, Q26 and SFTPRO.

Table 3.1 – Summary of the main parameters of the three main SPS optics.

SPS Optics	LHC Q20	LHC Q26	SFTPRO
Horizontal tune, ν_x	20.13	26.13	26.62
Vertical tune, ν_y	20.18	26.18	26.58
Natural chromaticity, Q'_x/Q'_y	-22.7/-22.7	-32.6/-32.63	-33.51/-33.46
Maximum betas, $\beta_x \approx \beta_y$ [m]	105	105	105
Minimum betas, $\beta_x \approx \beta_y$ [m]	30	20	20
Maximum dispersion, D_x [m]	4.5	8	4.4
Transition energy, γ_t	18	22.8	22.8
Phase advance per cell, $\mu_x \approx \mu_y$ [°]	67.5	90	90

3.1.1 Fast extraction

The LSS4 and LSS6 are straight sections where the fast extraction elements of the SPS are installed. The fast extraction is a process that permits to eject the circulating beam in one machine revolution. Usually, a kicker magnet is triggered and the beam is deflected from its nominal orbit towards the aperture with magnetic field of a septum magnet. The septum provides the additional deflection to the beam which is needed to leave the synchrotron and access the TL.

Kicker magnets, or simply kickers, are fast pulsed magnets. The time needed to reach the maximum field (the so-called rise time) has to be shorter than one machine revolution minus the beam length to minimise the beam losses of the single-turn extraction. In general, the rise times for kickers used in high energy machines are in the order of $[1 \times 10^{-7}, 1 \times 10^{-6}]$ seconds. This can be achieved by charging a capacitor to a high voltage and then discharging it through the transmission line of the kicker [14]. In general there is only a single conductor, so a current pulse of the order of a few thousand A is needed to generate sufficient magnetic field. The beam passes through a gap in the magnetic yoke, which is arranged symmetrically with respect to the closed orbit, hence the magnetic field B produced by the flowing current I in the coil is given, if $\mu_r \gg 1$, by

$$B = \frac{\mu_0 I}{h} \tag{3.1}$$

where h is the gap height. This corresponds, in a relativistic domain, to a deflection angle θ of

$$\theta = \frac{l}{\rho} = 0.2998 \frac{B[T]l}{p[GeV/c]} \tag{3.2}$$

where l is the magnetic length and ρ the bending radius. An example of kicker magnet is shown in Fig. 3.5.

Septa are special insertion magnets that define the border from the ring and the TLs.
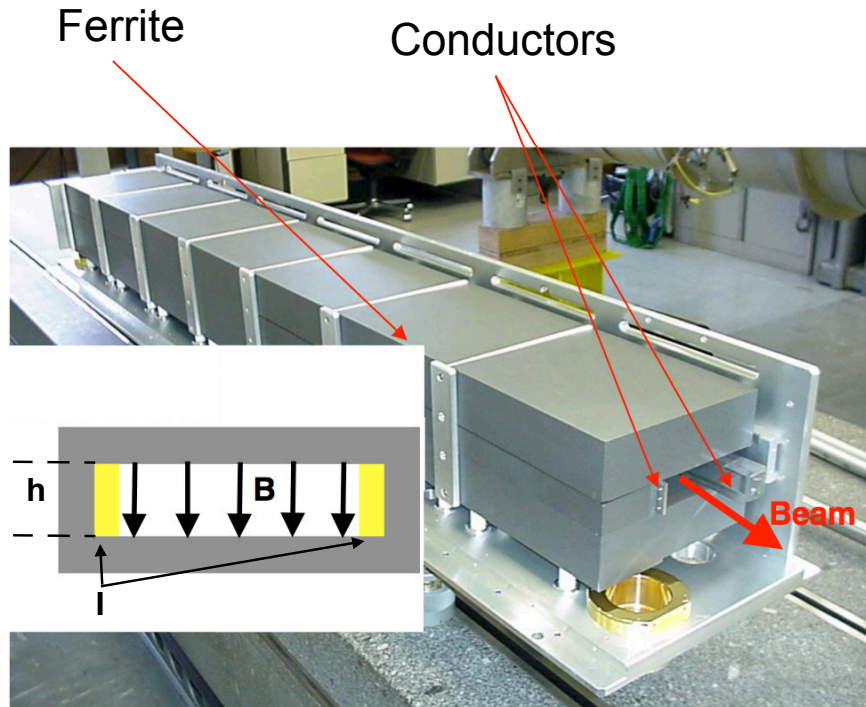
Figure 3.5 – Illustration of the yokes of an SPS extraction kicker.

The septum conductor physically separates the circulating beam from the extracted one. Usually they are active for a few seconds or even completely DC, and hence they can reach magnetic fields in the order of a few T. (Fig. 3.6).

In the SPS, the beam momentum at extraction is $450\,\mathrm{GeV/c}$ and due to the large beam rigidity, it is very challenging to realise a kicker that alone can provide the necessary deflection for the extraction. In fact, to limit the required field of the kicker, the beam orbit is locally distorted (closed orbit bump) to reduce the distance from the beam centre and the septum blade. This is realised using small dipoles, so-called bumpers. An example of fast extraction from the SPS is shown in Fig. 3.7.

The main fast extraction elements installed in the SPS are:

- Extraction kickers, MKE. Four installed in LSS4 and three in LSS6. The main characteristics are listed in Table 3.2.

- Extraction magnetic septa, the Magnetic Septum Thin (MST) and the Magnetic Septum Extraction (MSE). Some of these element parameters are summarised in Table 3.3.
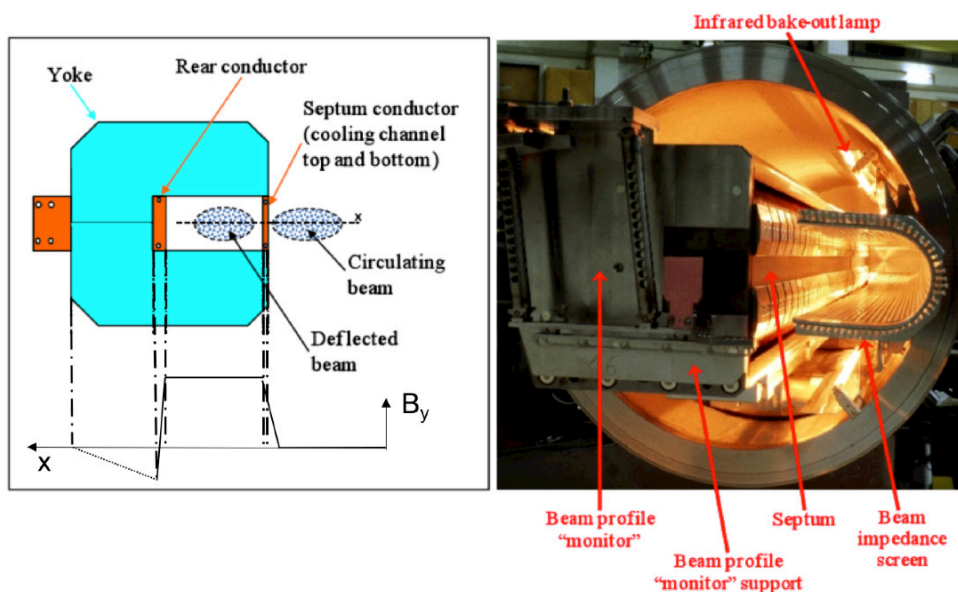
Figure 3.6 – Illustration of a septum magnet and its principle of functioning.
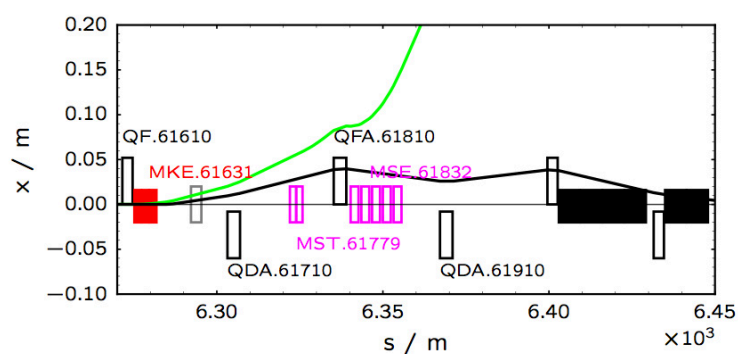
Figure 3.7 – Schematic view of the LSS6 fast extraction layout. The circulating beam CO is plotted in black and the extracted beam trajectory in green.

Table 3.2 – Main parameters of the SPS extraction kickers.

Parameters	MKE-L	MKE-S	Unit
Gap height	35	32	mm
Magnetic length	2.174	2.174	m
Deflection required	0.10	0.11	mrad
$\int B\,dl$ max	0.15	0.17	T m
Rise/fall time (LSS4)	≈ 8	≈ 8	µs
Rise/fall time (LSS6)	≈ 6	≈ 6	µs
Flat top duration (LSS4)	≈ 15	≈ 15	µs
Flat top duration (LSS6)	≈ 16	≈ 16	µs

Table 3.3 – Main parameters of the SPS septa.

Parameters	MST	MSE	Unit
Number of magnets	2	5	-
Septum thickness	4.2	17.25	mm
Gap height	20	20	mm
Magnetic length	2.247	2.237	m
Deflection required	0.532	1.892	mrad
$\int B\,dl$	0.798	2.838	T m
Current at $450\,\mathrm{GeV}$	5.654	20.183	kA
Magnet resistance	1.07	0.34	m Ω
Magnet inductance	13	12	µH
Rise/fall time	≈ 200	≈ 200	ms
Flat top length	≈ 300	≈ 300	ms

3.1.2 Slow resonant extraction

The main users of the SPS are the Fixed Target (FT) experiments of the NA. They require a constant flux of particle at $400\,\mathrm{GeV}$. The extraction channel installed in LSS2 is in fact used for slow resonant extraction exploiting the one-third integer resonance. The elements for such an extraction comprise: a set of bumper magnets (as for the fast extraction), an electrostatic septum (ZS), and the two magnetic septa (MST and MSE) and four extraction sextupole (installed in LSS1, 3, 4 and 5).
The content of this subsection is based on [15], unless explicitly specified.
The slow extraction process starts when the beam has been accelerated to its extraction energy. The extraction sextupoles are turned on in a quasi adiabatic way, the extraction bump brings the beam closer to the electrostatic septum and the tune is changed approaching the resonance condition, i.e. $\nu_x = N + p/3$, with N and p integers. In this way, the motion in phase space is distorted, as shown in the previous chapter (Fig. 2.4). Particles lying outside the stable region will be pushed to higher amplitudes towards the three separatrices. The electrostatic septum wires are used as a blade to "cut" the extracted beam from the circulating one. The final deflection needed to leave the circular machine is given by the magnetic septum.

Resonance stop-band

In the SPS there are four extraction sextupoles installed all around the machine. For the conceptual explanation of the slow extraction process a *virtual sextupole* can be defined and will be used from now on in order to simplify the calculations. Then, the normalised

strength of the virtual sextupole can be written as:

$$S = \frac{1}{2}\beta_x^{3/2}\frac{l}{|B\rho|}\left(\frac{\mathrm{d}^2 B_y}{\mathrm{d}x^2}\right)_0 = \frac{1}{2}\beta_x^{3/2}lk',$$ (3.3)

where β_x is the horizontal beta function at the sextupole location, l is the sextupole length, $B\rho$ is the beam rigidity and B_y is the vertical component of the magnetic field. The stability area directly depends on the sextupole strength and the distance from the resonance, $\delta\nu \equiv \nu_{particle} - \nu_{resonance}$. It can be proved that the stable area (triangular shape) is written as:

$$A_{stable} = 2J_{stable}\pi \leq \frac{48\sqrt{3}\pi}{S^2}(\delta\nu)^2\pi,$$ (3.4)

with the notation used in the previous chapter. Inverting the inequality in Eq. (3.4), the unstable area can be derived. Hence, the tune range $\delta\nu$ where particles with a certain amplitude are unstable is:

$$|\delta\nu| < \sqrt{\frac{J}{24\sqrt{3}\pi}}|S|,$$ (3.5)

where the range $|\delta\nu|$ is usually referred to as stop-band of the third-integer resonance for a given amplitude J (Fig. 3.8).
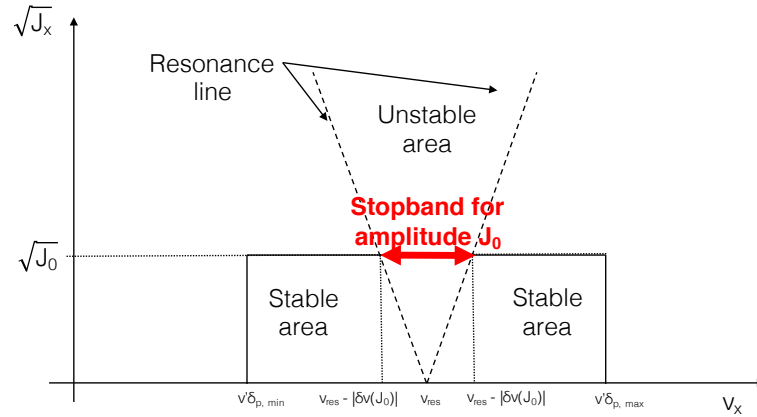
Figure 3.8 – Schematic view of the slow extraction process as Stainbach diagram.

From Eq. (3.5), the equation of the *resonance line* can be derived, yielding:

$$\sqrt{J} = \sqrt{24\sqrt{3}\pi}\left|\frac{\delta\nu}{S}\right|.$$ (3.6)

This equation defines the border of stability, depending on the particle amplitude, for a given $\delta\nu$. In fact, there is no stable amplitude for particles exactly on resonance, $\delta\nu = 0$. Also, the range of stable amplitudes increases when the tune is shifted from the resonance.

Extraction methodology

From Fig. 3.8 it is clear that particles have to be moved in the unstable region to be extracted, or the unstable region has to be moved towards them. Eq. (3.6) is by definition the stability border, hence possible ways to drive particle unstable in a controlled way are:

- Increase the stop-band width (SBW) by increasing the sextupole field;

- Increase the particle amplitudes until they cross the resonance line (e.g. RF knock-out);

- Change the beam tune to move particles inside the unstable region.

The beam energy is the main limitation of the first two methodology. Both of them become very challenging at high energies. The third one, instead, is much more suitable for high energy slow extraction due to the usual small tune variation needed for the complete beam extraction. In the SPS in fact, the last extraction methodology is used. For this method the unstable area is unchanged. The tune of the machine is varied and particles with different momenta are driven unstable (Fig. 3.9). The intensity distribution of the spill depends on the momentum distribution of the beam and on the rate of the tune change.
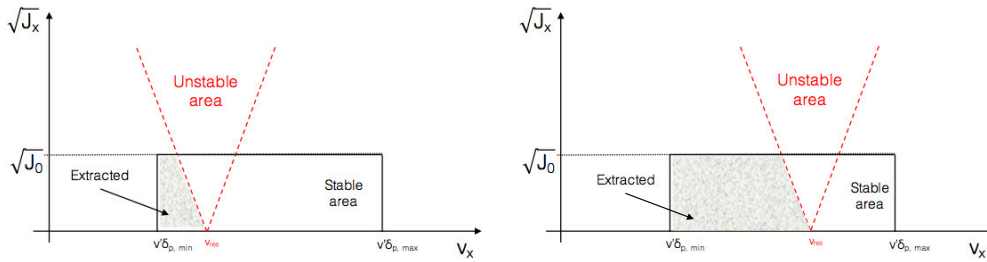
Figure 3.9 – Stainbach diagram of a slow extraction where the machine tune is changed to drive particles unstable.

Spiral step

When a particle is outside the stable region, its amplitude grows quickly. The amplitude growth of a particle on one-third integer resonance can be seen schematically in Fig. 3.10.

The spiral step is defined as the amplitude growth in three turns for a particle with tune exactly on resonance and initial amplitude equal to the transverse position of the electrostatic septum wire. This can be written as:

$$\Delta X_{ZS} = \frac{3}{4}|S|\frac{X_{ZS}^2}{\cos\theta}, \tag{3.7}$$

where X_{ZS} is the normalised horizontal amplitude at the ZS and θ is the angle between the extraction separatrix and the horizontal axis in normalised phase space.

The spiral step defines the horizontal beam size of the extracted beam. It is the maximum amplitude allowed at the electrostatic septum location. In fact, the rectangular horizontal phase space footprint of the extracted beam is used to define the optics of the transfer line form the electrostatic septum to the fixed target.
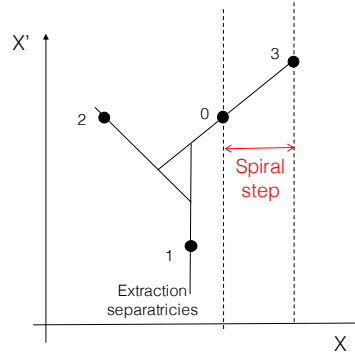
Figure 3.10 – Schematic view of the definition of spiral step.

The extraction separatrices are continuously filled with particles, hence the electrostatic septum wires will be hit by some primary protons. Therefore, the efficiency of the slow extraction critically depends on the thickness of the electrostatic septum wires. A usual configuration of a slow extraction channel comprises an electrostatic septum followed by a thin magnetic one. Such a configuration permits to achieve the required deflection needed to extract the beam.

Hardt condition

For a momentum spread based slow extraction, the part of the beam along the extraction separatrices will have a different fractional momentum as the tune is changed during the extraction process. At a location with a non-zero dispersion, the extraction separatrices will not always overlap. If this happens at the electrostatic septum location, the effective width of the extraction separatrix all along the extraction process will be increased. This is shown in Fig. 3.11. Due to the spread in angle, and accounting for the septum length and field, the losses will be increased. Depending on their initial conditions, such particles can hit the septum wires further downstream. Given the horizontal transverse

coordinates of a particle at the septum entrance (x_0, x_0'), the septum length L_{ES} and its distance from the beam centre Δx_{ES}, the particles that will be lost at the wires can be determined from:

$$x(s) = sx_0' + x_0 + \frac{\theta_{ES}}{L_{ES}}s^2 \tag{3.8}$$

$$x(s) = -\frac{\Delta x_{ES}}{L_{ES}}s. \tag{3.9}$$

The deflection of the extracted beam operated by the ES is given by:

$$\theta_{ES} = \tan^{-1}\left[\frac{|E_x|L_{ES}}{p\beta}\right] = \tan^{-1}\left[\frac{|V_x|L_{ES}}{dp\beta}\right] \tag{3.10}$$

where E_x is the electrostatic field and V_x the voltage between the conductors placed at a distance d. If $0 \le s \le L_{ES}$ then the particle will hit the wires from the left. Then, for $\theta = 0$, the Eq. (3.9) can be solved to evaluate if the particle will hit the septum from the right.
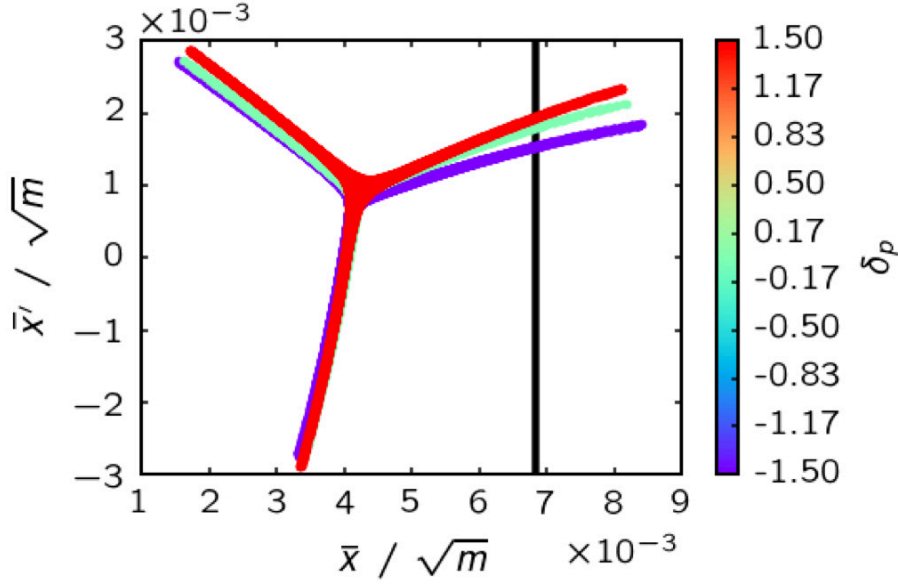
Figure 3.11 – Example of normalised phase space at the ES when the Hardt condition is not respected.

The machine optics can be tuned in a way that the separatrices will overlap at the extraction point. This is known as the *Hardt condition*. It can be proved that the

equation that has to be satisfied for this to happen is:

$$D \cos(\alpha_0 - \Delta\psi) + D' \sin(\alpha_0 - \Delta\psi) = -\frac{4\pi}{S} Q'_x, \tag{3.11}$$

where α_0 is the angle between the extraction separatrix and the ES, $\Delta\psi$ is the phase advance between the virtual sextupole and the ES, D and D' are the normalised dispersion function and its derivative and Q' is the horizontal chromaticity. Although Eq. (3.11) seems easily adjustable, some constraints have to be accounted for:

- The angle $(\alpha_0 - \Delta\psi)$ is given by the geometry of the extraction and by the machine configuration,

- The sextupole strength S is closely linked to the slow extraction dynamics and can only be marginally changed,

- The chromaticity is one of the main variables but it can be varied only in the range of values that guarantee the stability of the high intensity beam,

- The dispersion function is given by the lattice.

3.2 SPS-to-LHC transfer lines

The two ≈ 3 km long TLs, TI2 and TI8, are responsible for the safe transfer of high brightness beams form the SPS to the LHC. The space constraint, the beam energy and power and the preservation of the beam emittance made their design a challenge under all aspects [16]. Their geographical layout is shown in Fig. 3.12 together with the SPS and the LHC.

The TI2 line connects the SPS LSS6 to the LHC IR2. It branches off from TT60 which is the TL directly connected to the extraction system in LSS6. The TI8, instead, branches off from TT40 which is connected to the LSS4.

Different possible designs were considered, also including exotic ideas such as polarity reversal of the SPS to use only one TL, but the choice of having two completely normal conductive lines was taken.

The optics design of the TLs took into account the requirements of delivery precision from the LHC and also let the possibility of future optics change. In fact, following the optics change in the SPS (form Q26 to Q20), the TLs optics was rematched. The central part of both lines is composed by a FODO structure with 90° phase advance per cell. Dedicated matching sections (independently powered quadrupoles) are installed at the beginning and at the end of each line.

The main optics constraints in the TLs come from the difficulty to match the dispersion to the LHC and from the phase advance relation among the TL collimators (TCDI). In fact, in order to protect the LHC aperture and the injection septum, a complete collimation system is installed in both TI2 and TI8. Such a system is based on a 3-phase

collimation, i.e. three collimators per plane with 60° between two subsequent collimators. Therefore, they are installed as close as possible to the end of each line [16].
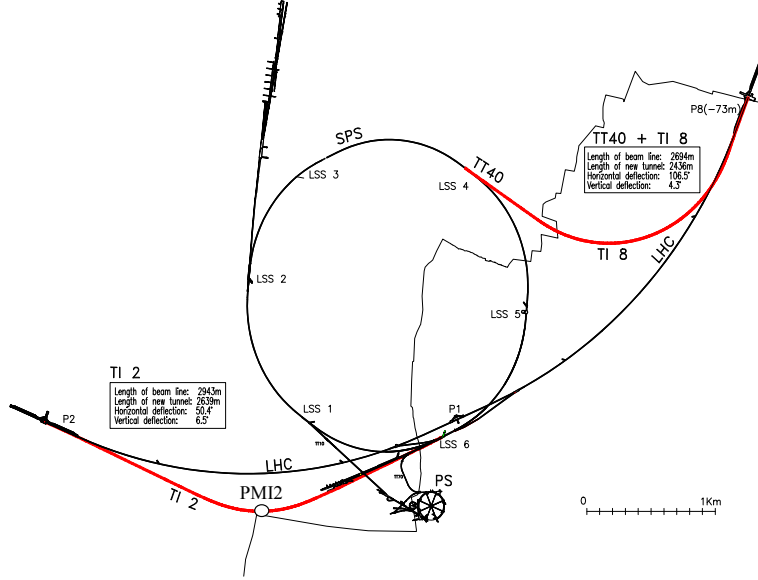
Figure 3.12 – View of the SPS and its TLs to the LHC [16].

3.3   Large Hadron Collider (LHC)

The beam energy reachable at the LHC is a direct consequence of its circumference and main dipole strength. All the LHC main dipoles are super-conductive, as well as the main quadrupoles and correctors. The LHC is composed by 1232 main dipoles, 386 main quadrupoles and more than 4000 orbit correctors. The experiments occupy IR1, 5, 2 and 8, nevertheless IR2 and IR8 also host the injection channels for Beam 1 (B1) and Beam 2 (B2), respectively. The RF cavities are installed in IR4, the collimation system in IR7 and the extraction systems towards the beam dumps are installed in IR6.
As previously introduced, the HL-LHC upgrade is aiming to push the peak luminosity of about one order of magnitude. The main modifications foreseen to reach such a luminosity, beyond the upgrade of the injectors, can be summarised as [17]:

- Inner triplet magnets: the expected dose received by the triplet quadrupoles and its correctors after the reach of $300\,\text{fb}^{-1}$ integrated luminosity will be about $30\,\text{MGy}$. In this regime of dose, some of these magnets are expected to have already failed. In order to anticipate this, the replacement of the triplet is envisaged.

- Super-conductive crab cavities: to improve the colliding bunch overlap and hence to increase the geometric factor F in Eq. (1.1) such special insertion devices will

be installed.

- Collimation system: the doubled beam stored energy foreseen for the high luminosity upgrade implies the need to upgrade the collimation system to maintain the current cleaning efficiency. Also, the higher beam intensity requires a lower beam induced impedance from these devices.

- Dispersion suppressors (DS): the leakage of off-momentum particles from the primary collimators, and their following losses in the dispersion suppression regions, have been identified as possible performance limitation. The proposed concept to remove this bottleneck foresees the replacement of the LHC main dipoles in the DS with dipoles of the same strength but higher field and shorter length. In this way, an ad-hoc designed collimator can be placed between them to absorb the off-momentum particles.

- Beam diagnostic improvements.

- Machine protection: improvements of the robustness against mis-steered beam from injection and extraction kickers. This includes upgrades of the passive protection devices as well as the kicker systems themselves.

- Improved availability: in order to increase the integrated luminosity, a plan to improve the machine availability is foreseen. This comprises upgrades of: cryogenics, radiation to electronics handling, quench protection system.

Super-conducting devices are by definition very sensitive to any temperature increase. The stored energy in the beam that circulates in the LHC makes it a likely source of temperature increase in the magnets in the case of particle losses. The maximum stored energy in the LHC beam is 362 MJ and is expected to be doubled in the HL-LHC era (Fig. 3.13). These numbers are orders of magnitudes higher than the quench or damage limit of the machine components. Hence, in order to protect the machine against uncontrolled beam losses, protection and halo cleaning systems are needed. As briefly mentioned before, IR3 hosts the momentum cleaning and IR7 the betatron cleaning. The two injection regions, IR2 and IR8, are both equipped with passive protection systems, as well as IR6 has passive devices which complete the extraction systems.

3.3.1 LHC injection systems

The two TLs, TI2 and TI8, deliver the beam to the LHC in the two insertion points IR2 and IR8, shared with ALICE and LHC-b, respectively. In both cases, the beam comes form the outside and below the machine plane [16]. Lambertson [16] septa are the first elements of the injection system, which deflect the beam horizontally by 12 mrad towards the nominal orbit. Then, a series of injection kickers (MKI) adjust the beam vertical trajectory (0.85 mrad) and fix the injected beam onto the closed orbit. To protect the
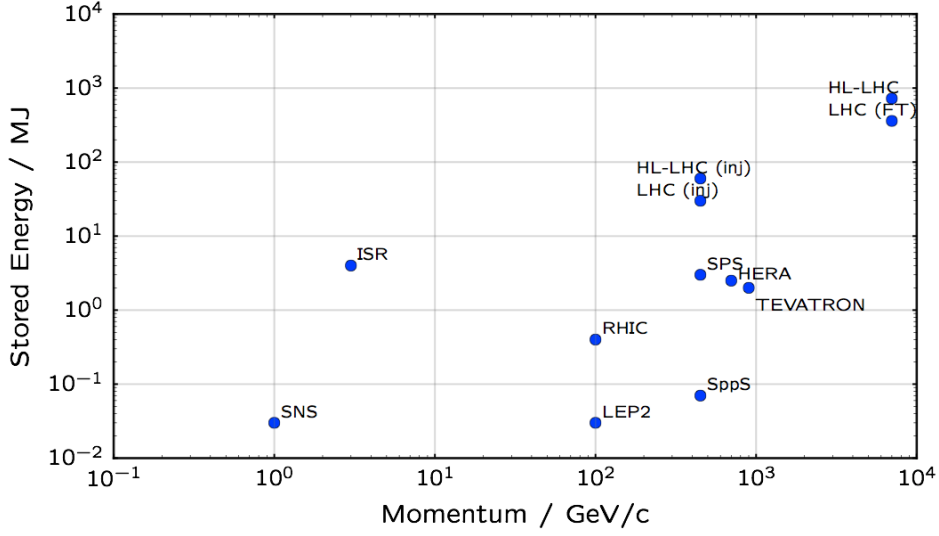
Figure 3.13 – Beam stored energy as a function of the beam longitudinal momentum of the main accelerators around the world [18].

LHC against failures of the MKI, an injection beam stopper (TDI) is located at 90° phase advance from it (about 15 m upstream the super-conductive recombination dipole, D1). The D1 is also protected from secondary showers, originated by the interaction of the beam with the TDI jaws, by the TCDD. The passive injection protection system is completed by two auxiliary absorbers, the TCLIA and TCLIB, which shade the LHC cold-bore apertures from possible optics errors between the MKI and the TDI [16]. A schematic view of the injection system in IR8 is shown in Fig. 3.14.
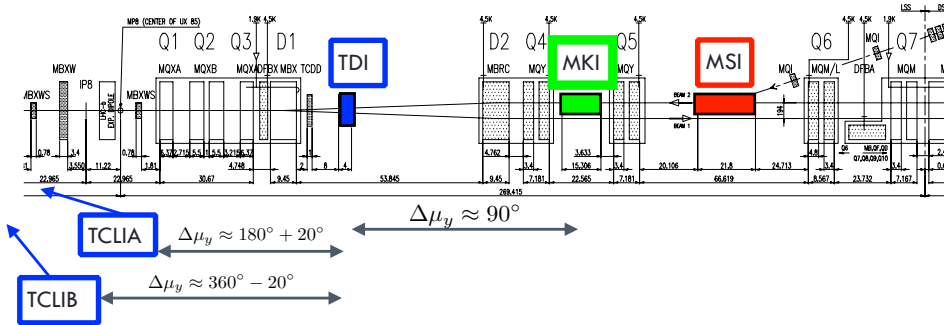
Figure 3.14 – Schematic view of the LHC injection system in IR8 [16].

Optics of the injection regions

The presence of fast pulsed magnets in the injection regions imposes the need of passive protection devices. As described above, optics constraints are essential to maintain the protection strategy. The HL-LHC optics, for the two injection regions, preserves such constrains, and only minor differences can be observed between the HLLHC V1.1 and LHC Run 2 optics (Fig. 3.15 and 3.16). The crossing and separation schemes are also very similar.

In this report, the simulations for the present LHC were done using the Run 2 optics, instead for HL-LHC, the version HLLHC V1.1 was used.
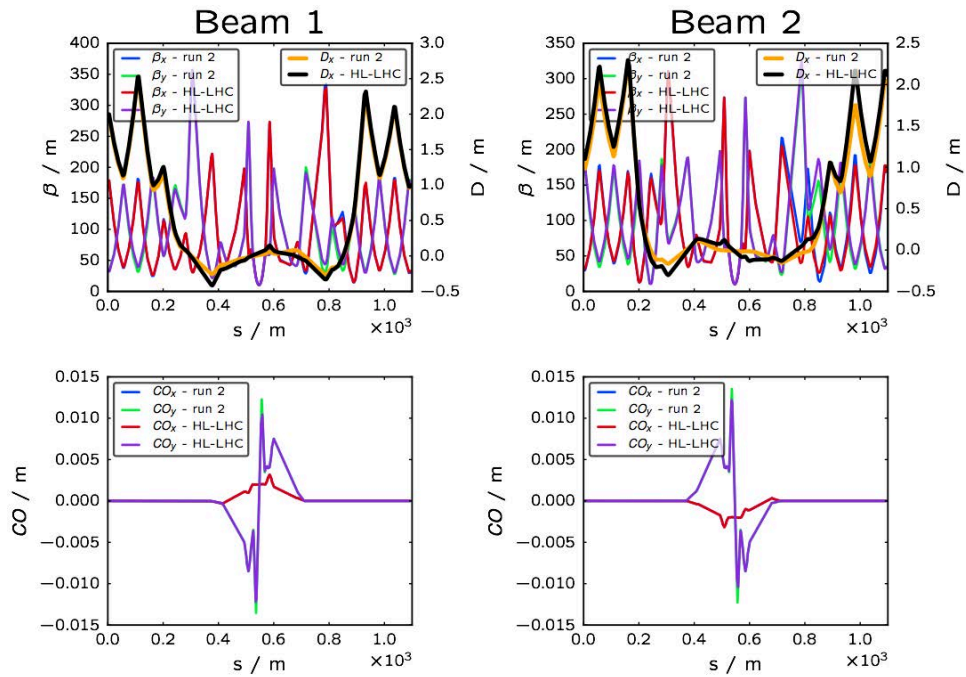
Figure 3.15 – Twiss functions (top) and orbit (bottom) at the IR2 for the Run 2 and HLLHC V1.1 optics.
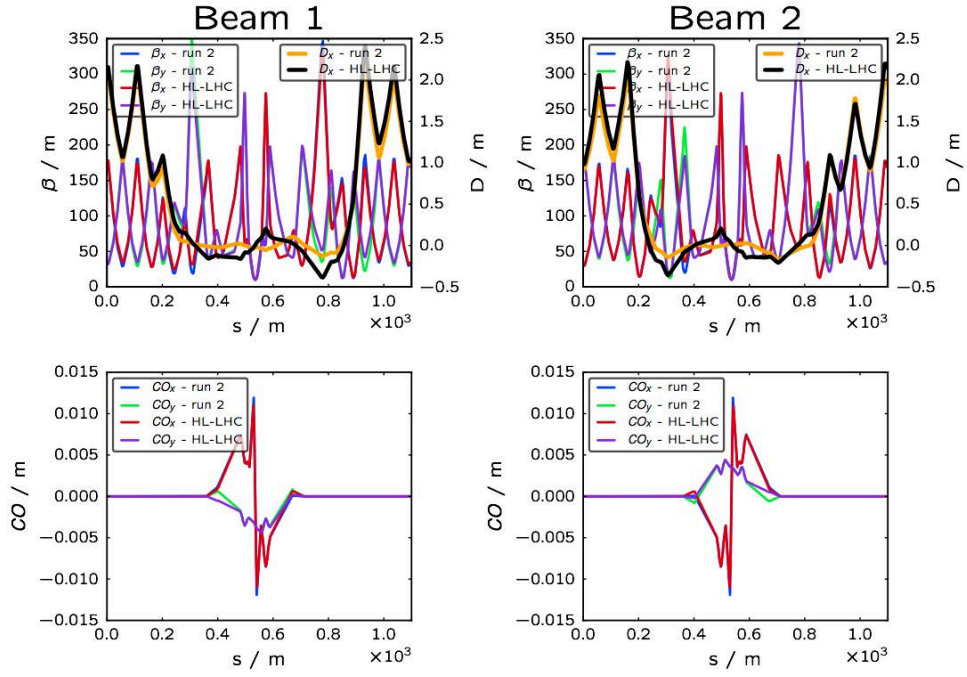
Figure 3.16 – Twiss functions (top) and orbit (bottom) at the IR8 for the Run 2 and HLLHC V1.1 optics.

CHAPTER 4

Non-local fast extraction

4.1 Motivation

The description of the beam dynamics, assuming an ensemble of non-interacting particles, is known as single particle beam dynamics, as presented in the first chapter. Under this assumption, the particle motion is derived only as interaction of the beam with the external electromagnetic (EM) fields. This description is valid as far as any additional EM field, originated by the presence of the totality of the beam, are not strong enough to perturb the single particle motion. In many cases though, for example for the HL-LHC operation, very intense and dense (high brightness) beams are required. In these cases, the EM fields created by the beam when interacting with the accelerator environment is significant and can be source of instability. This is classically viewed as an *instability loop*, where the beam motion is calculated accounting for the self-induced EM fields as well. In such a closed loop, small initial perturbation of the beam can be enhanced and lead to instability.

The intensity of the interaction between the resistive machine aperture and the beam itself is described by the wake fields, or equivalently the impedances (Fourier transform of the wake function), of the accelerator components. The wake function is essentially the impulse response of an accelerator component, and the impedance is its transfer function. The wake field produced by the beam passage (source) in a discontinuity can directly effect the witness particles (particles physically behind the source are the only one that can be affected, unless the wake persist longer than one turn) perturbing its motion. The effect of the impedance is non-negligible when the beam intensity goes above a certain threshold (instability threshold).

The SPS kickers (Fig. 4.1) are considered one of the main contribution to the total SPS impedance budget [1], accounting for about 40 % the total vertical tune shift due to impedance. For the upcoming luminosity upgrade a significant impedance reduction is required. In this context, the removal of one the SPS extraction kickers (MKE), could lead to a reduction of about 7 % the total SPS transverse impedance. In this

chapter, the possibility to remove the MKE in LSS6 by means of a non-local extraction is explored. The feasibility of this extraction concept is evaluated with both simulations and measurements with beam.

Figure 4.1 – Overview of the all SPS kickers. The MKPs are the injection kickers, the MKQV/H are the tune kickers, the MKDV/H are the dump kickers and the MKEs are the extraction kickers [*Courtesy of M. Barnes*].

4.2 Non-local extraction concept

The periodicity of a FODO lattice based on strong focusing can be exploited for extraction purposes. In fact, except for the elements physically needed at the location of the extraction (septa, bumpers), kickers and any other element that is used for the extraction (sextupoles, etc.), can be placed in any other accelerator location as far as the symmetry conditions are respected.The most direct example of this concept is the fast non-local extraction. In high energy machines, such as the SPS, the fast extraction is performed first adjusting the closed orbit to approach the septum blade, and then deflecting the beam with a kicker. In this way the total resulting deflection is obtain as a superimposition of kicks and closed bumps. The kicker is usually placed in the same FODO as the extraction septum. This is not the case for the non-local extraction, in fact a kicker placed in a favourable phase advance location can be used for the same purpose. A schematic example of this is shown in Fig. 4.2.

The main advantages of this concept are:
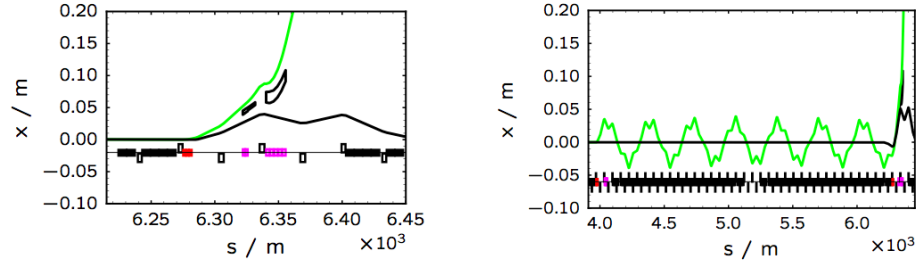
Figure 4.2 – Comparison of schematic view of normal fast extraction (left) and non-local extraction (right) in the SPS LSS6 using the MKE.4. The CO of the circulating beam is plotted in black and the trajectory of the extracted one in green. The mini-map showing the accelerator components has the following colour code: black, for the main quadruples and dipoles; red, for the kickers; magenta, for the septa.

- The reduction of the number of elements in the extraction regions;

- The possibility to reduce the activation of the extraction insertions (see Ch. 6);

- The possibility to use each single extraction element as a building block for a new way of extracting the beam (modular extraction channels).

Although there are multiple advantages, drawbacks have also to be taken into account:

- Increased risk of failures (more elements involved in the extraction process);

- High complexity from the interlocking point of view (one single device for multiple extraction types);

- Reduction of the acceptance of the extracted beam;

- More critical extraction and machine stability.

In the following section, the application of the non-local fast extraction concept to the SPS is presented. In the next chapters instead, a possible non-local extraction scenario applied to the slow extraction in the SPS, both non-resonant and resonant, will be discussed.

4.3   SPS non-local fast extraction

Nominally, B1 is extracted from LSS6, using MKE.6, and B2 from LSS4, using MKE.4. The possibility of extracting both B1 and B2 towards the LHC using the same fast pulsed magnet MKE.4 is explored (Fig. 4.2).
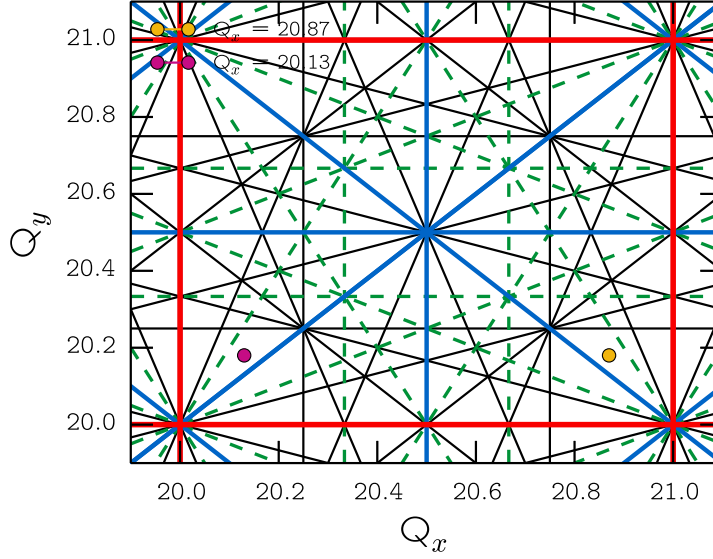
Figure 4.3 – Position on the tune diagram of the currently used tune and the one proposed for the non-local extraction of the LHC B1.

Taking into account only the on-momentum betatron transverse motion ($\delta_p = 0$), the particle transverse coordinate can be transported from a longitudinal location s_1 to another s_2 using Eq. (2.19). Assuming that $x(s_1) = 0$ (the beam CO at the kicker corresponds to the machine magnetic axis) and $x'(s_1) = 0$, the beam displacement at the location s_2 is then:

$$x(s_2) = \sqrt{\beta_1 \beta_2}\, \theta \sin(\Delta\psi), \tag{4.1}$$

where θ is the deflection provided by the kicker. In order to optimise the needed kick θ then, i.e. minimise the orbit oscillations amplitude and maximise the orbit excursion at the extraction point $x(s_2)$, the kicker in LSS4 (at s_1) and the extraction septum in LSS6 (at s_2) need to be at relative phase-advance as close as possible to 90°.

For the Q20 optics, the horizontal and vertical tunes are $\nu_x = 20.13$, $\nu_y = 20.18$, respectively. For this optics, the relative phase-advance between the kicker in LSS4 and the septum in LSS6 is about $2/3\pi$, which makes the non-local extraction for B1 not feasible. A different fractional part of the horizontal tune was thus explored. A natural choice was to move the WP to an island in the specular part of the tune diagram, i.e. $\nu_x = 20.87$ (Fig. 4.3). In this way, the relative phase advance between s_1 and s_2 is about $\pi/4$, which translates into an orbit excursion of 70 % the one obtainable with $\Delta\psi_x = \pi/2$.

Among the main drawbacks of the non-local extraction, those related to the beam dynamics can be evaluated for the SPS, with beam based measurements and simulations.

The non-local extraction technique has two intrinsic sources of possible aperture limitation: large betatron oscillations and not exactly $\pi/2$ phase-advance between the kicker and the septum. A trade-off between the kicker strength and the extraction bump amplitude has to be found to maximise the available aperture for both circulating and extracted beam. In this section, the results of error studies to evaluate the acceptance change with the non-local extraction technique are presented.

The extraction stability is a concern for operation. Due to the low limits on the accepted emittance growth as a consequence of injection errors in the LHC and possible losses at the transfer line collimators, the reproducibility of the TL trajectories is fundamental to guarantee high machine availability. During the LHC Run 1, variations of TL trajectories were observed, both fast, i.e. shot-to-shot variations, and slow, i.e. drift of the nominal trajectory. Monte Carlo simulations were performed to evaluate the shot-to-shot stability of the non-local extraction with respect to the normal SPS fast extraction. This has also been compared with available extraction stability measurements.

The SPS orbit stability can be critical for possible operation of the non-local extraction. In fact, variation of the nominal closed orbit represents a concern from the machine protection point of view when the available acceptance is small (large betatron oscillations during the extraction process). Hence, during LHC Run 2 commissioning, a campaign of measurements was put in place to investigate possible orbit drift sources, such as wrong transverse tune, large amplitude chromaticity trims, single dipole error, etc. The measurements carried out during commissioning of LHC Run 2 and during Run 2 itself are presented in the next section, together with the performed analysis and discussion of possible source candidates.

Aperture Analysis

The SPS orbit is dominated by the quadruple misalignments: no orbit correction can be applied at top energy due to the lack of strength in the correctors [19]. To obtain a realistic simulation scenario, MAD-X calculations were done applying random quadrupole misalignments ($\sigma_{dx,dy} = 100\,\mu$m) which could reproduce the measured orbit at $450\,$GeV with the Q20 optics [20]. The horizontal rms orbit distributions among the 1000 different simulated machines, for both local and non-local extraction, are shown in Fig. 4.4.

Due to the big oscillation amplitudes (about $20\,$mm) the available aperture for the non-locally extracted beam is expected smaller than for the local extraction. The figure of merit used to compare the apertures, in the two different analysed cases, is the minimum acceptance in the machine, defined as

$$A_{min}(s) = \min \frac{aper_H(s) - |x(s)|}{\sigma_x(s)}, \tag{4.2}$$

where $\sigma_x(s) = \sqrt{\beta_x(s)\varepsilon_x + (D_x(s)\Delta p/p)^2}$, $D_x(s)$ is the dispersion function, ε_x the geometrical emittance, Δp/p is the fractional momentum difference and $aper_H(s)$ is the

45
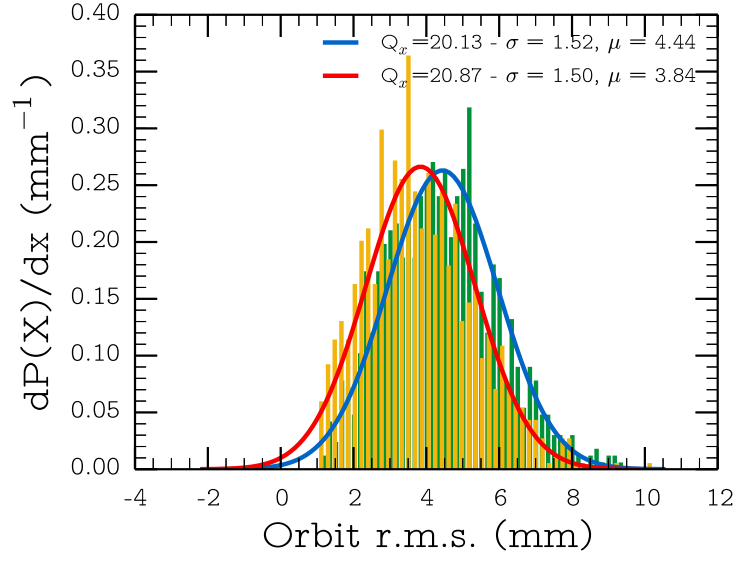
Figure 4.4 – Calculated horizontal r.m.s. orbit distributions obtained misaligning all the quadrupoles in the SPS with MAD-X. Green: $\nu_x = 20.13$. Yellow: $\nu_x = 20.87$.

horizontal mechanical aperture.
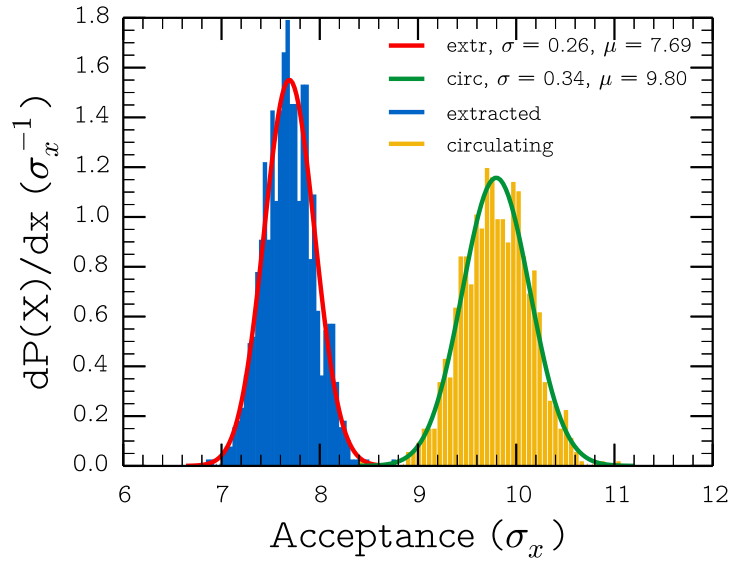
Figure 4.5 – Acceptance analysis, in the horizontal plane, for circulating and non-locally extracted beam.
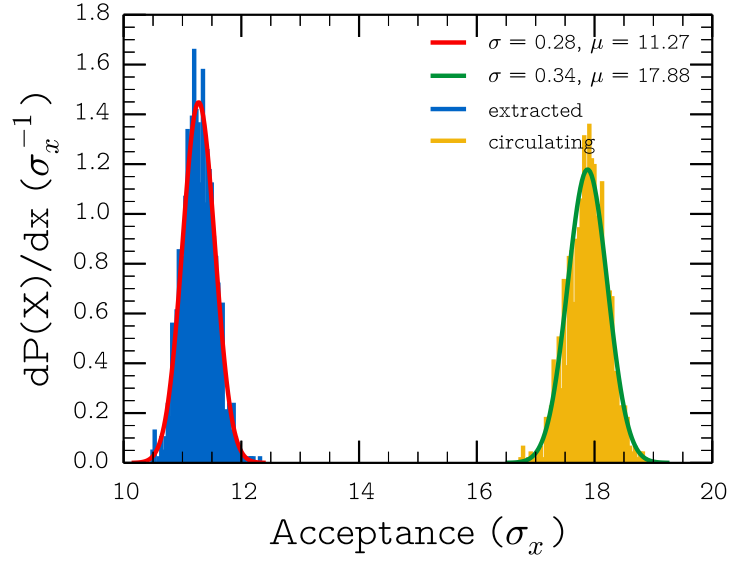
Figure 4.6 – Aperture analysis, in the horizontal plane, for circulating and normally extracted beam (present situation).

In Fig. 4.5 the distribution of the minimum acceptances is shown. The aperture bottleneck, for the extracted beam, is at the entrance of the first extraction septum (MST) in LSS6, as expected (Fig. 4.7). In some cases instead, the minimum acceptance was at the extraction septum in LSS4 or at the collimator (TCSM [21]) in LSS5 (Fig. 4.7). The 5 per mil of the simulated extraction trajectories had minimum acceptance lower than $6\,\sigma_{\mathrm{x}}$ in LSS4 or LSS5. To increase the acceptance at the TCSM a two-sextant long counter-phase bump was matched. It is a closed orbit bump with maximum amplitude of 10 mm at the QF.52, obtained using 30 horizontal correctors between LSS4 and LSS6. Also, the MSE, which is installed on a movable girder, was moved 4 mm away from the circulating beam centre. The distribution of the minimum acceptances when the beam is normally extracted from LSS6 is shown in Fig. 4.6.

The kicker strength was kept as low as possible, i.e. 33 kV, and the bump amplitude was increased (10 mm higher than the nominal) to increase the acceptance for the non-locally extracted and circulating beam.

Stability of the non-local extraction

The shot-to-shot TL variations have been extensively investigated in the last years [22] and the main source has been isolated as the current ripples of the extraction septa MSE. During the yearly technical stop between 2011 and 2012, a campaign was pursued to improve the current stability of the extraction septa. Measurements done during the
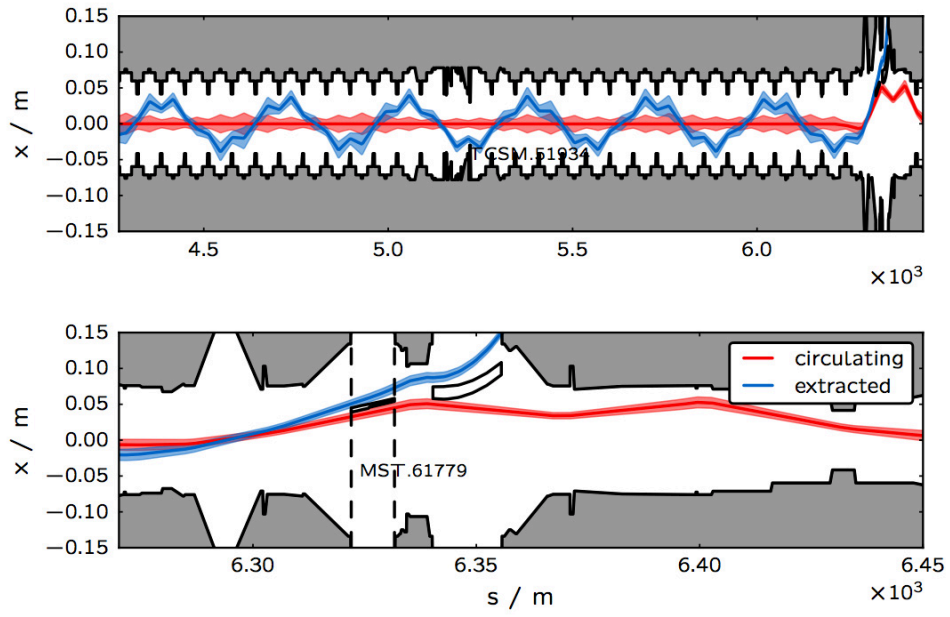
Figure 4.7 – Envelope of the extracted and circulating beam for the non-local extraction. Top - overview of the betatron oscillations performed from the non-locally extracted beam from LSS4 to LSS6. Bottom - Zoom of the extraction region in LSS6.

commissioning of LHC Run 2, confirmed the expected improvement of the shot-to-shot stability. Large beam oscillations in the TLs produce high losses at the collimators and can lead to important injection oscillations in the LHC where the available aperture is very tight [23]. The stability is one of the main concerns for the non-local extraction due to the high brightness of the transported beam.

Table 4.1 – Errors assigned to the SPS active elements. A seed from the above error analysis was used to compare both non-local and normal extraction. The horizontal orbit r.m.s. was 5.6 mm in both cases.

Errors	Distribution	Value
Quads $\Delta k/k_0$	Norm	$\sigma = $ 1e-4
Dipoles $\Delta B/B_0$	Norm	$\sigma = $ 1e-4
MKE $\Delta B/B_0$	Uniform	$\pm$1e-2
MSE $\Delta B/B_0$	Norm	$\sigma = $ 0.11e-3
MST $\Delta B/B_0$	Norm	$\sigma = $ 0.11e-3

The expected quality of the extraction and its sensitivity to the machine dynamic errors were evaluated calculating the beam position, transverse momentum, beta and dispersion functions just downstream of the MSE in LSS6 (more precisely at the monitor BTVE[1]) for 1000 different cases (Table 4.1). Non-local and local extraction simulations started with a non-zero orbit ($x_{rms} = 5.5$ mm) obtained with the same quadrupole misalignments.

Table 4.2 – Extraction stability results for both non-local and normal extracted beams. In this table, μ represent the averages of the different quantities, and σ the standard deviations.

Parameters	$\mu_{\textbf{NL}}$	$\mu_{\textbf{nom}}$	$\sigma_{\textbf{NL}}$	$\sigma_{\textbf{nom}}$
D_x (m)	-4.2e-2	-5.35e-1	1.1e-2	1.2e-2
β_x (m)	44.3	49.9	9.7e-2	9.7e-2
x (mm)	155	156	5.9e-2	2.0e-2
x' (mrad)	8.52	8.52	1.7e-3	2.3e-4
D_y (m)	-6.2e-3	-2.7e-3	3.4e-4	1.6e-4
β_y (m)	76.9	69.0	1.3e-1	1.1e-1
y (mm)	2.2	2.0	5.3e-3	4.3e-3
y' (mrad)	8.4e-2	7.4e-2	1.7e-4	1.35e-4

The results of the extraction stability analysis for the horizontal plane are shown in Fig. 4.8. Due to the larger shot-to-shot variation, observed in this set of simulations (especially for x and x'), a degradation of the current extraction stability was expected

---

[1]The BTV are Beam TV screen which use a high speed camera to record the light emitted by the interaction of the beam with screen material (usually alumina or titanium). The BTVE are BTV installed on the extraction septa in the SPS.
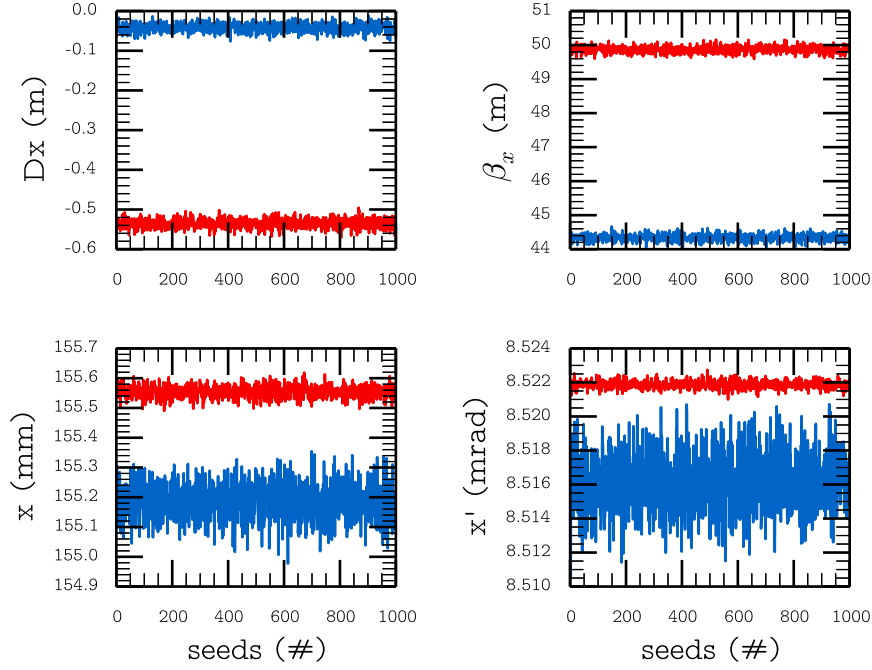
Figure 4.8 – Orbit and optic functions at the BTVE.6 calculated for 1000 different scenarios. Red: Normal extraction. Blue: Non-local extraction.

for this new concept. These values come exclusively from simulations. Measurements of the present extraction stability from LSS6 are shown in Fig. 4.9. The shot-to-shot jitter observed (one standard deviation) is 0.2 and 0.4 mm for the two monitors used. Assuming that the total extraction stability σ_{TOT} is the result of two statistically independent contributions, i.e. pure extraction stability σ_{extr} and machine stability σ_{SPS}, we can write:

$$\sigma_{TOT} = \sqrt{\sigma_{SPS}^2 + \sigma_{extr}^2}, \tag{4.3}$$

where the implicit assumption that the errors are all Normally distributed is made and σ_{extr} is σ_{NL} or σ_{nom} for the non-local extraction and the nominal extraction, respectively (Table 4.2). Then σ_{SPS} can be derived from the available measurements and the expected σ_{TOT} for the non-local extraction can be calculated. This results in $\approx 5\,\%$ larger shot-to-shot variation for the non-local extraction compared with the nominal one. Hence, the difference in the expected stability between the two extraction techniques, under the assumptions taken, can be considered negligible.
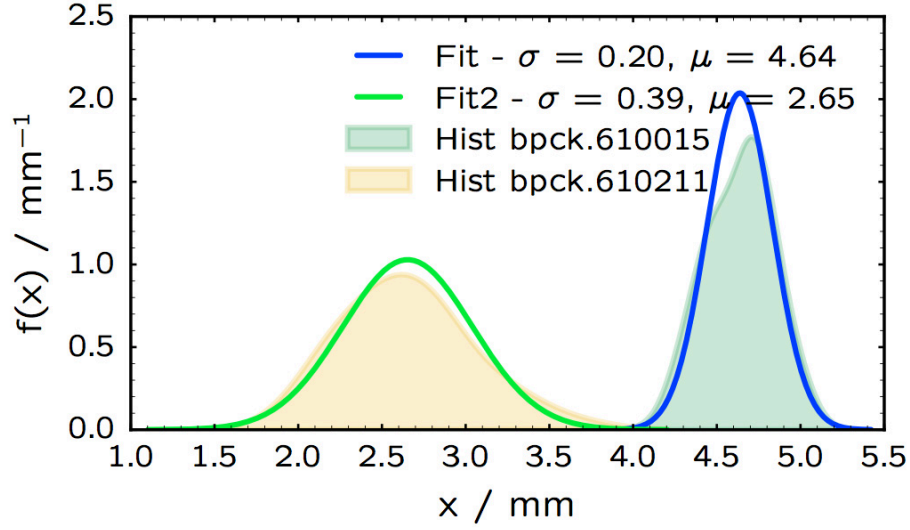
Figure 4.9 – Measurements of the beam position at the first two available monitors in TT60 over a period of two hours.

4.4 SPS orbit stability

The reproducibility at extraction is one of the key parameters for a clean and safe beam transport from the SPS to the LHC. The long term TL drifts were extensively investigated [24] and the main source was identified as the SPS orbit [25, 26]. At the end of the LHC Run 1, a set of orbits was collected and analysed [25]. Different possible sources were investigated, but none of them found to be responsible for the observed drift. In this section, the analysis of the orbit measurements taken during LHC Run 2 is presented.

4.4.1 Estimation of closed orbit at extraction

In the SPS extraction regions, the BPMs need enlarged apertures to accommodate both circulating and extracted beam. This leads to very inaccurate readings from these monitors, which are called BPCEs. It is common practice to evaluate the beam centroid position at such locations by using fitting techniques. Once the difference from a chosen reference orbit is taken, the closed orbit, at any s position in a ring, can be written as a combination of harmonic functions, exploiting the Twiss formalism. Assuming prior knowledge of the machine optics, a fitting function can be written, e.g. for the horizontal plane, as:

$$x_{CO}(s) = \sqrt{\beta_x(s)}[A\cos(\mu_x(s)) + B\sin(\mu_x(s))] + D_x(s)\delta_p \tag{4.4}$$

where β_x, μ_x and D_x are the beta-function, phase-advance and dispersion of the ring respectively. The parameters A and B are the fitting parameters together with δ_p, which represents the momentum offset of the beam. Once the fitting parameters are known,
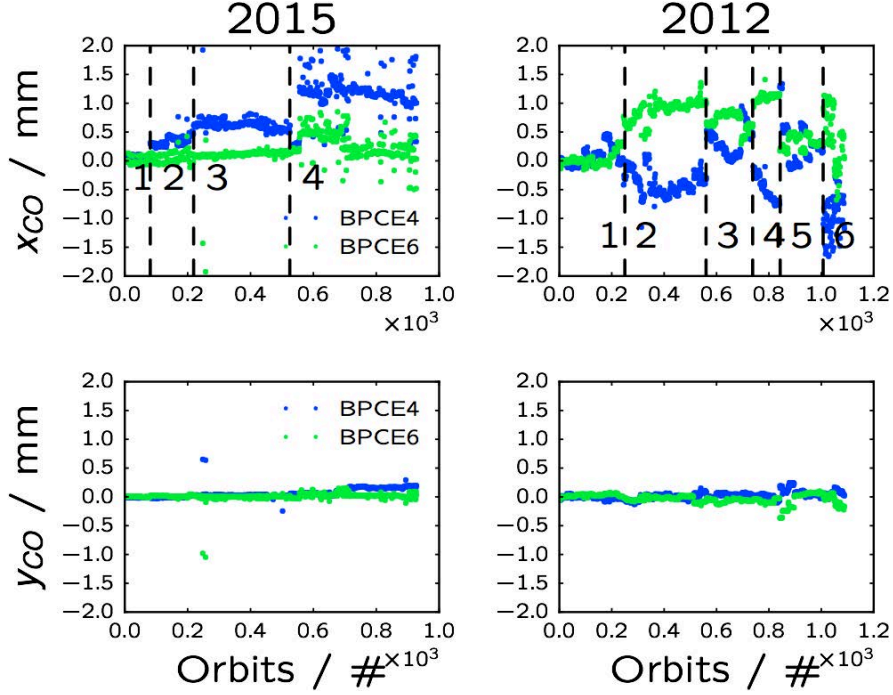
Figure 4.10 – Fitted SPS orbit at the location of the extraction BPMs, BPCE4 and BPCE6, for the available orbit sets recorded during Run 1 (2012) and Run 2 (2015). The different periods in which the data have been divided are also indicated with black dashed lines.

the closed orbit at the BPCEs can be calculated. In Fig. 4.10 the orbit at the BPCEs in LSS4 and LSS6 is shown, for the two sets of measurements, 2012 and 2015. The set from 2012 spans over two months and the one from 2015 over three months. A clear variation of maximum 1.3 mm can be observed for both sets and only in the horizontal plane. The almost unchanged vertical orbit is an indication that the source of such drift is not a geological variation of the SPS tunnel floor, which would have affected the vertical orbit as well.

4.4.2 Tune and Chromaticity variations

Due to the non ideal SPS orbit and the presence of the extraction bumps, the beam is non-centred in the quadrupoles and sextupoles. Hence, a variation of their strengths translates in a different closed orbit via feed-down effects. To assess the expected effect

of the tune variation onto the orbit at extraction, measurements have been done varying the nominal horizontal tune (20.13) and measuring the orbit. This was also done for two different settings of horizontal chromaticity, i.e. high chromaticity (HC) $Q'_x = 21.92$ and low chromaticity (LC) $Q'_x = 4.8$. The results of these measurements, are shown in Fig. 4.11. The nominal SPS orbit was reconstructed with MADX using the embedded correction algorithm SVD (Singular Value Decomposition) in order to reproduce the observed closed orbit variation as a function of the horizontal tune. Also, the measured chromaticity was reproduced using the machine sextupoles. The simulation results are plotted in Fig. 4.11 as solid lines showing a very good agreement with the measurements (dots).

The amplitude of the tune variation needed to explain the observed orbit drift is beyond what has been observed during normal operation. In fact, the tune drifts, measured during normal SPS operation, are in the range of ± 0.01 units, which would only mean a few hundred microns in the closed orbit at the BPCEs.

Another possible source of orbit variation is the change in the beam central momentum. When the LHC is requesting beam the SPS RF frequency may change by $\pm 10\,\mathrm{Hz}$, resulting in a different beam energy. This can feed back into the orbit, depending on the non-zero dispersion in the extraction regions. In addition, in case of non-zero chromaticity, the tune could be varied and some adjustments could be foreseen to bring it back to the nominal value. Measurements were done to evaluate the effect of such variation, but it was observed that the expected orbit change is more than an order of magnitude smaller than what is shown in Fig 4.10.
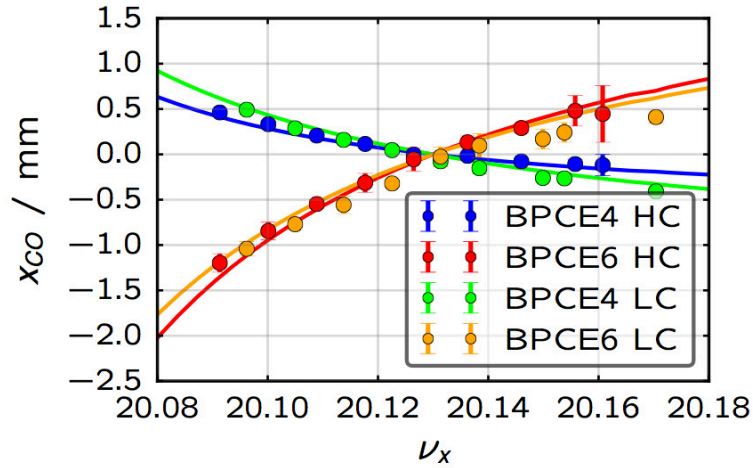
Figure 4.11 – Fitted closed orbit at the BPCE4 and BPCE6 for different tune (± 0.4) and chromaticity settings (HC and LC). In blue and red are shown the measurements results for HC settings as markers and MADX simulations as solid lines. In green and yellow the same but with LC settings.

4.4.3 Extraction septa stray field

Measurements recorded during Run 2 commissioning have shown a significant contribution of the stray field of the extraction septa on the closed orbit if not properly taken into account. During normal operation, both extraction bumps, in LSS4 and LSS6, and both extraction septa are ON at a fixed setting, and hence they cannot be considered as a source for the orbit drift over time (they can only contribute to a fixed offset). The contribution to the orbit can be up to $1\,\mathrm{mm}$ for both LSS4 and LSS6.

4.4.4 Single dipole error

The MADX model, developed in the context of the aforementioned studies, was used to investigate for possible single kick errors. As previously done in [25] for the set of orbits recorded at the end of Run 1, the Model Independent Analysis (MIA) [27] has been used to evaluate if the single dipole error assumption is valid and, if so, to isolate a possible source. MIA consists in constructing a measurements matrix M,

$$
M = \begin{pmatrix}
x_{1,BPM.1} & x_{1,BPM.2} & \cdots & x_{1,BPM.M} \\
x_{2,BPM.1} & x_{2,BPM.2} & \cdots & x_{2,BPM.M} \\
\vdots & \vdots & \vdots & \vdots \\
x_{N,BPM.1} & x_{N,BPM.2} & \cdots & x_{N,BPM.M}
\end{pmatrix}
\tag{4.5}
$$

where the N measured orbits at the M BPMs are vertically stacked. Then, via SVD, the matrix M is decomposed as: $M = USV^T$, where U and V are the orthogonal matrices of the left and right eigenvectors, respectively, and S is the diagonal matrix of the singular-values λ_j. The left and the right eigenvectors represent the temporal and spatial modes respectively. The low order spatial modes, which correspond to the highest singular-values, can be used to identify the source of errors.

In Fig. 4.12 the amplitude of the singular-values, for the horizontal plane, for both sets of orbits are shown. In both cases, more than one dominant singular-value is present, hence sub-periods can be considered in order to have only one main source of error. The 2015 set can be divided in four sub-sets, as marked in Fig. 4.10 with dashed lines, because the orbit at the extraction BPMs does not vary significantly in these periods. The SVD analysis is then repeated for each sub-set and the resulting singular-values are shown in Fig. 4.13. Only for *period 3*, which corresponds to 1-2 August 2015, there is one dominant singular-value, indicating only one main source. The MADX correction routine MICADO is used to identify such a source, which indicates the LSS6 half-cell 631-632 (Fig. 4.14). Every other element with phase-advance close to $\mu_x = n0.5 + 0.13 + m$, with m and n integers, can produce an equivalent betatron oscillation. In fact, the second best group of correctors belongs to the LSS1 half-cell 111-112, which has an equivalent
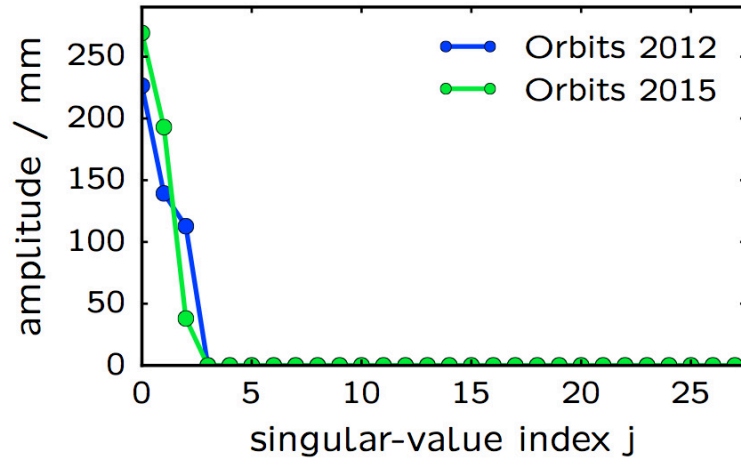
Figure 4.12 – Singular-values plot for the two available orbit sets, 2012 and 2015.
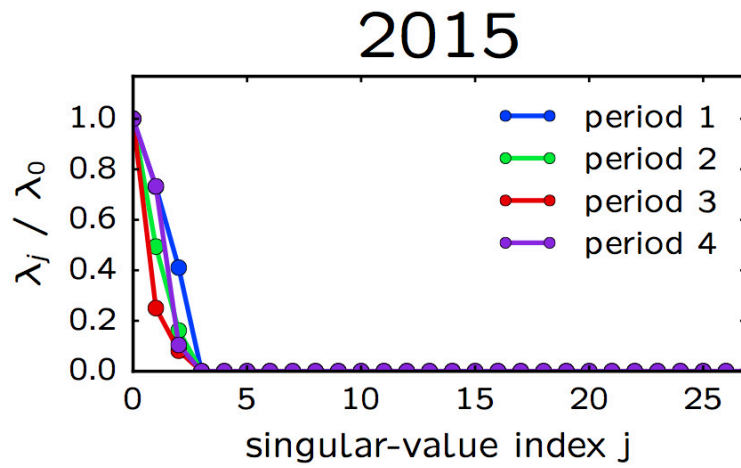
Figure 4.13 – Singular-value plot for the orbits set from Run 2 divided in sub-periods as proposed in Fig.4.10.
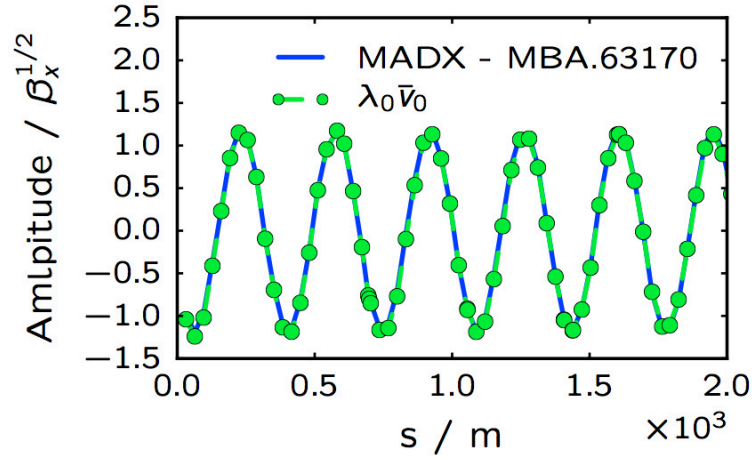
Figure 4.14 – Dominant eigenmode from the 2015 set period 3. The dashed green line represents dominant eigenvector times the corresponding singular-value and the solid blue line is the betatron oscillation originated from the MBA.63170 with a kick of 110 µrad. Both are normalised to the square root of the local beta-function.

phase-advance. The oscillation originating from such elements is plotted, together with the 0-mode, in Fig. 4.15. A very good agreement can be noticed when comparing the sub-period 3 0-mode and the orbit generated by the MBA.63170, or equivalent elements. The same oscillation is also compared with the 0-mode of the whole 2015 set (Fig.4.15), but in this case the missing contribution from another source is clear.

The set of orbits from Run 1 has been processed in the same manner with the intent of finding some analogies with more recent data. Also in this case, a division in sub-periods was necessary to obtain only one dominant mode. The 2012 set overlaps with the one analysed and discussed in [25], although it covers a bigger time span. The best correctors for the periods where only one source is clearly dominating belong to the half-cell in LSS6 634-635, which do not appear in the 2015 set.

4.5 Experimental results of non-local extraction towards LHC

The concept presented in Sec. 4.3 has been tested in the SPS in two occasions: *15th May and 18th August 2015*.

Such a measurement is complicated from the set-up point of view. Some of the interlocks that are usually monitoring the extraction process have to be disabled and this is possible only due to the low intensity used. This means that meticulous attention is needed to re-set the SPS in a safe state afterwards. Also, the SPS was isolated from its LHC TLs
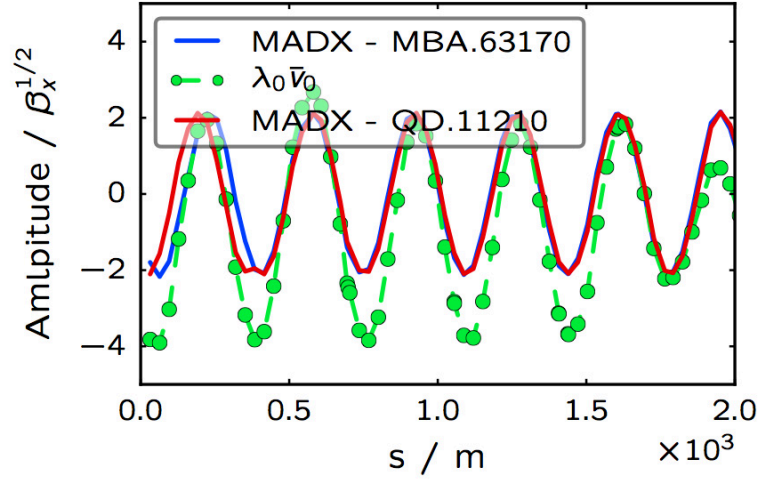
Figure 4.15 – Dominant eigenmode from the 2015 set. The dashed green line represents dominant eigenvector times the corresponding singular-value. The solid blue and red lines are betatron oscillations originated from the MBA.63170, with a kick of 200 µrad, and the QD.11210, with an equivalent kick of 150 µrad. All of them are normalised to the square root of the local beta-function.

closing the movable absorbers (TED) available just after the LSS4 and LSS6 extraction channels [16].

As previously discussed, the needed horizontal working point is very different from any operational one. This can be directly changed on-line varying the main quadrupoles current.

The extraction bump needed for this new working point was calculated. As previously discussed, the bump amplitude had to be set 10 mm larger than during nominal operation. The measured SPS closed orbit with the non-local extraction bump active is shown in Fig. 4.16. The bump non-closure was also measured and was found to be < 0.5 mm, which is the standard value for the SPS extraction bumps.

Once the TEDs are closed, the new working point set-up and the extraction bump switched on, the extraction using the MKE.4 can be performed. In order to verify that the beam is correctly extracted, the first available BTVE screen, just after the LSS6 septa, is moved on the beam trajectory. The measurements of the first attempts of the non-local extractions of B1 using the MKE.4 are shown in Fig. 4.17. The position of the beam recorded at this BTVE is in complete agreement with what is usually observed with standard LHC extraction.
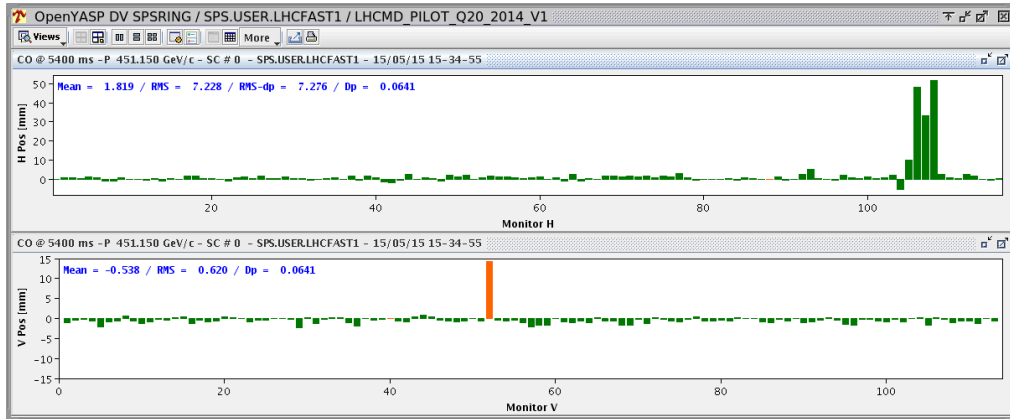
Figure 4.16 – Screen-shot of the SPS steering application showing the closed orbit just before extraction. The CO is shown as difference with respect to the nominal one, in order to evaluate the bump shape and its closure.
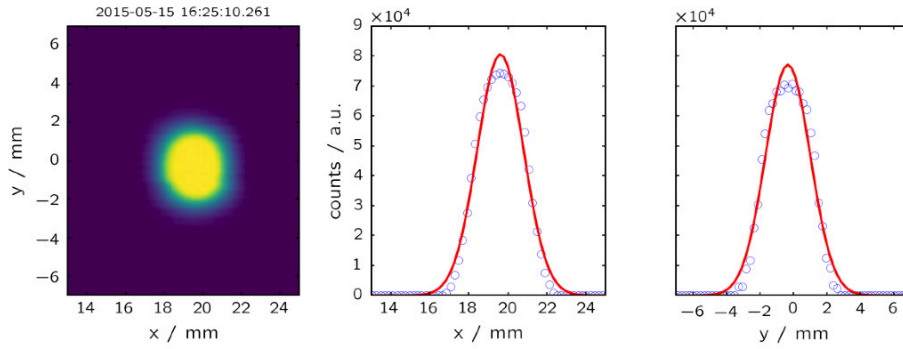
Figure 4.17 – Measurements of the first screen installed at the extraction from LSS6 when B1 was non-locally extracted.

4.6 Conclusions

The foreseen brightness increase for the HL-LHC era demands an impedance reduction to increase the instability threshold. The SPS kickers are among the main contributors to the SPS transverse impedance. Among those, the extraction kickers are the worst for the beam induced impedance. In this chapter, the possibility to use only one of the MKEs to extract both B1 and B2 towards the LHC has been shown.

The concept of non-local extraction permits to exploit the SPS FODO lattice periodicity to remove the MKE installed in LSS6. Simulations show the feasibility of the non-local extraction of B1 when the fractional part of the horizontal tune is changed.

The Monte Carlo simulations show an aperture reduction, for both extracted and circulating beam, in case of non-local extraction. Also, the extraction stability calculated from measurements and simulations is expected to be slightly worse (about 5 %) than the one guaranteed by the current system. Such a reduction is considered to be small enough to not worsen the delivered beam quality to the LHC.

The SPS orbit long term drift can be very critical for the possible operation of the non-local extraction and nevertheless for the current extraction. Different orbit drift sources were considered and measurements carried out to try to explain the observations. No source has been isolated yet as the sole cause of the orbit drifts. The possible tune variations could only partially account for the observed drift.

The possibility of a single dipole error was also investigated leading to two possible candidates. More orbits will be recorded in the ongoing LHC physics run to try to corroborate these results.

Finally, measurements with beam confirmed the simulation results of the feasibility of the non-local extraction. In fact, B1 was extracted using the MKE.4 at the first attempt with the set-up explored in simulations. Such an extraction was performed multiple times and no major problems were found. The potential big gain in terms of impedance reduction has to be carefully evaluated together with the possible operational difficulties and increased complexity (controls, machine protection).

CHAPTER 5

Non-local non-resonant slow extraction

Since the early 90s, the possibility of extracting high energetic particles from the SPS aperture by means of silicon bent crystals has been explored. The channelling effect of a bent crystal can strongly deflect primary protons and hence eject them from a synchrotron. Many studies and experiments have been carried out. As summarised in [28, 29, 30, 31], diffusion extraction of 120 and 270 GeV protons was proved in the SPS. In these cases, scintillation counters placed downstream of the crystal were used to profile the channelled beam.

Currently, in the SPS, the UA9 [21, 32] experiment is evaluating the possibility to use bent silicon crystals as primary collimators for the LHC. Exploiting the non-local extraction technique presented in the previous chapter, and the UA9 crystal installation, a non-local non-resonant slow extraction from the SPS can be achieved. This also represents a first step in the development of a way to reduce slow extraction losses, as it will be shown in the next chapter. In this chapter, the possibility to extract particles from the SPS LSS2 using crystals in conjunction with conventional septa has been investigated. Detailed descriptions of the simulations and measurements of crystal assisted extraction from the SPS are presented.

5.1 UA9 experimental setup in the SPS

A schematic view of the UA9 experiment installation in the SPS LSS5 (half-cell 517/518) is shown in Fig. 5.1. The experiment elements and instruments comprise two goniometers for a multi- and a single-crystal setup, different detectors to precisely characterise the observables and absorbers and scrapers to stop the channelled beam. It has to be highlighted that the crystals in this area are installed towards the centre of the SPS (negative x in MADX convention).

A short introduction to silicon bent crystals is presented in the following section. The collimators and absorbers installed in the UA9 are: TCSM, TACW and TAL. All of them are equipped with LHC Beam Loss Monitors (BLM), which are much more sensitive
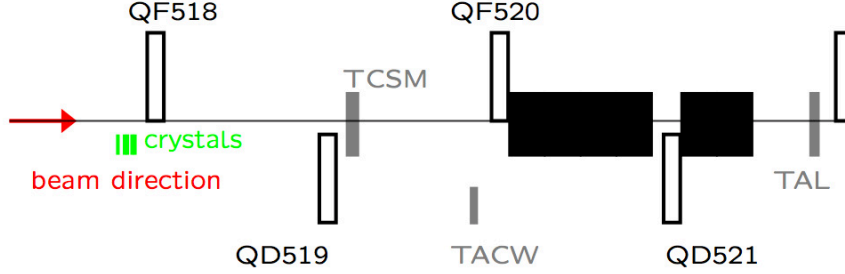
Figure 5.1 – Schematic representation of the UA9 experiment installation at the SPS.

than SPS BLMs. The TCSM is an LHC primary collimator [16] equipped with a BPM at its entrance. It is a 1 m graphite block with two horizontally placed jaws. It is only used for dedicated measurements campaigns and not during normal SPS operation. The TACW is an LHC secondary collimator used to stop the crystal channelled beam during UA9 data taking. It is a 60 cm tungsten block and it is preceded by a high precision pixel detector. The experimental installation is terminated with the TAL, another LHC secondary collimator.

5.2 Introduction to silicon bent crystals
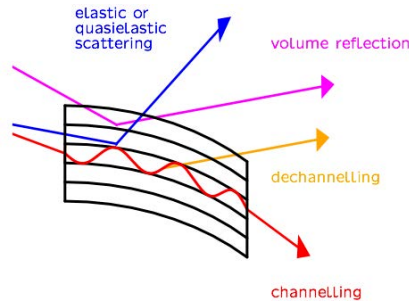
Figure 5.2 – Schematic view of the main coherent processes taking place when positive particles interact with a silicon bent crystal.

The highly ordered atomic structure of crystals is the reason behind the channelling effect.

Essentially, particles that interact with this crystalline structure and with a transverse momentum that is smaller in module than the crystal critical angle are trapped in the transverse potential wells. If the particle transverse energy does not go above a certain threshold, it will be trapped and go trough the crystal staying confined between two crystal planes. When crystals are bent, large deflection angles can be then achieved exploiting the same principle. This is in fact one of the main reason why the concept of crystal collimation has been developed [21].

A bent crystal deflects the part of the intercepted beam by a certain angle. A schematic view of a bent crystal is shown in Fig. 5.2. Here, the different processes that generate different deflection angles of the particles interacting with the crystal lattice are shown. Such processes can be divided in three regimes (Fig. 5.3):

1. Transition (amorphous and volume reflection): all the processes that lead to a smaller deflection angle compared to channelling. Particles are scattered along the bent crystal and the output angle does not differ much from the initial one. The main contributors to such a regime are volume reflection and elastic (or quasi-elastic) scattering. In case of volume reflection, the mean value of the deflection angle is opposite to the deflection angle due to channelling, as expected from simple geometrical considerations.

2. De-channelling: particles that were trapped in between the crystalline planes but, before reaching the end of the crystal, are ejected from the crystalline planes and hence leave the crystal with a deflection halfway between zero and the nominal channelling angle.

3. Channelling: particles that are trapped in between crystalline planes until they leave the crystal and thus experience the full deflection angle. The ratio between the total number of particles interacting with the crystal and the number of channelled particles is defined as the crystal channelling efficiency.

The probability that different processes occur is a function of the incidence angle. From measurements performed in 2014 on a UA9 silicon bent crystal (SFT45) [33] and available in [32], a map of the relation between output and input angles of particles into the crystal was built (Fig. 5.3 [33]). The different deflection regimes are clearly visible and, very important for the following studies, the results refer to single pass effects measured on an experimental transfer line in the NA (H8).

From the 2D histogram of Fig. 5.3, limiting the impact angles to those expected from the analysed beam, a 1D pdf can be derived ($\pm 10\,\mu$rad)[32]. The pdf of the expected deflection given from the crystal is shown in Fig. 5.4 as blue solid line. From this the effect of a crystal SFT45 on the intercepted beam can be parametrised and used to understand the effect on the beam dynamics when using crystals. Such a pdf will be used in the following section.

Two approximations are used to describe the beam-crystal interaction: ideal bent crystal

(IBC) and non-ideal bent crystal (nIBC). In case of IBC, the deflection angle given to a particle interacting with the crystal is randomly picked from Gaussianly distributed kicks with average $\mu_{\Delta\theta} = 160\,\mu$rad and standard deviation $\sigma_{\Delta\theta} = 16\,\mu$rad (Fig. 5.4, red line). In this case the assumed efficiency is a non-realistic 100 %. For the nIBC approximation instead, the kick experienced by each particle is chosen from the pdf shown in Fig. 5.4 as blue line. This simple approach is sufficient for the level of approximation that these studies are aiming for.

Recently, a significant effort has been put in place in the studies of the concept of crystal collimation [21, 34, 35]. The phenomenon of high energy particles channelling by means of silicon bent crystals has been experimentally demonstrated both in the SPS and in the LHC [21, 34, 35].
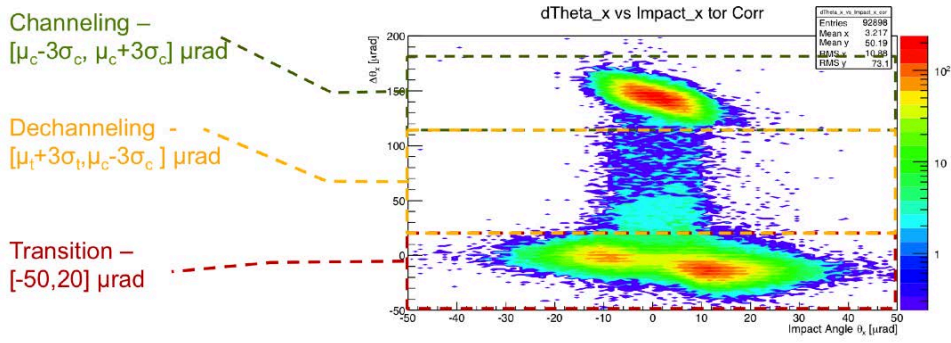
Figure 5.3 – 2D histogram of the deflection angle of the crystal as function of the impacting angle [33].
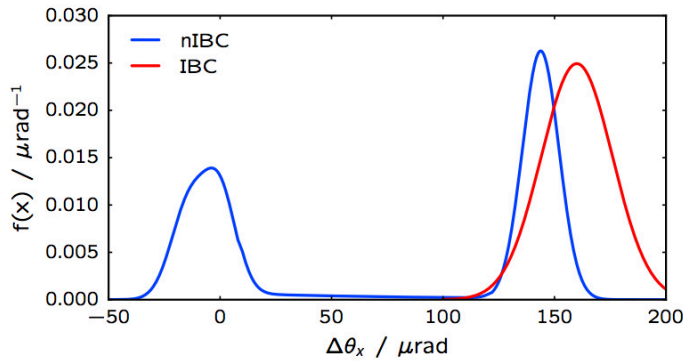
Figure 5.4 – Probability density function of simulated kick from a thin crystal for the cases of an ideal bent crystal (red) and a non-ideal bent crystal (blue).

5.3 Extraction concept

In order to exploit the UA9 experimental setup in the SPS for slow extraction from LSS2, the concept of non-local extraction can be used. An ad-hoc machine horizontal working point is used to optimise the phase advance between the crystal and the LSS2 electrostatic septum. The part of the beam that interacting with the crystal is channelled will gain enough displacement to "jump" the ZS wires. Hence, with the help of an extraction bump, the beam halo can be extracted turn by turn, resulting in a constant flux of particles sent down TT20.

The definitions of beam halo are quite disparate in literature, although usually they agree in saying that it represents less than 1% of the total beam population. The beam halo is arbitrarily defined here as the particles that lie at an amplitude above 3σ from the core. A usual configuration of the UA9 experiments sees the crystal sitting at 6σ to 7σ from the beam centre. The beam halo hits the crystal and a downstream absorber stops the channelled beam (TACW) inside the SPS apertures, where the channelled beamlet has reached enough separation from the circulating beam. A detector is placed just upstream of the TACW to measure the position of the halo channelled by the crystal.

If the collimator is removed, the channelled beamlet can circulate and, if the displacement of the channelled beamlet is sufficiently large to jump the ZS wires, a slow extraction can be performed.

5.4 Working point optimisation

In a perfect linear machine, the transport of the transverse coordinates can be done using Eq. (2.20). For the purpose of the non-resonant crystal assisted extraction, the optimum necessary phase advance between the crystal and the ZS has to be calculated. From Eq. (2.20) the displacement at the electrostatic septum, when a kick θ is impressed to a particle with initial coordinates (x_1, x_1'), can be written as:

$$x_{ZS} = x_1 \sqrt{\frac{\beta_{ZS}}{\beta_1}} (\cos(\Delta\psi) + \alpha_1 \sin(\Delta\psi)) + (x_1' + \theta)\sqrt{\beta_1 \beta_{ZS}} \sin(\Delta\psi). \tag{5.1}$$

The deflection angle of the channelled particles can be between $100\,\mu$rad to $200\,\mu$rad (for the crystals installed into the SPS). From Eq. (5.1) the optimum phase advance between the crystal and the ZS can be calculated (Fig. 5.5). Taking a 1D cut of the plot in Fig. 5.5 for $x_1 = -7\sigma$ (Fig. 5.6), the phase advance that leads to the maximum displacement at the ZS is calculated, as $\Delta\psi_{opt} \equiv \Delta\psi = 234°\,(0.65\,2\pi)$.

Using $\Delta\psi_{opt}$ as the target phase advance between the crystal and the ZS, the operational SPS optics were checked for the best match ($\nu_x = [20.13, 26.13, 26.62]$ which corresponds to $\Delta\psi = [320, 300, 25]°$). None of them satisfy the requirements, hence all possible horizontal working points between 20 and 28 were checked for the best match. The horizontal tunes that best fit is 21.62. Such a tune could be, in principle, be used for
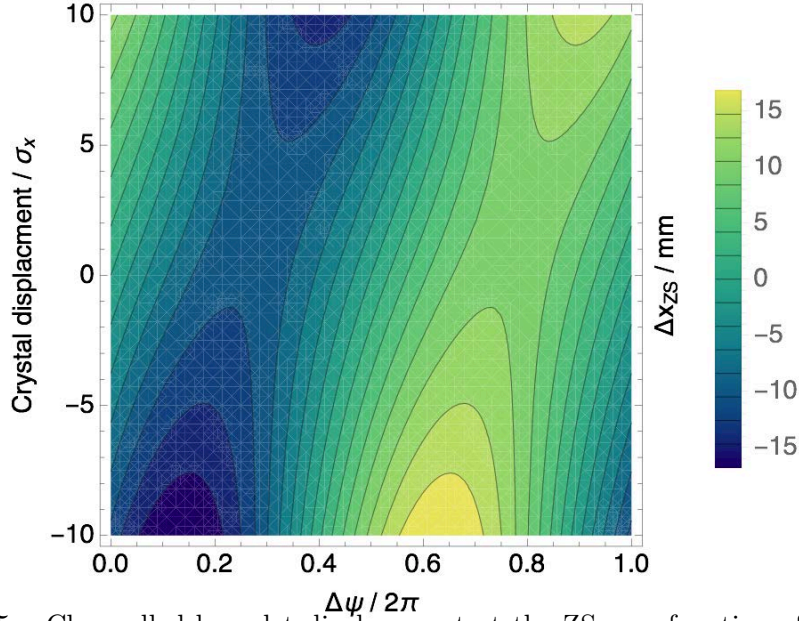
Figure 5.5 – Channelled beamlet displacement at the ZS as a function of the crystal position and the phase advance between crystal and ZS. Here the assumption that the β-function at the crystal and the ZS do not change with the working point has been made.

this extraction, although a working point with 21 as integer part has never been tested operationally. To simplify eventual measurements with the machine, new possibilities were investigated.

A very promising solution is to extract the channelled beamlet one and half turns after it has been deflected by the crystal, and not directly. In this non-local extraction configuration, the horizontal tune which guarantees the best phase advance between the ZS and the crystal is 26.62 (SFTPRO tune). For this working point and under these conditions, $\Delta\psi = 252°$. Due to the familiarity of this optics with the SPS, this was chosen as working point for this extraction concept.

5.5   SPS non-local non-resonant slow extraction

Once the optics is chosen, tracking simulations with MADX+*pycollimate* were performed to evaluate the feasibility of this concept.

To calculate the optimum extraction bump shape, a few considerations have been made. Due to the beam angular spread, not only the centre part of the beam intercepted by the crystal, but also the extrema have to be evaluated. In fact, the particle that has the largest normalised transverse momentum and smaller amplitude will be the one defining how close the extracted beamlet will be to the ZS wires (Fig. 5.7 and 5.10).
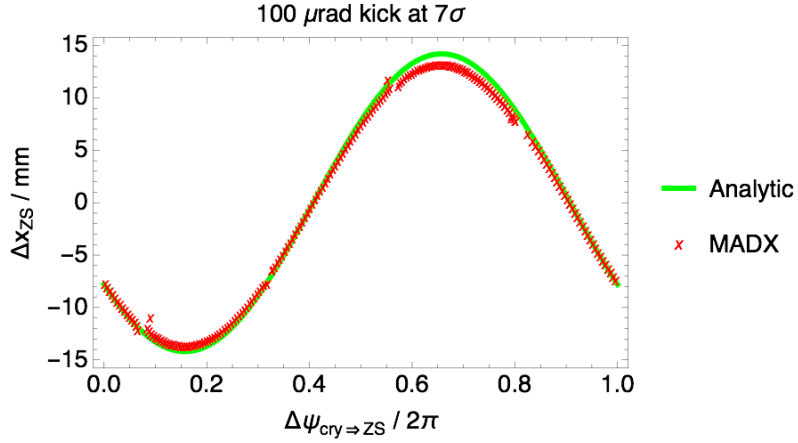
Figure 5.6 – Displacement of the channelled beamlet from the circulating beam at the ZS as a function of the phase advance between crystal and ZS. Here the case of a crystal at 7σ from the beam centre and with a mean channelling angle of $100\,\mu$rad is shown.
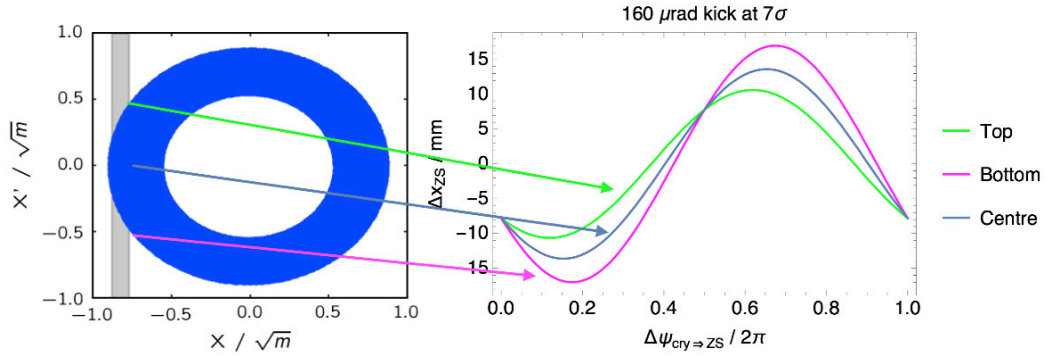
Figure 5.7 – Displacement from the beam centre, at the ZS, for the different parts of the channelled beamlet as a function of the phase advance crystal-ZS. A uniform hollow distribution between 5 and 8σ is shown.

Taking this into account, the optimum extraction bump has to move the circulating beam at 10σ from the ZS. In Fig. 5.9, the trajectory of the channelled beamlet is shown together with the circulating beam for one and half turn after interacting with the crystal. It has to be noted that the crystal has to be used in a "single-pass mode", meaning that particles that interact with it and get a deflection close to the average channelling angle will be extracted without re-interacting with the crystal. This is very important since the single-turn efficiency of the crystal is a key parameter.

Using this model, an initial hollow Gaussian particle distribution between 5σ and 8σ is
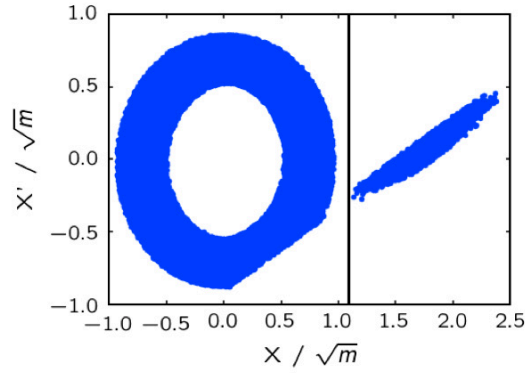
Figure 5.8 – Beam halo at the ZS in lSS2 after deflection at the crystal in LSS5 for an optimal phase advance crystal-ZS.
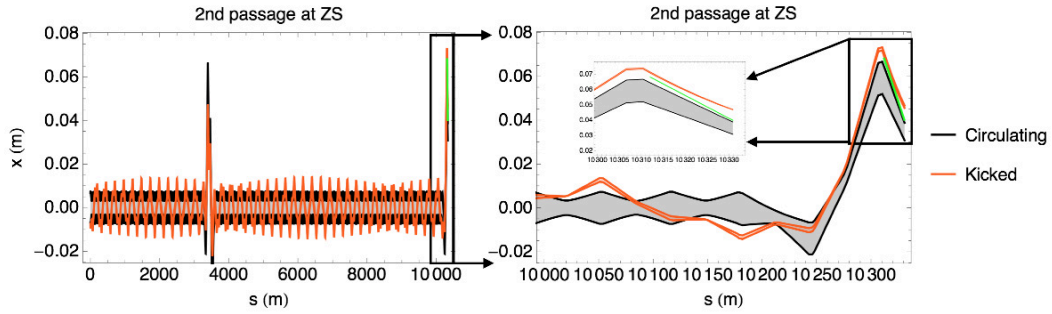
Figure 5.9 – In black the circulating beam envelope ($7\,\sigma$) is plotted together with the channelled beamlet (orange). A zoom at the ZS at second passage of the beamlet is shown.

tracked for a few turns to evaluate the beam profile at the ZS. The expected phase space at the ZS for a non-local non-resonant crystal extraction is shown in Fig. 5.10 - left. The expected beam profile at the ZS is shown in Fig. 5.10 - right.

Due to the non-ideal crystal efficiency, particles will populate the region between the channelled beamlet and the circulating beam. For the proposed SPS test, the particle density at ZS wires is expected to be lower than during standard SFTPRO slow extraction. This is the case for two reasons: the extraction rate is much slower than in a resonant extraction and the density of non-channelled particles is much lower than the usual separatrix population (see next chapter).
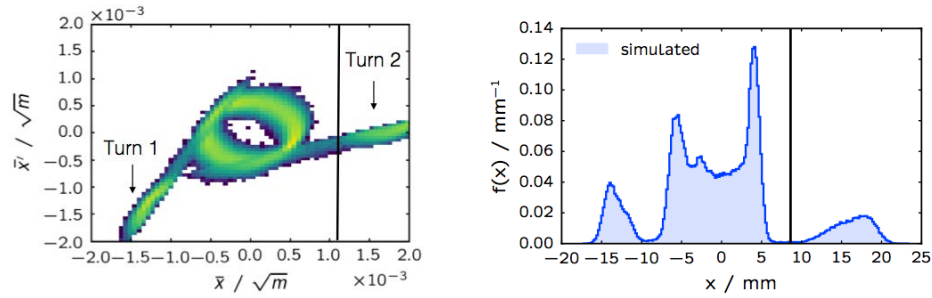
Figure 5.10 – Left - Normalised phase space at the ZS after beam-crystal interaction. The particle distribution has been extracted two turns after the crystal touched the beam halo. Right - Beam profile at the ZS after beam-crystal interaction. A clear intensity dip at the region of the ZS wires can be observed.

5.6 Experimental results with beam in the SPS

On *20th July 2016* a first dedicated MD was allocated to prove the feasibility of the non-local non-resonant crystal assisted extraction. In order to be able to use the installed crystal, the SPS was used as a storage ring, meaning that the beam was kept at a constant energy in the machine for hours instead of the usual cycles which only last a few seconds. An LHC-like bunch ($5 \times 10^9 - 1 \times 10^{11}$ protons in $\epsilon_N = 3.5$ mmmrad maximum) was accelerated up to $270\,\mathrm{GeV}$ and then stored. At this energy, the extraction bumpers and septa can be operated in DC mode.

Due to the high density of the beam used[1], it was decided to stage the proof-of-principle measurements in two steps:

- A first one to only evaluate the effect of the extraction bump on the channelling angle and the model prediction of the channelled beamlet position (ZS moved out from the extraction channel) without performing the actual extraction.

---

[1]Usually the ZS is exposed to debunched beam and on resonance, in this case the beam is an LHC type, hence concentrated in maximum $5\,\mathrm{ns}$.

- A second one, to test the complete extraction but using a lower intensity beam (PILOT, $\approx 5 \times 10^9$ protons).

This was done because the experiments with crystals were done with INDIV ($I_b \approx 1 \times 10^{11}$ protons) or higher intensity beams and this can be harmful for the delicate ZS wires. In this first MD, only the first step was performed.

The SFTPRO optics was used for the MD, i.e. $\nu_x = 26.62$ and $\nu_y = 26.58$. The extraction bump used for the simulations was also used for the measurements. Its closure was evaluated and a maximum leakage of 0.5 mm was observed when it was energised at its nominal value (47 mm). This is the normal orbit oscillation leakage for SPS extraction bumpers.

Then, the effect of the extraction bump on the crystal angular alignment was tested. The bump leakage measured half-cell after the crystal was 100 µm. The optimum crystal angular alignment with beam, though, was found to be unchanged. This is a very interesting results, because the sensitivity of the crystal alignment to the beam was one of the main concerns for operation. The orbit offset could be compensated by displacing the crystal laterally (without changing its angular alignment).

Due to the impossibility to extract , the channelled beam position after one turn was measured at the LHC collimator (TCSM) in LSS5 (Fig. 5.1). Using the TAL, the channelled beamlet was stopped after one interaction with the crystal. In this way, most of the channelled particles interact with the crystal only once (Fig. 5.11 - left).

The channelled beam was then profiled by scanning the position of the external jaw of
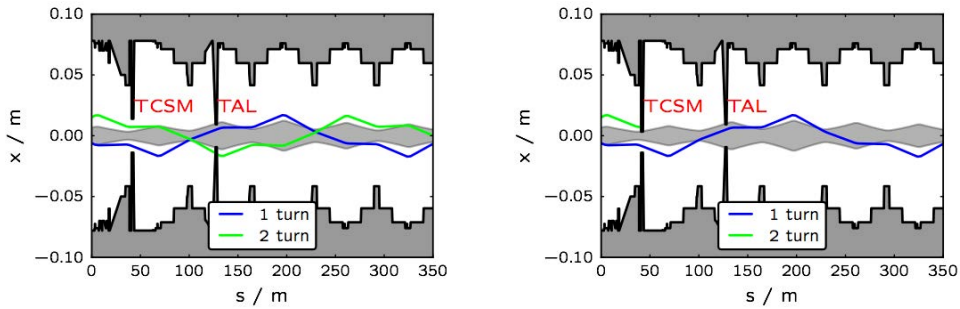
Figure 5.11 – Schematic view of the beam in the SPS when the profiling of the beamlet with the TCSM was performed. Left - TAL absorber closed to $7\,\sigma$ to intercept the channelled beamlet at the second turn. Right - beam profiling with the left jaw of the TCSM stopped when the circulating beam was reached.

the TCSM, as shown in Fig. 5.11 - right. In Fig. 5.12, the collimator jaw position and the losses at the TCSM, recorded during the MD, are plotted as a function of time. The collimator jaw is moved towards the circulating beam (grey shaded area). The jaw is stopped before reaching the circulating beam in order to preserve it (green shaded area). The last movement of the jaw increased the losses of more than an order of magnitude

(red shaded area). This was the indication that the circulating beam was touched by the collimator.
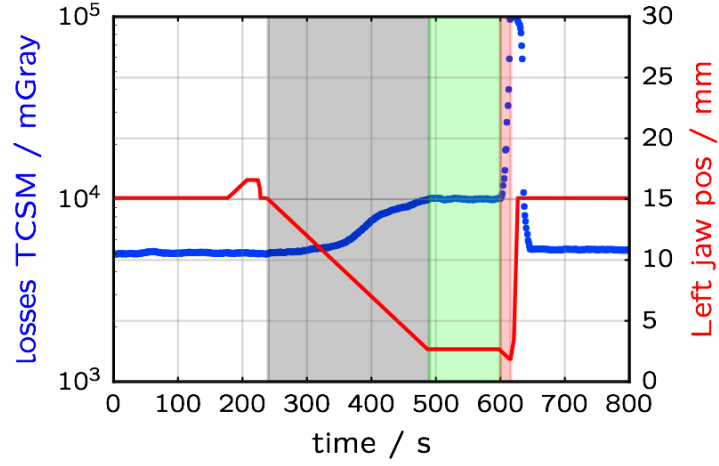
Figure 5.12 – Raw experimental data, Beam Loss Monitor (BLM) and jaw position readings, of the beamlet profiling measurement one turn after being channelled.
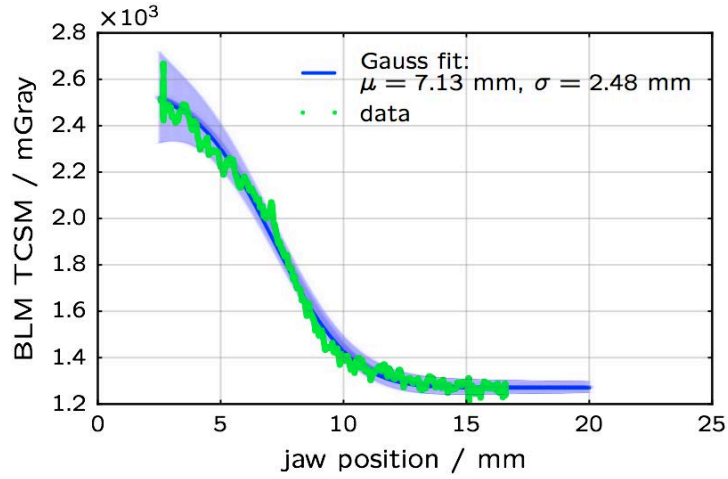
Figure 5.13 – Measurements and fit from the automatic scan of the channelled beamlet with the left jaw of the TCSM. The date corresponds to the one indicated with grey shaded area in Fig. 5.12.

Using the BLM readings when the collimator was moving from its initial position towards

the beam centre, with an appropriate fit, the beam shape, and its average displacement, can be calculated (Fig, 5.13). In Fig. 5.13 errors on the collimator jaw position, beam jitter, fit errors (at $5\,\sigma$) and BLM reading uncertainty have been included in the error bars of the fitting function. From the fit, the beamlet centre is $(7.1 \pm 0.2)\,$mm. From simulations instead, the expected beamlet centre for a channelling angle of $175\,$μrad is $7.25\,$mm.

Such measurements suggest a wider beamlet than expected from simulations (Fig. 5.14-left). The results of the simulations and measurements are summarised in Table 5.1. The main reason is thought to be due to the background signal originated by the interaction of the channelled beam with the TAL absorber. In fact, the simulation results shown in Fig. 5.14-right give a much better agreement with measurements including such absorber in the simulations and tracking for 20 turns. The effect of the absorber used to stop the beamlet after two turns is emphasised observing the phase space distribution (Fig. 5.15). The noise observed in the measurements could probably be better reproduced in simulations increasing the number of particles and the number of turns, although the achieved agreement was already satisfactory.

Table 5.1 – Comparison between measurements and simulations of the central position and width of the channelled beam after one SPS revolution.

	μ (mm)	σ (mm)
Simulations	7.25	1.71
Measurements	7.1±0.2	2.48±0.5
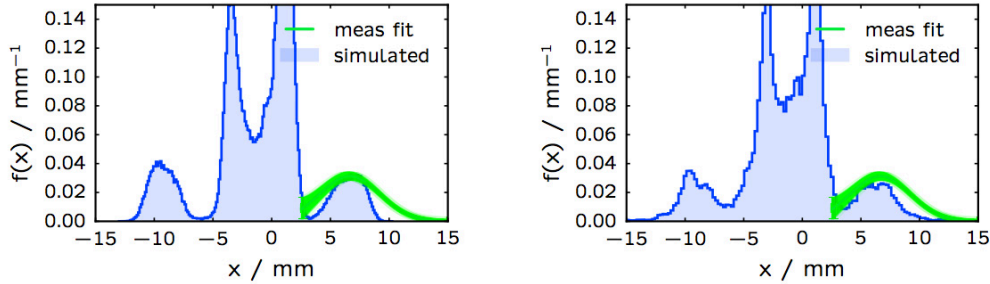
Figure 5.14 – Beam profile at the TCSM from measurements (green) and simulations (blue), without including (left) and including (right) the scattering from the TAL.

On the *28th November 2016* a second MD was carried out. In this measurement session, a PILOT beam was used to demonstrate the possibility to extract primary protons from LSS2 using the UA9 crystals in LSS5. The same procedure described above was repeated, but with the ZS at its "in-beam" position. All the extraction elements, as well as TT20, were switched on.

With the extraction bump in LSS2 already powered at its nominal value the MD started
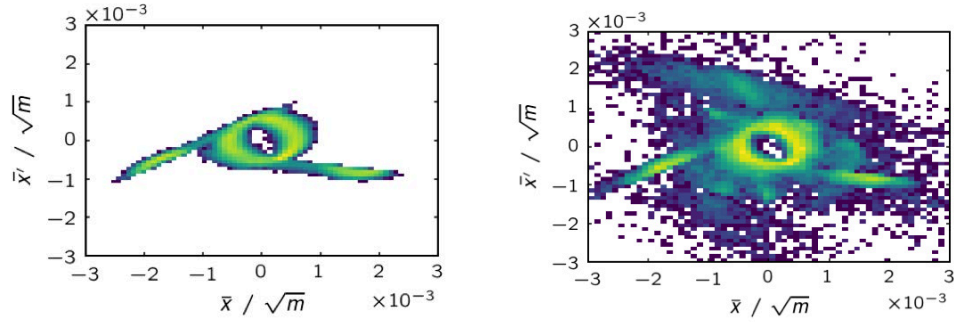
Figure 5.15 – Normalised phase space at the TCSM location corresponding to the beam profiles shown in Fig. 5.14, left without and right with scattering from TAL.

by setting up the crystal alignment with the beam in order to have the optimum angle for channelling. This was to avoid perturbing the channelling efficiency when turning on the extraction bump. The TACW was initially kept in to constrain the channelled beam to the UA9 experimental region.

A so-called Cherenkov proton Flux Measurement (CpFM) detector was installed in TT20 to detect the extracted beam for the non-local crystal assisted slow extraction tests. Such a detector comprises a Cherenkov radiator bar made of quartz that is installed inside the primary vacuum; it is movable and hence a scan across the vacuum chamber aperture is possible to evaluate the beam position and shape. It is capable of detecting 2 to 200 protons per pulse.

The MD was divided in a series of measurements aimed to demonstrate the presence of channelled primary beam in TT20:

- Correlation between TACW position and CpFM reading;

- Channelled beam profile reconstruction using the CpFM in TT20;

- Correlation between TCSM position and CpFM reading;

- Imaging of the third turn using MEDIPIX with extraction bump on and off.

For the first test, the TACW was initially positioned such that the channelled beam was intercepted and only background measured at the CpFM. Then, the TACW was retracted and the particle flux measured in TT20 increased accordingly. In Fig. 5.16 the measured flux on the CpFM in TT20 is plotted as a function of the TACW position. This is the first proof of the presence of the channelled beam in TT20.

Finally, the CpFM was moved across the beam pipe and a profile of the extracted beamlet obtained (Fig. 5.17).
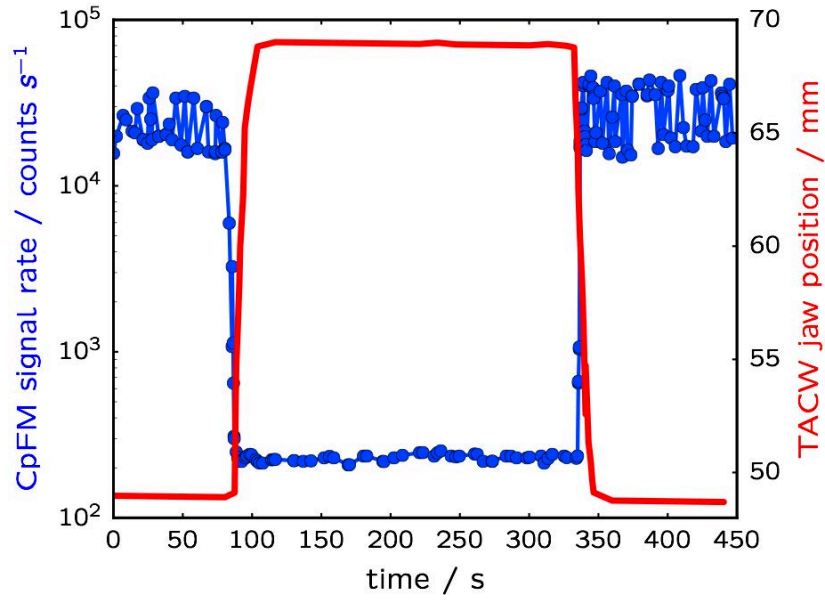
Figure 5.16 – Correlation plot of the presence of primary protons in TT20 with the TACW absorber position. It can be seen that when the TACW is fully retracted, i.e. at 48.9 mm, primary protons are seen in TT20. Instead, when the TACW is close to the beam, i.e. 68.8 mm, there is no beam extracted form LSS2 [*Courtesy of F. Addesa and UA9 collaboration*].
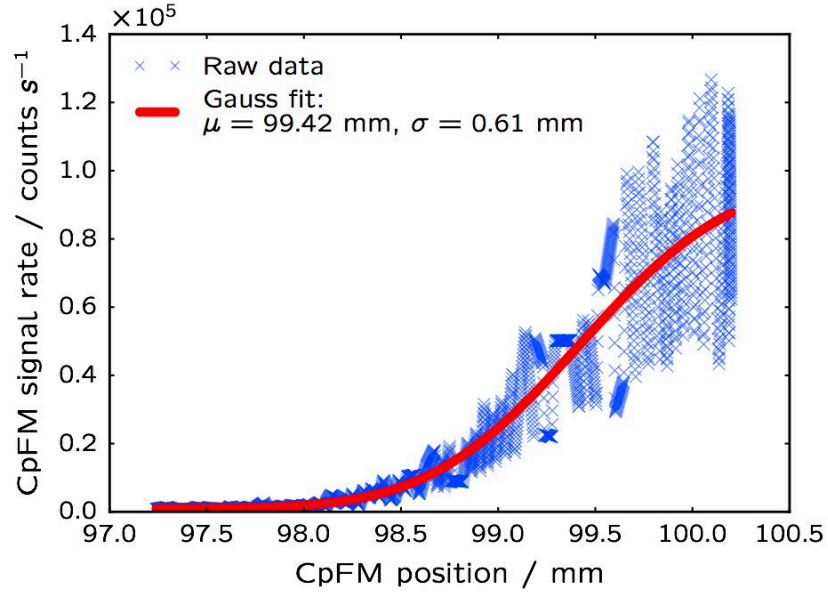
Figure 5.17 – CpFM count rate as a function of its position (blue dots). The red line shows the fit to a Gaussian function of the data [*Courtesy of F. Addesa and UA9 collaboration*].

5.7 Conclusions and outlook

Non-resonant crystal assisted extraction is a concept that was tested in the SPS in the 90s [29]. It was proven that high-energy particles can be deflected by means of silicon bent crystals. In the SPS today, the UA9 experiment is currently active with the main aim to asses the feasibility of using bent crystals as primary collimators for high energy machines; LHC and beyond.

In order to investigate the feasibility of a complete non-resonant crystal assisted operational slow extraction, the concept of non-local extraction has been simulated and tested. The UA9 crystals installed in LSS5 can be used to deliver beam to the LSS2 extraction channel.

In order to use the present hardware, an optimal optics for the non-local non-resonant crystal assisted slow extraction was found. The FT optics can be used to extract the channelled beamlet from the crystal at the second turn at the ZS.

Particle tracking simulations have been carried out to validate the concept. Also, dedicated machine time was allocated in the SPS to prove the experimental feasibility. The test was divided in two due the risk of damaging the ZS wires. During the first MD time, the channelled beam displacement was measured at the TCSM location in LSS5 and it was measured to be consistent with simulation predictions.

In the second MD, the complete extraction from the SPS aperture towards TT20 was

performed. Using the simulated scenario, the channelled particles at the crystal in LSS5 were extracted from LSS2 and measured at the CpFM detector in TT20.

This was an important step towards the realisation of an operational scenario that foresees crystals assisting slow extraction.

CHAPTER 6

SPS Slow Extraction Optimisation for future FT experiments

A new experiment, SHiP [6], has been proposed at CERN. The purpose of this experiment is to investigate the existence of three Heavy Neutral Leptons (HNL) postulated in the neutrino minimal Standard Model (νMSM) [7, 8] theory. High-intensity slow-extraction of 400 GeV protons from the SPS is a fundamental pre-requisite for SHiP. The experiment requires 2×10^{20} protons on target in five years, which equates to approximately twice the maximum flux ever slow-extracted per year at the SPS (the West Area Neutrino Facility in the 90s reached almost 2×10^{19} protons per year). A conceptual design study including the operational constraints of the SPS and its other users recommended a 7.2 s SHiP cycle with a short 1.2 s flat-top [36] with 4×10^{13} proton per pulse. Beam losses and activation of the electrostatic extraction septum (ZS) could be a serious performance limitation.

In this chapter, the present SPS slow extraction is described, and the most important parameters which have to be kept under control are highlighted. The evolution of the activation induced through the slow-extraction process is discussed and the expected situation for SHiP presented. Tracking simulations and measurements are compared to evaluate the quality of the simulation tools used to model the future scenario. In addition, combining together the results from the last chapters, a possibility to reduce slow extraction induced losses is developed. The proposal comprises the usage of non-local crystal assisted slow extraction together with the standard SPS resonant extraction. Tracking simulations are used to characterised the expected losses reduction in the extraction region.

6.1 Characterisation of SPS slow extraction

The slow resonant extraction is a process that permits the extraction of a quasi-constant flux of particles from a synchrotron over several thousands of turns. In the SPS, the
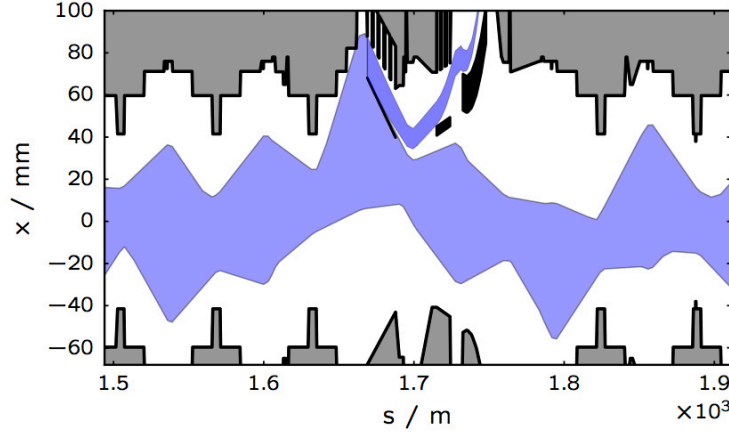
Figure 6.1 – Envelope of the circulating and extracted beam during the SPS slow extraction. In blue, the extrema of the trajectories of the last three turns for a particle with maximum amplitude at the ZS are superimposed. No tolerances have been included and a spiral step of (maximum) 20 mm at the ZS was assumed.

typical spill duration is 4.8 s, which corresponds to 2×10^6 turns. This is obtained using three septa (ZS, MST and MSE) and four extraction sextupoles with constant nominal integrated strength of $k_2 = -0.12\,\mathrm{m}^{-3}$. The horizontal chromaticity is trimmed to $\xi_x = -1$ and the momentum spread is increased to enhance the beam tune spread by means of an RF manipulation. Then the RF are switched off and the beam is let de-bunching, to help smoothing the extracted intensity over time.

The particle amplitude oscillations are then driven unstable by pushing the tune towards the resonant condition $3\nu_x = n$, where ν_x is the horizontal betatron tune and n is an integer. The quadrupole strength is changed, sweeping through the tune spread of the beam, during the length of the spill and the rate of the change is adjusted to guarantee as uniform as possible flux of the extracted beam [37]. The SPS nominal tunes for the FT beam are $\nu_x = 26.66$ and $\nu_y = 26.58$, for the horizontal and vertical plane respectively. As the horizontal tune is varied between $\nu_x(1 - \xi_x \delta_{p,\max})$ and $\nu_x(1 - \xi_x \delta_{p,\min})$, particles with different momenta are extracted as a function of time.

A closed orbit bump is introduced at the ZS in order to create a global aperture bottleneck to ensure that particles are extracted at the ZS and not lost elsewhere. Five bumpers are used to approach the circulating beam to the ZS. The maximum orbit excursion, $x_{CO} = 48\,\mathrm{mm}$, is reached at the focusing quadrupole just upstream of the ZS. Particles reaching the ZS upstream position with a sufficient oscillation amplitude to cross the septum wires and enter the electric field region are deflected into the extraction channel (Fig. 6.1). The additional deflection needed to enter the quadrupole coil window, which represents the beginning of TT20, is provided by the MST and MSE.

The slow extraction process involves the control of many machine parameters, such as the bump amplitude, tune sweep, chromaticity, momentum spread, etc. Each of these

contributes to the efficiency and quality of the extraction. In this section, some of the main SPS slow extraction parameters are evaluated and reference measurements and simulations are presented.

6.1.1 Enhancement of momentum spread

The SPS resonant slow extraction is momentum driven. To provide the required spill duration with an as uniform as possible spill intensity rate, a so-called *RF gymnastic* is performed, when the extraction energy of 400 GeV is reached. This is a manipulation that theoretically should uniformly distribute the particles momenta filling the whole RF bucket, and comprises the following steps (Fig. 6.2):

- The RF phase is moved (almost instantaneously if compared with the time scale of the RF gymnastic) to an unstable one, i.e. $\Delta\phi_s = \pi$, and kept constant for 0.3 ms (Fig. 6.2–1, 2);

- The phase is moved back to the nominal value for 2.25 ms (Fig. 6.2–3, 4, 5);

- All RF cavity voltages are set to zero (Fig. 6.2–6).

After the RF gymnastic, with the RF off, the beam de-bunches, which reduces any high frequency intensity modulation components in the spill (200 MHz, 40 kHz).

The knowledge of the beam momentum spread is fundamental for the optimisation of the extraction. For this test, a Schottky pick-up [38] was used to measure the beam momentum spread. Such a pick-up gives the revolution frequency distribution of the beam. The momentum spread is related to the frequency spread by:

$$\delta_p = \eta^{-1}\frac{\Delta f}{f_0}, \tag{6.1}$$

with δ_p being the momentum spread, η the slip-factor and $\Delta f/f_0$ the frequency spread. In Fig. 6.3 the measurements of the momentum spread distribution before (left - red solid line) and after (right - red solid line) the RF gymnastic are shown. A model of the SPS slow extraction and the RF gymnastic has been developed using MADX. In this model, no intensity dependent effects are taken into account. Using the measured momentum spread distribution as input, the resulting distribution after the RF gymnastic is shown in Fig. 6.3 as blue histograms. Measurements and simulations show a similar trend of the evolution of the momentum distribution. The discrepancy in the plot after RF gymnastic originates from the relatively long acquisition time of the network analyser used to measure the frequency range of interest.
In Fig. 6.4 the measured momentum spread distribution all along the flat top of the FT cycle is shown (while slowly extracting). It is interesting to notice that a significant part
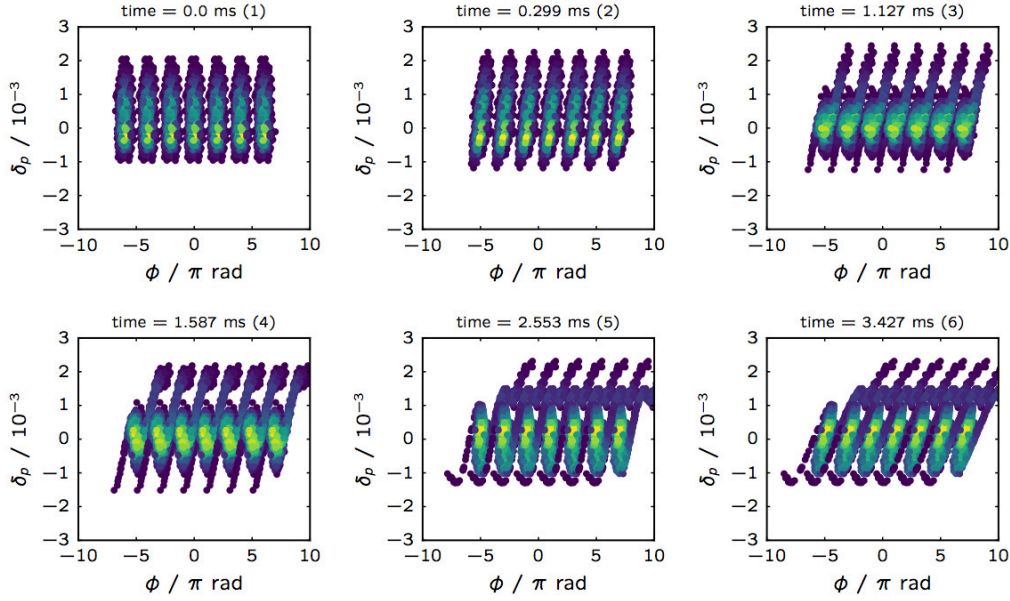
Figure 6.2 – Simulated longitudinal phase-space distribution during the SPS RF gymnastic.

of the negative δ_p distribution is left behind. This might be caused by the non-optimised choice of the starting point of the tune sweep when measurements were carried out.

6.1.2   Slow extraction tracking simulations

The developed MADX model has been tuned with measured machine parameters such as chromaticity, momentum spread, spiral step, etc. Thanks to the possibility of changing the horizontal tune (main machine quadrupole strengths) on a turn-by-turn basis in the simulation, the whole slow extraction process can be simulated. The results from the previous subsection are used to realistically distribute the particles in momentum at the beginning of the extraction process.

Tracking simulations of the whole slow extraction process were done to assess the quality of the model and hence to be able to compare it with measurements. An initial Gaussian distribution on the transverse plane and with the measured longitudinal distribution was tracked through the RF gymnastic process. The RF cavities have been switched off and the slow extraction started. The distribution obtained at the upstream end of the ZS (Fig. 6.5) was tracked through the septa towards TT20. The beam profile at the first monitor [1] in TT20 was obtained and compared with the measurements (Fig. 6.6). A very close agreement between measurements and simulations is shown. The main difference is

---

[1]Secondary emission monitor gird device composed of vertical and horizontal wires. It is used to measure the beam transverse distributions
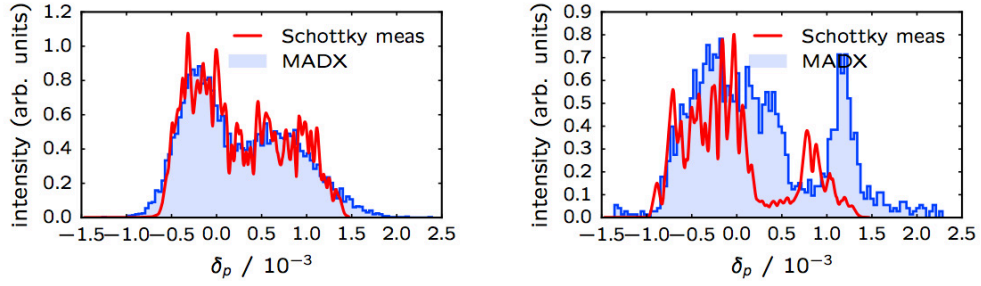
Figure 6.3 – Momentum distribution before (left) and after (right) the RF manipulation called RF gymnastic. The measurements results are drawn in red and MADX tracking results in blue.
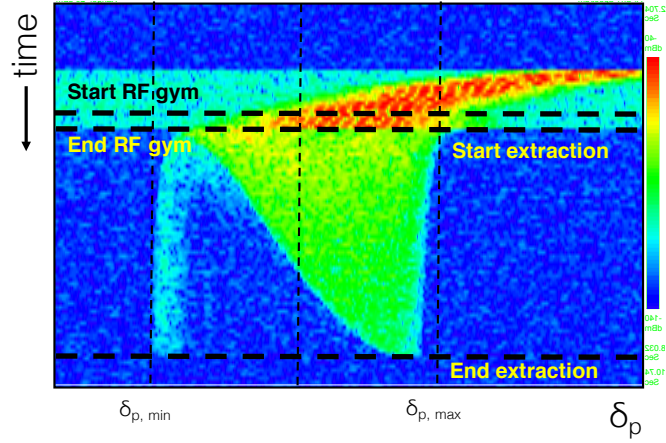
Figure 6.4 – Measurements of the momentum spread distribution during the slow extraction.

in the positive side of the horizontal profile. In simulations, the ZS has a sharp edge and no scattering of primary protons on the wires is considered. This is clearly not realistic. Such scattered particles are difficult to transport to the targets and will be lost in TT20. Due to their large angles and difference in energy, they can be outside the phase space acceptance of the line and hence lost before reaching the target.

SPS slow extraction stop band width

The extracted momentum offset as a function of time is shown in Fig. 6.7-left. If the tune is swept linearly, which is the assumption made in the simulations although this is not the case in operation, the slopes in Fig. 6.7(left and right) are the same. This assumption does not change the validity of the used model because this will mainly affect
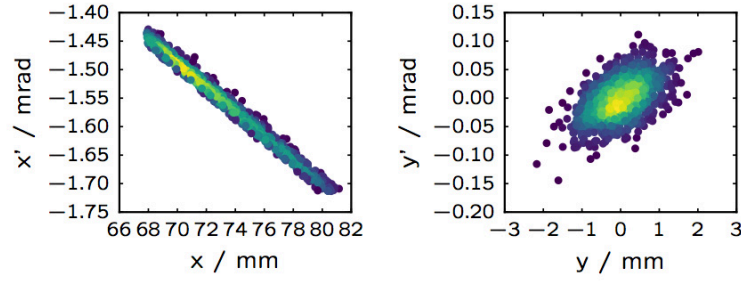
Figure 6.5 – Horizontal (left) and vertical (right) simulated transverse phase space at the entrance of the ZS at the end of the slow extraction. This has been obtained with a bump amplitude of 94 % the nominal, in order to reproduce the measured spiral step.
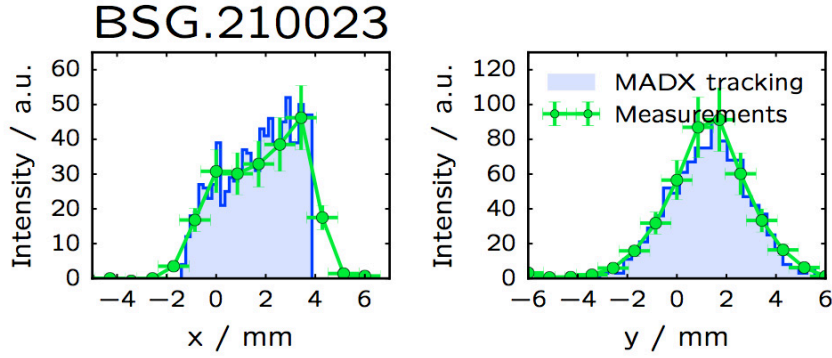
Figure 6.6 – Horizontal (left) and vertical (right) transverse beam profile at the BSG.210023 in TT20. Measurements obtained during 2016 commissioning are shown in green. The blue shaded area are the tracking simulation results.

the spill structure[2] (extracted intensity versus time) which is not considered here. The thickness of the particle distribution in time-momentum space of Fig. 6.7-left represents the stop band per unit of time. The initial transverse distributions have been cut at $\pm 3\sigma$, then the stop band width (SBW - Fig. 6.8) is calculated to be equal to 2.5×10^{-4}. For a fast rate of tune change with time, some of the particles will fall again in the stable area without leaving the SPS. This has been observed both experimentally and in simulations and it is the limiting factor to the maximum extraction speed for a certain set of slow extraction parameters. For nominal operational conditions in the SPS, the amount of beam left in the machine (which has to be dumped) is in the order of a few percent. This is directly proportional to the ratio of the sweep velocity, $v_{sweep} \equiv \delta_{\nu_x}/t_{spill}$, and

---

[2]The intensity of the extracted beam as a function of time depends on the momentum spread distribution and on the rate of the tune change.
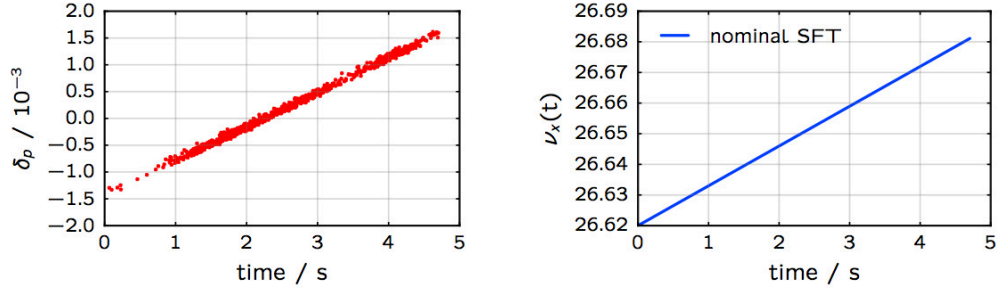
Figure 6.7 – Left - Simulated momentum spread of the extracted particles as a function of time. Right - Horizontal tune function used for the slow extraction simulations.

the extraction velocity, $v_{extr} \equiv SBW\xi_x/t_{1\sigma ext}$:

$$\frac{v_{sweep}}{v_{extr}} = \frac{\delta_{\nu_x}}{SBW\xi_x} \frac{t_{1\sigma ext}}{t_{spill}} \propto I_{dump}, \qquad (6.2)$$

where $t_{1\sigma ext}$ is the time needed for a particle on resonance with amplitude of $1\sigma_x$ to be extracted. It has to be noted that the terms of Eq. (6.2) are not all independent to each other, for instance, the SBW and $t_{1\sigma ext}$ are both linked to the normalised sextupole strengths. A careful adjustment of these parameters permits the reduction of the non-extracted beam intensity and a consequent improvement of the extraction efficiency. The enlargement of the SBW by increasing the beam emittance would be an obvious choice, although this can cause an increase of the extraction separatrix width, which would correspond to higher losses at the electrostatic septum. Instead, increasing the sextupole strengths will increase the SBW but leaving the separatrix thickness unchanged. The drawback, though, is the increase of the chromatic content of the separatrices which could result in an increase of the separatrix density. The increase of the separatrix density or the increase of the separatrix thickness translate in a higher number of primary protons seen by the ZS wires, and hence in higher losses.

Spiral step

The spiral step has been defined in chapter 3. Eq. (3.7) defines the transverse amplitude growth in three turns as a function of the normalised quadrupole strength and the wire distance from the beam centre. By varying the bump amplitude, the distance between the beam centre and the electrostatic septum is changed (quadratically). Hence, the spiral step can be changed by scaling the bump, as shown in Fig. 6.9. Reducing the bump amplitude increases the spiral step, as expected from (3.7). In Fig. 6.9 a very good agreement between measurements and simulations is shown, when using a bump amplitude 8 % bigger than ideally calculated. This is most likely due to the non-zero
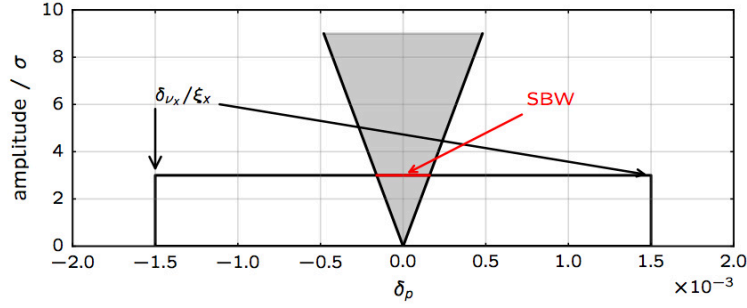
Figure 6.8 – Steinbach diagram of the SPS slow extraction. The stop band width (SBW) has been defined as the width of the stop band at a betatron amplitude of $3\,\sigma$

orbit in the extraction region or the mechanical precision of the ZS wires position. From the measurements, a closed orbit of about $3.5\,\mathrm{mm}$ with respect to the ZS is estimated to account for the difference with simulations.

In the last years, a non-negligible variation of the SPS closed orbit has been observed for the LHC beams [39] and it is believed that this is also the case for FT beams. The beam during slow extraction is debunched, hence the SPS orbit cannot be measured due to limitations of the electronics of the BPM readouts. A periodic measurement of the spiral step could give information regarding the actual distance between the beam centre and the ZS wires. This information can be used to understand if the observed losses during extraction are linked to variations in the CO since the beam density of the separatrix changes rapidly with the distance from the centre and higher losses may result.

6.1.3   Shorter spill duration

For the new proposed project SHiP a shorter spill duration, $1\,\mathrm{s}$, and the same intensity per extraction, $\approx 4 \times 10^{13}$ protons, are required. In order to evaluate the parameters needed to have a similar extraction dynamic as today, tracking simulations have been performed. The aim is to maintain the non-extracted particle intensity constant and keep the losses at the ZS as low as possible to not compromise the extraction efficiency and minimise the beam loss, equipment activation and personnel dose.

Due to the faster spill, the amount of non-extracted beam, if the slow extraction parameters are not changed, will be about five times higher than today's slow extraction. This has been observed in simulations and it is in agreement with expectations. Particles with tune on resonance do not spend enough time in the unstable region and are recaptured when their stable area is increased due to the change of the machine tune. More precisely, the non-extracted beam intensity I_{dump} ratio for the "SHiP 1" and "SPS FT" cases (Table 6.1) is exactly equal to the ratio of the spill duration, i.e. 4.8. In Fig. 6.10–1,2 such difference, for a momentum spread smaller than 1×10^{-3}, can be
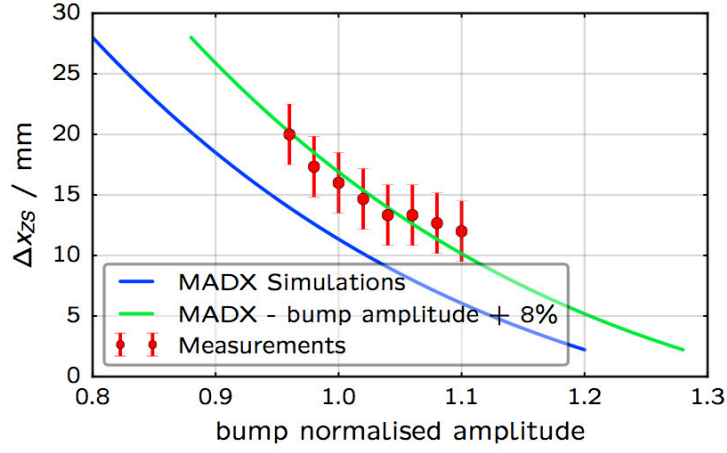
Figure 6.9 – Evolution of the spiral step as a function of the bump amplitude. In blue the spiral step is plotted in case of ideal machine. In red dots the measurements recorded during 2016 slow extraction commissioning are plotted. The case with a bump 8 % larger than theoretically estimated is shown in green.

observed. Here the instantaneous particle amplitude is plotted as a function of the momentum spread, as for the Steinbach diagram, the slow extraction with 4.8 s and 1 s spill duration.

From Eq. (6.2), the parameters that can be tuned to reduce the number of non-extracted particles can be identified. The tune spread can be reduced avoiding the RF gymnastic and reducing the horizontal linear chromaticity. As previously suggested, the sextupole strength can be increased to enlarge the SBW. Also, a more uniformly distributed momentum spread distribution can increase the slow extraction efficiency. In fact, using the set of parameters reported in Table 6.1–SHiP2 column, the amount of residual beam can be kept at the same level as for the present slow extraction (Fig. 6.10–3), even with 1 s spill duration.
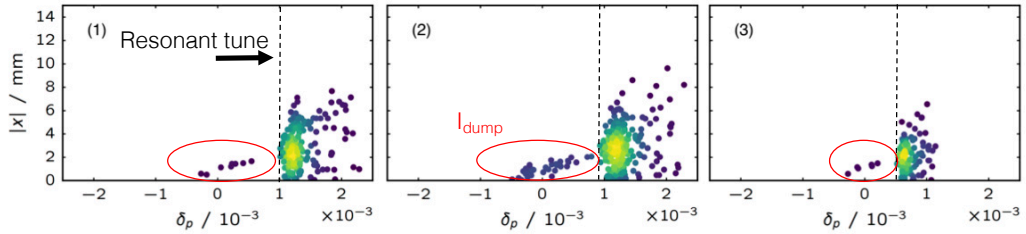
Figure 6.10 – Simulated Steinbach plot, at almost 70 % of the extraction process, for the three case of Table 6.1: 1) SPS FT, 2) SHiP 1 and 3) SHiP 2.

Table 6.1 – SPS slow extraction main parameters for three different scenarios: nominal SPS FT extraction, SPS FT extraction scaled to 1 s spill duration and ad-hoc settings for 1 s slow extraction.

Parameters	Units	SPS FT	SHiP1	SHiP2
Spill duration	s	4.8	1	1
H emittance	mm.mrad	12	12	12
V emittance	mm.mrad	7	7	7
H Chromaticity	-	-1	-1	-0.7
Spiral step	mm	13	13	18
Sextupoles k_2	m^{-3}	-0.12	-0.12	-0.24
Momentum spread	10^{-3}	± 1.5	± 1.5	± 1
Bump amplitude	%	95	95	100

6.2 Slow extraction losses

The resonant slow extraction is an intrinsically lossy process. The electrostatic septum physically cuts the beam when, due to the crossing of the third order resonance, it has been transversally blown up and diluted. In the SPS, the long straight section that hosts the slow extraction systems, LSS2, is the second worst activated area ($> 1 \times 10^3 \, \mu Sv/h$) of the whole SPS, only the dump system region is higher.

The SPS was originally built to host two slow extraction channels: LSS2 and LSS6. The main design aim for the SPS was for fixed target physics, although this has changed significantly during its operation as $p\bar{p}$ collider and then as LEP and LHC injector. The WA was served by the LSS6 extraction channel and the NA was, and still is, served by the LSS2 extraction channel. In order to deliver beam to both NA an WA via slow extraction process, a technique called *tune split* was used, where the phase-advance between the four extraction sextupoles and both electrostatic septa could be adjusted to a favourable value without affecting the machine tune. Then, using ad-hoc settings for the extraction sextupoles, particles could be slow extracted simultaneously from both LSS2 and LSS6 in the same cycle.

The highest protons on target (POT) per year ($\approx 2 \times 10^{19} \, p^+/year$) ever recorded in the SPS slow extraction history was at the WA when the half-integer resonant extraction was used (1995 - 1998). The extraction towards the WA was stopped when the CNGS operation started, 2007. In the CNGS era (2007-2012), the integrated protons slowly extracted from the SPS were much lower than previously achieved (Fig. 6.11). During LHC Run 2, due to the end of CNGS operation, the POT delivered to the NA are comparable with what achieved in 2007 and 2008, Fig. 6.11.

The SHiP experiment, which could potentially start operation after 2020, requires an unprecedented 2×10^{20} POT in 5 years. This means that a record 4×10^{19} POT/year will be required. This is a factor two above the WA record and a factor four above the highest POT/year recorded at the NA. The main challenge to satisfy these specifications

is the linear dependence of the activation of the area with the delivered POT (Fig. 6.12). The activation is expected to be a factor four higher than ever recorded in LSS2. Increased activation levels mean higher doses to personnel in the event of an intervention involving hands-on maintenance of the extraction hardware. In light of the increasingly strict radiation protection regulations, put in place for the safety of CERN's personnel, the cool-down time required before an intervention will become prohibitive for the operation of the NA. A way to mitigate the extraction losses has to be found if the availability of the machine has to be maintained during high intensity operation to the NA.

Different techniques have been developed in the last years to reduce losses at extraction, for instance the Multi Turn Extraction (MTE) [40] in the PS or mass-less septum, but none of them permit to have a spill of the order of seconds. Optimisation of the SPS third-integer extraction can clearly bring benefits to the extraction losses, although the optimisation alone cannot permit to reach the aimed loss reduction factor. A novel concept to significantly reduce the extraction losses has been explored, exploiting the concept of non-local extraction and the recent developments for crystals used in collimation.
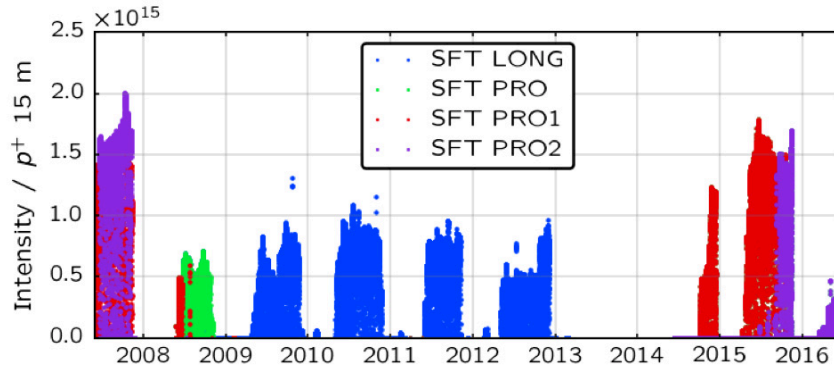
Figure 6.11 – Logged data of integrated proton intensity extracted over 15 minutes from slow extraction cycles.

6.3 Crystal assisted non-local resonant extraction via shadowing

In order to reduce the extraction losses coming from the direct impact of primary protons on the ZS wires, the bent crystal technology introduced in the previous chapter can be exploited. Silicon bent crystals, in principle, could be used to improve the SPS resonant slow extraction in two ways: either to replace completely the ZS or to shadow it. The first solution would offer many advantages with a much more compact device, although the current technology does not permit yet such usage of the bent crystals. The second option
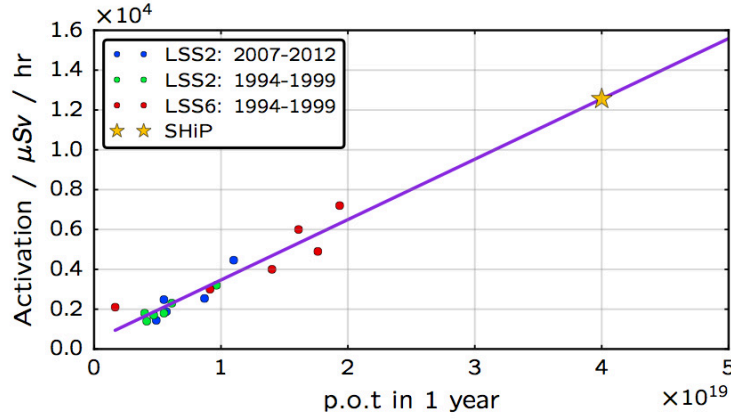
Figure 6.12 – Measurements of the activation at the end of the year in LSS2 or LSS6 as a function of delivered proton on target. The star represent the extrapolated scenario for SHiP if no modification to the slow extraction is put in place [*courtesy of M. Fraser*].

may be possible with available and tested technology. In the following, the performance reach and feasibility of crystal shadowing are explored.

For an operationally usable concept of crystal assisted slow extraction, a fast actuating crystal (a nominal SPS cycle is in the order of seconds), or a series of high energy magnetic bumpers to move the beam close to the crystal are needed. This is due to the large beam size of the circulating beam at injection energy, which requires more physical space at the crystal.

There are two ways to shadow the ZS wires: locally, by installing a crystal immediately upstream of the ZS or, non-locally, by installing it in a favourable optics location equipped with bumpers. The first option seems the easiest one operationally and the less demanding in terms of optimisation. The drawbacks are the possible integration issues in a high radiation area, small lever arm to the septum and hence larger minimum deflection angle and additional losses coming from un-channelled particles. The second possibility involves the exploitation of a concept previously discussed, non-local extraction. Here the negatives are increased operational complexity and possible losses elsewhere in the SPS. The advantages of having the crystal not in LSS2 are:

- decoupling of the bumps in LSS2 and in the crystal location, allowing more optimisation parameters;

- minimum deflection deflection angle;

- easy integration and modification for machine development studies.

In this section, a concept for the second configuration (non-local) will be described. The theoretical concept will be presented and the achievable loss reduction calculated.
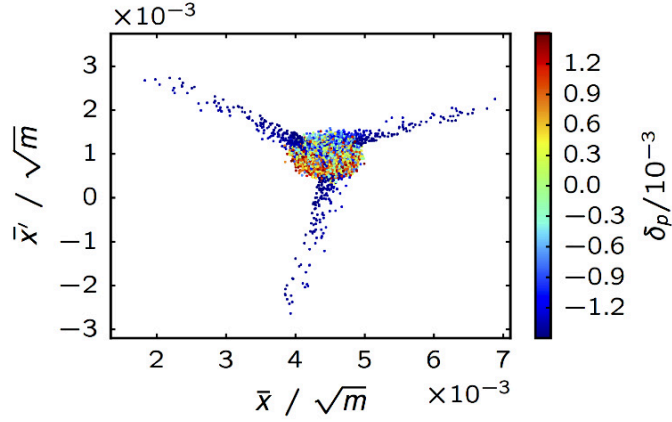
Figure 6.13 – Simulated normalised horizontal phase-space at the ZS 100 turns after the beginning of the spill.

Non-local extraction was introduced in chapter 4. Using the results from simulations and measurements, this concept can be extended to simple diffusion extraction (as already shown) or to a more complex resonant extraction. The basic idea of non-local extraction is to spread the extraction elements needed to extract a beam from a synchrotron around the whole machine, exploiting the available symmetries. This gives more flexibility in the creation of new extraction channels, e.g. reduces the space needed in one single straight section and permits to combine single extraction systems as blocks. The use of such a concept can be used to reduce the losses at the electrostatic septum during slow extraction using a thin bent crystal to shadow the ZS wires.

A first investigation for a suitable location for the crystal was made. The crystal should be installed at $n180° \pm \Delta\mu_{nl}$ from the ZS, with n integer. Here, $\Delta\mu_{nl}$ represents the phase-advance needed to completely move the beamlet intercepted by the crystal away from the ZS wires, for a given crystal deflection angle. Such an angle should be minimised in order to not reduce too much the acceptance of the extracted beam. Another requirement for the crystal location in the SPS is the presence of extraction bumpers, as previously discussed. The location should ideally have the same optics functions as the front face of the ZS, although this condition is not strictly necessary and can be compensated with the crystal thickness or with a dynamic bump. Taking all this into account, the best location identified in the SPS is in LSS4, just upstream the extraction septum MSE, $s = 4031\,\mathrm{m}$. To not interfere with the extraction elements and hence to avoid the creation of unwanted aperture bottlenecks, the proposal is to place the crystal on the inside of the SPS (the fast extraction septa are one-sided elements placed on the outside) and profiting from the dual polarity of the extraction bumpers. This translates in the necessity to force n to be an odd integer number in order to have the same separatrix intercepting both the crystal and the ZS at the same turn. In this way, the particles intercepted by the crystals are those
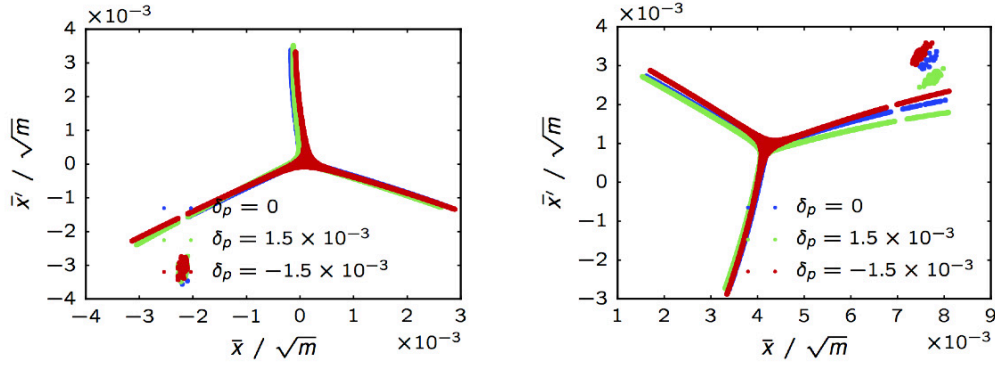
Figure 6.14 – Simulations of the expected phase-space at the crystal (left) and ZS (right) for a non-local resonant crystal assisted slow extraction. In this case a IBC has been simulated.

that, in the same turn, will be intercepted by the ZS wires. The effective thickness of the ZS wires considered here is $300\,\mu m$, where possible misalignment and motor movement accuracy are taken into account (to be compared with the $60\,\mu m$ thickness of a single wire). For the case of IBC (Ideal Bent crystal approximation), the losses at the ZS can be reduced to virtually zero. This is possible using a crystal $1.8\,mm$ thick. The thickness is defined by the total momentum spread of the beam, here assumed as $\delta_p = \pm 1.5 \times 10^{-3}$, and on the dispersion, and its derivative, at the ZS location (Fig. 6.15).

Due to the highly non-linear regime of the beam dynamics during the slow extraction process, particle tracking simulations are needed to assess the performance reach of this concept. In order to simulate the effect of the crystal on the beam, MADX and *pycollimate* were used. For this propose, a simple module to simulate the IBC and nIBC case was written. The SPS model used is the one discussed at the beginning of this chapter.

In order to have a complete picture of the expected performance of this technique, the whole slow extraction needs to be simulated. The SPS slow extraction is momentum spread based and is such that the stop band width is very narrow around the resonant tune (Fig. 6.8). Thanks to this characteristic, the problem can be decomposed in time, slicing the beam according to the particle momentum spread. This is a good approximation, in fact, as shown in Fig. 6.13, the separatrices at a certain instant are almost monochromatic. Each beam slice is composed by 1000 particles and they are tracked for 300 turns when exactly on resonance ($3\nu_x = 80$).

In Fig. 6.14 the results of tracking simulations for the IBC case are shown. Here, the normalised phase-space at the crystal and at the ZS are plotted. Note that the Hardt condition is not matched at the ZS. The zoom of the kicked beam in trace-space at the
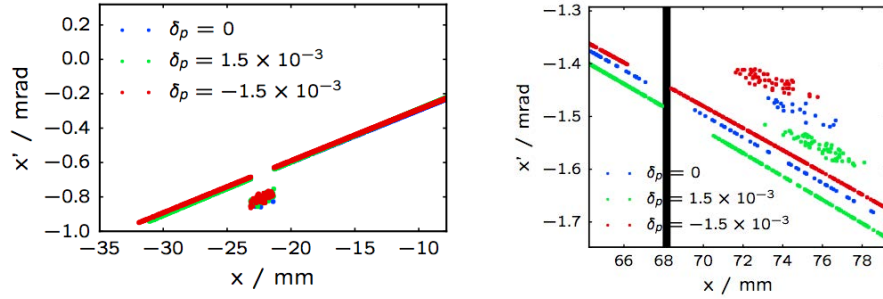
Figure 6.15 – Trace-space of the case described in Fig. 6.14 at the crystal (left) and ZS (right), for IBC approximation. The thick black line represents the ZS wires effective thickness.

crystal and ZS location are instead shown in Fig. 6.15. The requirement for such a thick crystal (relative to the ZS septum thickness) becomes very clear in Fig. 6.15. The ZS effective width has to be accommodated accounting for the total chromatic content of the beam and hence this gives the 1.8 mm crystal width specified.

In Fig. 6.16 and 6.17, the results of the tracking simulations for the nIBC case are shown. In order to evaluate the losses reduction at the ZS when shadowed by a crystal, more δ_p slices(13 instead of the 3 used for the ideal case) are used and the particle density of the extraction separatrix is plotted as a function of the horizontal transverse coordinate (Fig. 6.18). A clear intensity depletion section can be noticed at the ZS location and a consequent increase of extracted particles with spiral step smaller than 10 mm. The observed reduction is almost a factor of four (Fig. 6.19) even if the crystal efficiency has been assumed 54 %. A naive assumption can be that the loss reduction should be the same as the crystal efficiency. This is true only if the non-channelled particles would cross the crystal completely unperturbed. Instead, all the particles that can possibly hit the ZS wires are previously intercepted by the crystal which, with high probability, scatter them to a sufficient amplitude to miss the ZS wires. Only particles that receive an unlucky kick will still contribute to the losses at the ZS. In fact, the factor four reduction in losses can be seen as the sum of two effects: a factor two coming from the $\approx 50\%$ crystal efficiency (channelling), and a factor two coming from the simple scattering due to the crystal-beam interaction (transition and de-channelling).

The non-satisfied Hardt condition at the ZS (Fig. 6.14) translates into the need for such a thick crystal to compensate the dispersion functions and the large momentum spread. Due to the SPS optics and the slow extraction parameters, the horizontal chromaticity needed to satisfy the Hardt condition is a factor of two higher than currently used in the SPS. This translates into a much stronger dependence of the phase-advance between crystal and septum to the individual momentum of the particles, making the usage of the non-local extraction concept much harder, if not impossible. Also, the modification of the chromaticity changes the orientation of the separatrices at the crystal making the

91

alignment of the crystal with the ZS very complicated.

To reduce the thickness of the crystal, in order to reduce its activation, some expedients could be put in place:

- deploy a dynamic extraction bump which can be varied together with the horizontal tune to compensate the dispersion, and its derivative, at the ZS;

- reduce the momentum spread;

- improve the ZS position accuracy and precision.

The crystal thickness specified could comport an increase of the overall losses. This is not the case due to the low probability for a proton interacting with a crystal to perform inelastic scattering and hence originate losses. From [41], the probability of inelastic scattering at 400 GeV for about 2 mm long crystal is about 0.5 %. Hence, the expected losses at the crystal location would be about than 0.1 %. This is more than a factor of ten lower than the current situation in LSS2, hence a proper shielding should be sufficient to limit the air activation.

From the data in [32], a negative correlation between efficiency and crystal deflection angle can be retrieved, hence the minimisation of the crystal kick will be beneficial for the loss reduction. For the specified s-location, the minimum angle which guarantees the quoted loss reduction is 136 µrad. This could be further reduced by displacing the crystal to a different longitudinal position.

Summing up, the crystal parameters needed to shadow the ZS wires, basing the estimation on the presented simulations and on the single-pass data available at [32], have been summarised in Table 6.2.

Table 6.2 – Crystal parameters specification for the non-local resonant crystal assisted slow extraction.

Parameters	Units	Value	Comments
Efficiency	%	>65	-
Thickness	mm	1.8	For a $\delta_p = \pm 1.5 \times 10^{-3}$
Longitudinal position	m	4031	From the SPS starting point
Deflection	μrad	>136	For the above specified position
Distance from beam centre	mm	21.2	-

6.4 Conclusions and Outlook

Slow extraction is a process that demands the control and optimisation of many machine parameters. Each of them contributes to the quality and efficiency of the process. In this chapter, the main machine parameters from which a complete picture of the overall
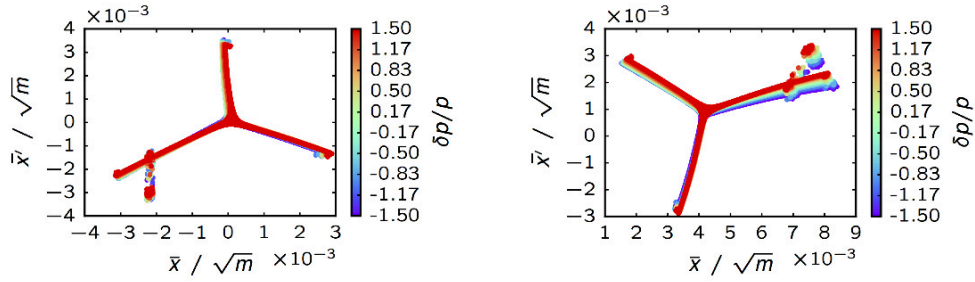
Figure 6.16 – Simulations of the expected phase-space at the crystal (left) and ZS (right) for a non-local resonant crystal assisted slow extraction. This refers to a nIBC case.
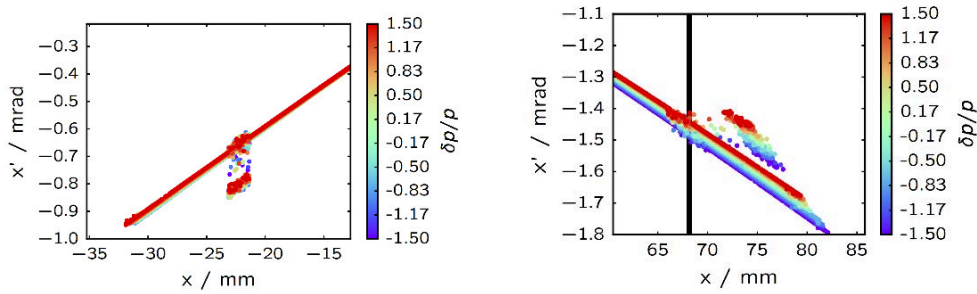
Figure 6.17 – Trace-space of the case described in Fig. 6.16 at the crystal (left) and ZS (right). The thick black line represents the ZS wires effective thickness.

performances can be derived have been investigated. As a consequence, a detailed model of the SPS slow extraction has been built. An overall very good agreement between measurements and simulations was shown and new slow extraction parameters configuration for a shorter spill duration given.

It was reported that the air activation of the area surrounding the electrostatic septum shows a very clear positive correlation with the POT delivered to the NA per year. For the much higher yearly POT required (about four times) by new experiments, the subsequent higher activation expected needs to be addressed. Exploiting the last decades results on silicon bent crystal technology to deflect part of the beam, an SPS new slow extraction technique has been developed. The shadowing of the ZS wires with a bent crystal should permit a loss reduction of about a factor four at the ZS, according to the simulation results shown. Also, due to the low probability of inelastic scattering for protons hitting the crystal, the overall loss reduction is estimated to be a factor four comparing with today's slow extraction. Such a reduction is in the range of what is needed for the foreseen SHiP operations. The specified crystal may be installed at the desired location in the upcoming years to evaluate experimentally the loss reduction at the ZS and to corroborate the simulation results.
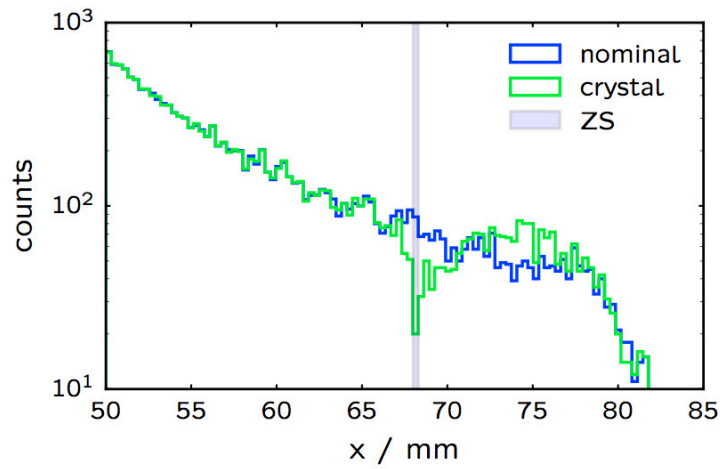
Figure 6.18 – Histogram of the horizontal particle position at the ZS. In blue is shown the case for a nominal SPS FT extraction and in green the case for the non-local resonant crystal assisted (nIBC) slow extraction.

The merging of crystal collimation (extraction) with usual extraction techniques could be extended to simplify, or just make possible, slow extraction from much higher energy machines.
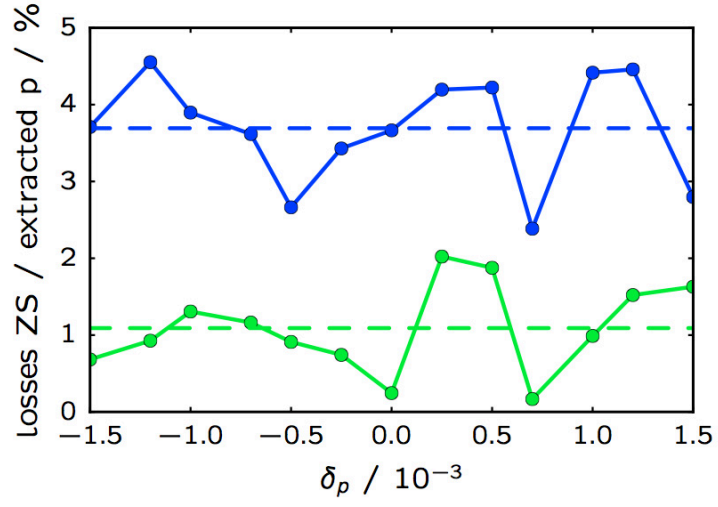
Figure 6.19 – Particles intercepting the ZS wires (assumed $300\,\mu\text{m}$ effective thickness) as a function of the δ_p extracted (time). In blue is shown the case for a nominal SPS FT extraction and in green the case for the non-local resonant crystal assisted (nIBC) slow extraction. The dashed lines are the averages.

CHAPTER 7

Injection and transport system for the the HL-LHC era

The increase of the intensity and brightness of the SPS beams will represent an operational challange also for the transport and injection into the LHC. Hence, the consequences of the failures of the systems involved in these processes have to be carefully evaluated. The increase of about one order of magnitude of the LHC luminosity determines a factor of two higher stored energy ($E_{stored} = pceN_p$) of the injected beam into the LHC (Table 7.1). This translates in the necessity to upgrade the SPS-to-LHC collimation and the LHC injection protection systems. The upgrade has to take into account the protection of the machine components, as well as the survival of the protection elements themselves. The reduced beam transverse size and the increased charge demands better suitable materials for the passive protection elements. In this chapter, some of the improvements of these systems will be discussed and the guaranteed protection evaluated.

Table 7.1 – Main beam parameters of the present LHC and future HL-LHC operation.

Beam type	Norm. emittance (π mm mrad)	Bunch intensity N_p (1×10^{11} p)	Bunches
LHC (Ultimate)	3.5	1.7	288 (4×72)
LHC (BCMS)	1.4	1.2	288 (6×48)
HL-LHC (Nominal)	2.0	2.3	288 (4×72)
HL-LHC (BCMS)	1.4 (min)	2.3	288 (6×48)

7.1 Aperture definition for LHC and HL-LHC

.

The design of the HL-LHC carries with it a major modification of the standard parameters and tolerances used to define the LHC apertures. The n_1 model [42, 43, 16] is the standard way to quantify the LHC aperture. Form the LHC Design Report [16]: "The effective

mechanical aperture n_1 defines the maximum primary collimator (TCP) opening in terms of the rms beam size that still guarantees a protection of the machine aperture against losses from the secondary beam halo. It depends on the magnet aperture and geometry and the local optics perturbations". Starting from the assumptions that the secondary halo (protons scattered by the primary collimators) [16] can induce a quench of the super-conducting magnets and that such a halo has a transverse extension as shown in Fig. 7.1 [16], the n_1 calculation corresponds to the maximum primary collimator aperture needed to protect a specific local aperture. In this way, the n_1 that is calculated (assuming tolerances on CO, optics, alignment, dispersion) for each machine element can be compared with the minimum required aperture of the primary collimators, $n_1 = 7.0$ (where operational margins have been included, in fact the actual $n_1^{min} = 5.5$) [16]. This value became the criterion to evaluate the aperture of any LHC component.

In the first two runs of the LHC, i.e. Run 1 (2010-2013) and beginning of Run 2
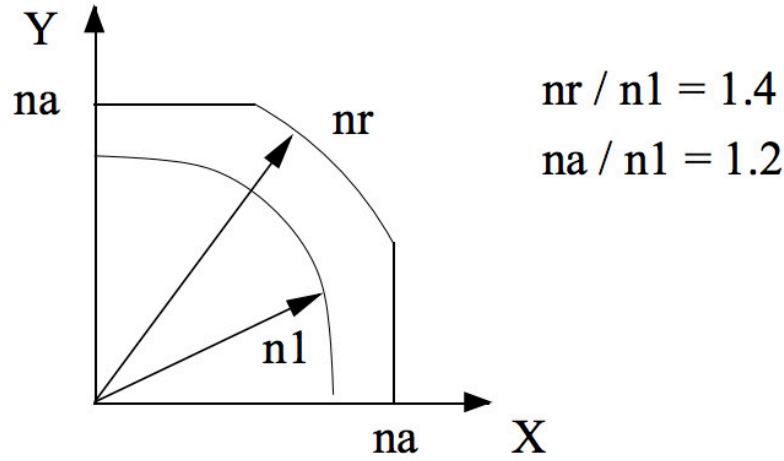
Figure 7.1 – Primary beam and halo shape assumed in the calculation of the n_1[16]

(2015-2016), the available LHC aperture was measured several times and under different conditions [44, 45, 46, 47, 48, 49, 50]. These results show a very good agreement with what was predicted during the LHC design phase. Profiting from the accumulated experience the parameters (tolerances and quench limits) used to calculate n_1 were reviewed, in order to obtain a more realistic model for the design of the aperture of the HL-LHC.

The tolerances used in the aperture calculations and the criterion used to evaluate the allowed mechanical aperture have been reviewed. The mechanical tolerances, assumed for every machine elements, come from the actual design of such elements, hence these values are provided by the hardware designer and were not changed. Instead, the tolerances coming from beam dynamics considerations can be adapted to match the cited measurements results (the details of the new approved tolerances are in [51, 52]). One of the main differences with respect to the original n_1 method is the way the halo shape is

calculated. The halo shape was obtained using the radial extension of the primary halo and the horizontal, vertical and radial extension of the secondary halo assumed with a racetrack shape [51]. Moreover, the calculation assumed that the secondary collimators are perfect absorbers. Both simulations and measurements [18, 53, 54, 55, 56] have shown that the dispersion suppressors downstream of the collimation system in IR3 and IR7 are the limiting locations for losses, although the n_1 shows significant margin. As proposed in [51], the losses recorded in the dispersion suppressor following IR7 are due to single-diffractive events taking place in the primary collimators. Such events produce particles significantly off-momentum that manage to escape the collimators placed in the straight section, where the dispersion is very low, and get caught by the normal apertures where the dispersion increases (dispersion suppressor) [51]. The reason of the inconsistency between observations (and also simulations) and n_1 calculations is because the n_1 halo model does not take into account off-momentum halo.

Moreover, the n_1 does not take into account particular failures originated by fast acting magnets (injection and extraction kickers), which can lead to more critical scenarios than halo cleaning. The idea proposed in [51] is to express the minimum allowed aperture directly in number of beam σ (this is done using the existing MAD-X aperture routine and setting the halo parameters to $6\,\sigma$, Table 7.2) and to deduce a criterion to account for losses from regular collimator cleaning, asynchronous beam dumps and injection failures. In this chapter, the convention

$$\sigma \equiv \sqrt{\beta_u(s)\ \epsilon_N/(\beta\gamma)}, \tag{7.1}$$

is adopted, where $\epsilon_N = 3.5\ \pi.\mathrm{mm.mrad}$ is the normalised transverse emittance. Such a notation is used only here unless explicitly specified.

The establishment of a criterion that includes, among the others, asynchronous beam dumps and injection failures is done calculating the intensity as a function of the transverse amplitude using the *survival function* on the escaping beam, obtained from particle tracking simulations. If the surviving particles, after one of the two failures, are distributed as $f(y)$ (PDF), the survival function normalised to the beam intensity, N_p, is given by:

$$S(y) \equiv N_p \int_A^\infty f(\hat{y}) d\hat{y}. \tag{7.2}$$

The function $S(y)$ expresses intensity as a function of transverse amplitude. Under the implicit conservative assumption that in case of losses the whole beam will be lost in one single location, $S(y)$ can be used to determine the criterion for the aperture calculation. Using then the set-up beam flag to limit the maximum accepted value of $S(y)$, a minimum protected amplitude y is obtained. The maximum beam intensity allowed in the LHC at injection energy when the protection systems are not in place is the so-called *set-up beam flag* ($\equiv 5 \times 10^{11}$). This value corresponds to about a quarter of the damage limit of copper experimentally obtained in [57] (which is $2.3\,\mathrm{p} \times 10 \times 10^{12}\,\mathrm{p}$ at $450\,\mathrm{GeV}$). The

value used to evaluate the maximum allowed amplitude is chosen as $N_{MAA} \equiv 5 \times 10^{11}$ p. Such calculations are done for the three cases previously mentioned, and the maximum among them is used as criterion for the aperture evaluation. In this chapter, the details of the simulations done for the injection failure scenarios are described.

Table 7.2 – New proposed parameters (3rd column) for the aperture studies at injection compared with the parameters used during the LHC design phase (2nd column) [51].

Parameter set	LHC design	HL-LHC design
Primary halo extension	$6\,\sigma$	$6\,\sigma$
Secondary halo, hor./ver.	$7.3\,\sigma$	$6\,\sigma$
Secondary halo, radial	$8.3\,\sigma$	$6\,\sigma$
Normalised emittance ϵ_N	$3.75\,\mu$m	$2.5\,\mu$m
Radial closed orbit excursion $x_{\rm co}$	4 mm	4 mm
Momentum offset δ_p	1.5×10^{-3}	6×10^{-4}
β-beating fractional beam size change k_β	1.1	1.05
Relative parasitic dispersion $f_{\rm arc}$	0.27	0.14

7.2 Beam transfer protection

The complexity of the elements participating in the extraction and injection process (kickers, bumpers, septa) and their particular principle of operation make them very sensitive elements in terms of machine protection. They are not the only elements that can lead to uncontrolled beam losses, in case of failures, also all the magnets involved in the beam transport can fail and mean arm to the nearby accelerator components.

The classification of failures of the different elements is done according to their individual time constants and their operational strength (essentially, how fast the beam can be moved from the reference trajectory and become dangerous for the downstream elements). For the SPS-to-LHC TL, such a classification is done, as shown in [57], evaluating the time needed to move the beam by $10\,\sigma$ (τ_{10}):

- slow failure: $\tau_{10} > 10\,$ms;

- fast failure: $0.1\,$ms $< \tau_{10} < 10\,$ms;

- ultra-fast failure: $\tau_{10} < 0.1\,$ms.

The dipoles of the TLs have usually long time constants and hence they belong to the *slow* or *fast* failures, depending on the magnet type and strength.

For elements that belong to the slow failure category, active protection systems (simple

current surveillance, beam interlocking system, etc.) are usually sufficient to guarantee adequate protection.

The SPS extraction septa MSE have a relatively short time constant, $\tau_{10} = 0.25\,\text{ms}$, and sits at the edge of the *fast* failures. The injection septa MSI, instead, has a longer time constant but belongs to the *fast* failures category too. For these elements, the conventional power converter surveillance (PCS) [57] is not sufficient and specific current monitors (e.g. FMCM) and passive protection elements (intercepting devices) need to be used to protect the TL and the LHC from misteered beam.

Kickers, both extraction and injection, are pulsed elements for a time which is comparable to the SPS revolution period, i.e. $T_{SPS} \approx 23\,\mu\text{s}$. They can deflect a $450\,\text{GeV}$ beam by hundreds of µrad and the time needed to reach the full field is of the order of µs. These characteristics make them belong to the *ultra-fast* failures category. In this case, none of the active protection system is enough and passive devices are the only way to protect the elements of the TL and LHC.

7.2.1 Active protection

The active protection systems used in the SPS-to-LHC transfer comprises the monitoring of hardware and beam parameters [57]. For instance, the current of the main magnets are constantly monitored (PCS). Also, BPMs at the SPS extraction are part of the interlocking system. If the beam position at these monitors is not inside predefined tolerances, the beam extraction is not permitted.

In the specific case of the SPS-to-LHC transfer, all the power converters of the magnets involved in the transfer process are surveyed. Due to the small time constant of some of the strongest magnets, the simple PCS system is not sufficient. In fact, these elements are interlocked with two protection systems: the Fast Extraction Interlock (FEI) and the Fast Magnet Current change Monitors (FMCM). The FEI controls the current value before giving the true flag for extraction. This check is done at latest $4\,\text{ms}$ before extraction. The usual tolerance of the surveyed value is around $0.1\,\%$ the nominal current. The FMCM measures the voltage across the magnet in order to detect rapid current changes. The usual interlock threshold is around few 1×10^{-4}.

Whatever happens in the last $4\,\text{ms}$ cannot be stopped by any of the active protection system and hence the need of a collimation system for the TLs.

7.2.2 Passive protection

A passive protection system represents the last resource against any type of failure that can result in a sudden and localised beam loss. It is usually composed by blocks of material (high or low Z, or even combination of them) strategically placed to protect sensitive accelerator components or to create voluntary aperture bottlenecks. They can

be divided in two families:

- Generic systems that protect the machine apertures against any failures;

- Dedicated system for certain critical regions (like injection and extraction).

The SPS-to-LHC TL collimation system belongs to the first category. It is composed by 6 collimators per TL. This will be described more in detail in the following section.

In the second category, instead, there is the LHC injection protection system. These systems are composed by fewer devices because they target only few critical elements (mainly kickers). The typical strategy is to place a main absorber 90° phase advance from a kicker. Auxiliary absorbers could be also used, depending of the expected failures.

7.3 SPS-to-LHC TL protection system for the HL-LHC era

Following the arguments of the last section, the SPS-to-LHC TL are equipped with a series of active and passive protection systems.

The passive protection system of the TLs is composed by three collimators (TCDI, Target Collimator Dump Injection) per plane per TL and guarantees the protection of the tight LHC aperture, as well as of the injection septum MSI. Its aim is to intercept miss-steered beam coming from the SPS and, in case of direct impact, to attenuate it to a safe level for the machine components. The design strategy of the present TCDI was to have an attenuation of a factor twenty. This was the case because the LHC Ultimate beam intensity (Table. 7.1) is about a factor of twenty above the safe intensity at $450\,\mathrm{GeV}$.

These $1.2\,\mathrm{m}$ long devices are made of graphite R4550 with $1.83\,\mathrm{g/cm^3}$ density. They are placed as close as possible to the LHC injection points in order to cover as many as possible sources of failures. Each collimator is placed at 60° phase advance from another, to guarantee a full phase space coverage (Fig. 7.2). The maximum amplitude A_{MAX} permitted with such a configuration is given by:

$$A_{MAX} \equiv \max(A_{x,y}) = n_{tot}/\cos(\Delta\phi/2), \tag{7.3}$$

where $\Delta\phi$ is the phase advance between two consecutive collimators and $n_{tot} = n_{setting} + e_{TCDI}$ is the half collimator gap in nominal beam sigma ($n_{setting}$) plus the error expected on each jaw (e_{TCDI}). Using the values from Table 7.3 [57], the maximum amplitude that can escape the TL collimation system is $7.4\,\sigma$ for $n_{setting} =5\,\sigma$.
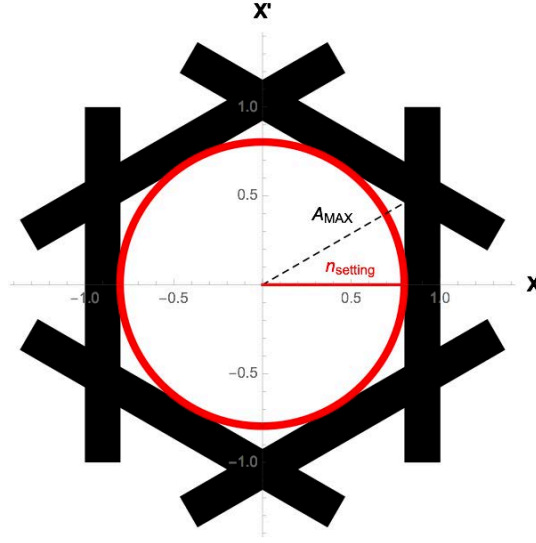
Figure 7.2 – Schematic view of the TCDI position in normalised phase space as seen at the last collimator in either of the two transfer lines.

Table 7.3 – Tolerances of the transfer line collimators [57]. For a typical beam size of $0.5\,\mathrm{mm}$, the linear sum of them gives $1.4\,\sigma$.

Parameter	Units	Value
Jaw parallelism	µm	50
Jaw axis respect to tank	µm	100
Tank axis respect to the beam	µm	180
Flatness	µm	50
Beam position	µm	44
Beam size + β-beating	σ	0.5

For the HL-LHC era, the increase in beam brightness poses more demanding requirements on the transfer line collimators. The intensity increase together with the emittance reduction make the present TCDI design incompatible with post-LS2 operations. The most challenging beam that the TCDI should protect the LHC and transfer lines from is the HL-LHC BCMS (Table 7.1). In fact, to reduce such a beam intensity to a safe value, a factor seventy attenuation is required. Comparing this with the LHC ultimate intensity, which was the design target for the present TCDI, the relation that has to be satisfied is [4]:

$$\frac{I_{afterTCDI}}{\epsilon_{afterTCDI}} = \frac{1}{20}\frac{I_{LHCultimate}}{\epsilon_{LHCultimate}} = \frac{1}{70}\frac{I_{HLLHC-BCMS}}{\epsilon_{HLLHC-BCMS}}. \tag{7.4}$$

The required attenuation can be achieved with: $1.9\,\mathrm{m}$ of graphite R4550 or with $2.1\,\mathrm{m}$ of

3D C/C. To date, there is not final decision on the material that will be used because experimental evaluation of the robustness of the two materials with similar HL-LHC beam parameters is still ongoing. The length was fixed to be 2.1 m, independently on the final material choice, to advance in the final design.

The increased beam brightness posses problems on the survival of the devices themselves for certain impact parameters. The stress caused on the material, for instance, for a $1\,\sigma$ impact parameter is above the material strength. This is closely related to the beam size and hence studies were done to adapt the optics to satisfy $\beta_x \times \beta_y > 3600\,\mathrm{m}^2$ [4]. For TI2, the current TCDI locations already fulfil all these constraints and hence no modification was needed. For TI8 instead, optics and TCDI positions were changed to satisfy the specifications.

The new design of the TCDI for the HL-LHC era implies new tolerances, as reported in Table. 7.4. With the new tolerances, the maximum amplitude that can escape the TL collimation system is $7.5\,\sigma$ for $n_{setting} = 5\,\sigma$.

Table 7.4 – Tolerances of the new transfer line collimators [4]. For a typical beam size of 0.5 mm, the linear sum of them gives $1.5\,\sigma$.

Parameter	Units	Value
Max mechanical offset	µm	330
Flatness	µm	100
Jaw centring	σ	0.07
Beam position	µm	44
Beam size + β-beating	σ	0.5

7.3.1 Collimator centring and set-up validation

The TL collimators need to be aligned with respect to the actual non-zero horizontal and vertical trajectory of the transfer lines. The centring procedure consists in finding the jaw position that minimises the beam losses once the half gap has been set at $5\,\sigma$. This is done using an operational tool so called `collimator scan app` (Fig. 7.3).

The application uses the BLMs close to the selected collimator and performs an automatic scan. The gap is kept fixed and both jaws are moved across the beam in a number of predefined steps and with a chosen step-size. Once the scan is finished, the obtained result is BLM readings as a function of the collimator jaws centre. Then, a second order polynomial fit of the data is performed and the minimum of this function represents the the beam position at that location. The number obtained (by default in betatron sigma but it can be automatically translated in millimeters) can be directly sent to the machine hardware. Such procedure must be repeated for all the TL collimators.
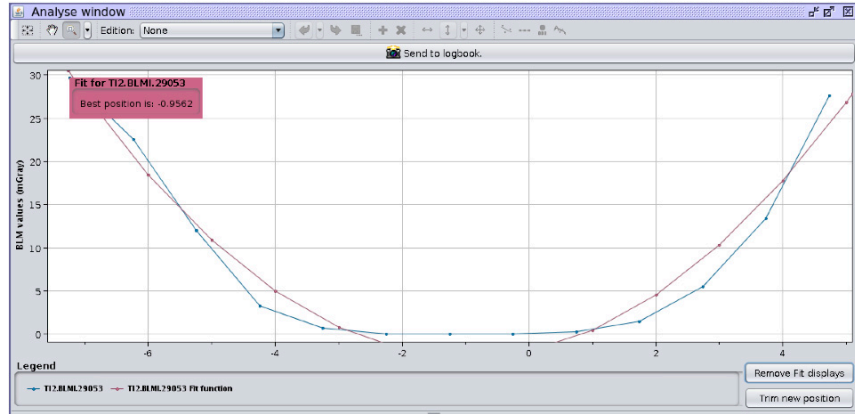
Figure 7.3 – Screen-shot of the operational tool used for the TCDI automatic alignment.
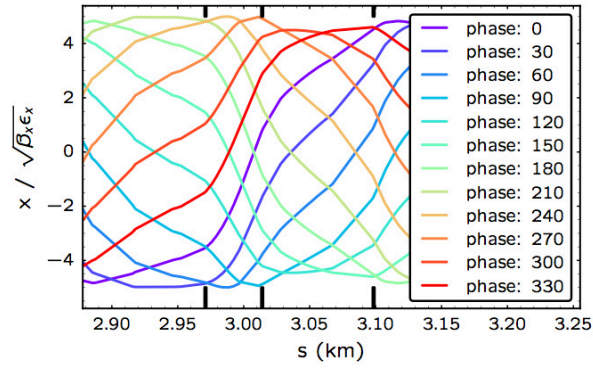
Figure 7.4 – Example of normalised trajectories used for the TCDI validation procedure (TI2 horizontal). The horizontal collimator longitudinal positions are sketched in black.

In order to validate the TCDI set-up (centring and gaps), a series of TL controlled oscillations is used. An example of trajectories is shown in Fig. 7.4. Such oscillations have to probe the whole phase-space. This is done by means of a series of correctors in the TLs to originate an oscillation that has the aimed transverse coordinate pairs (x, x') at the end of the TLs, as shown in Fig. 7.5. Using the losses recorded at the BLM (calibrating them first to resolve the number of lost protons) placed in proximity of the collimators, it is possible to reconstruct the gap opening of the TCDIs. With this information, the phase-space coverage guaranteed by the TL collimation system can be evaluated.

During Run 1, the TCDI set-up validation was performed with the so-called "distribution cut method". For Run 2 instead, the validation was done using the simulated loss maps of the TLs. In this case, also the previous methodology was still carried out for benchmarking purposes.
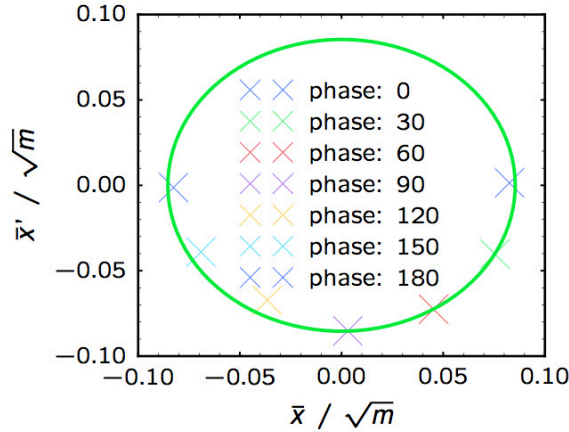
Figure 7.5 – Normalised horizontal phase-space at the end of TI2 (B1 injection septum). The crosses indicate the trajectory normalised position and transverse momentum of each oscillation excited in the horizontal plane of TI2 for the validation procedure.

BLM signal calibration

A prior BLM signal calibration to convert the BLM readings in lost protons is needed for the TCDI validation process.

The calibration is performed positioning each collimator jaw, one at the time, at $n\sigma$ ($n = 1$ for the distribution cut method and $n = -5$ for the loss map method) from the previously evaluated beam centre (Fig. 7.6). Measurements of the transverse emittance, vertical and horizontal, and beam intensity are also needed.

To infer the calibration factors C_c some assumptions are made:
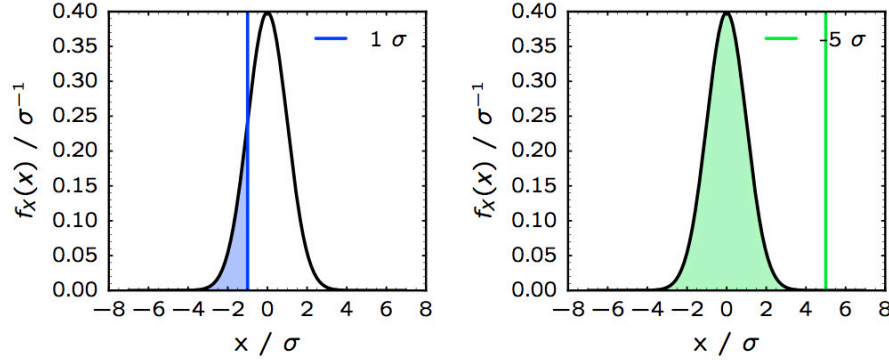
Figure 7.6 – Schematic view of the beam transverse cut for the calibration used by the two methods. Left - The $1\,\sigma$ cut needed for the distribution method is shown. Right - The almost total impact used for the loss map method is shown. For $1\,\sigma$ impact parameter about $15.9\,\%$ the particles are intercepted, instead for an impact parameter of $-5\,\sigma$ only $3 \times 10^{-5}\%$ are not intercepted by the collimator jaw.

- Nominal lattice functions are considered (values obtained from MADX reference optics file);

- A momentum spread of $\delta_p = 1 \times 10^{-4}$ is assumed;

- Perfectly Gaussian beam in both transverse planes;

- No positioning error considered for the collimator jaw at $1\,\sigma$.

The beam extracted from the SPS, if not scraped, has very pronounced tails [58]. Hence, having the beam scraped during the validation procedure, justifies the second last assumption.

The actual beam size is then calculated from the emittance measurements in the SPS as

$$\sigma_{meas} = \sqrt{\epsilon_{meas}\beta_x + D_x^2\delta_p^2}. \tag{7.5}$$

As previously stated, the transverse particle distribution is assumed Gaussian, $\mathcal{N}(0, \sigma_{meas})$, hence the percent of beam intercepting the collimator jaw, at 1σ from the centre, is calculated evaluating the cumulative distribution function (CDF) $F(x)$ at the jaw position. This can be formally written as:

$$C_c[\frac{p^+}{Gy}] = \frac{F(x)|_{x=n\sigma}}{L_{BLM}[\frac{Gy}{p^+}]}. \tag{7.6}$$

where L_{BLM} is the BLM reading normalised to the beam intensity. The calibration factor is essential for both methods that will be presented in this section. Using the maximum

measured shot-to-shot trajectory variations (Table 7.5), i.e. $0.5\,\sigma$, and considering all the rest ideal, the error in the estimated amount of beam intercepted by a collimator with $1\,\sigma$ impact can be up to $100\,\%$. This implies that several shots are needed for the calibration. The error introduced by the shot-to-shot line instability is basically negligible, i.e. $\sim 3 \times 10^{-4}\%$, using a calibration factor with $-5\,\sigma$ impact parameter. Of course, both way of calibrating BLM readings will suffer from other error sources, e.g. saturation.

Table 7.5 – Maximum shot-to-shot trajectory variation in both SPS-to-LHC transfer lines at collimator locations. The data were taken during Run 2 commissioning [22]. The confidence level is at $3\,\sigma$.

Transfer line	Plane	Max Error [σ]
TI8	hor	0.50
TI8	ver	0.22
TI2	hor	0.34
TI2	ver	0.18

Distribution cut method

Once the calibration factor C_c has been calculated for the BLM associated to each collimator, the validation procedure is carried on as describe in Sec. 7.3.1.
The betatron oscillations excited to sample the full phase space are off-setted with respect to each other by $\pi/6$ and the amplitudes scaled to 4, 4.5 and $5\,\sigma$. For each of them, losses from the first BLM in the line with a significant signal are recorded. Multiplying such BLM signal by the corresponding C_c and inverting the CDF, the distance from the beam centroid and the aperture bottleneck for that specific oscillation phase is calculated. Repeating this procedure for all the phases, the maximum escaping amplitude as a function of the oscillation phase can be obtained. An example of such a measurements is shown in Fig. 7.7. Assuming the error on the jaw position, as obtained from Table 7.3, the results of the validation procedure are compared with Eq. (7.3) (Fig. 7.7), i.e. $7.4\,\sigma$ for the present system.
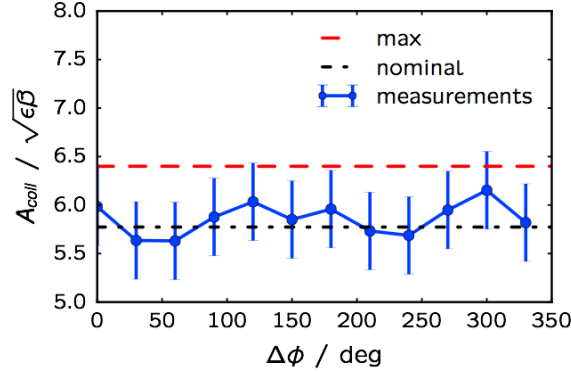
Figure 7.7 – TCDI set-up validation results for the horizontal collimators of TI2 using the distribution cut method. The blue line represents the measurements taken during the LHC commissioning for Run 2 in 2015. The dashed red line is the theoretical maximum amplitude that can be injected into the LHC, taking into account the maximum jaw position errors for the chosen settings, i.e. $5\,\sigma + 1.4\,\sigma$. The dashed black line represents the ideal jaw setting.

Model for TCDI set-up validation and new validation methodology

An improved method comprises simulate loss patterns for every required oscillation and compare them with the measurements. To do so, a new scattering routine was written in Python (`pycollimate`) and successfully interfaced with MADX.

In order to produce realistic loss maps, two type of simulation codes are necessary: one tracking particles inside accelerator active elements (e.g. MADX, PTC, SixTrack, etc.) and one tracking particles inside matter (i.e. scattering routine). Different simulation tools were investigated (*SixTrack extended for collimation* or ORBIT [59]), which already provides the combination of the required tracking codes, but none of them could be directly used to produce loss maps of the transfer lines (not suitable for non-circular machines, or completely different target energy). This led to the development of a new tool to simulate the validation process; that is `pycollimate` (a new scattering routine written in Python) interfaced with MAD-X and MADX-PTC (for the active elements tracking). The interaction processes of protons with matter, relevant for collimation studies, were already investigated in literature [60, 61]. The scattering routine implemented in *SixTrack extended for collimation* (based on K2) is a Monte Carlo routine for tracking particles inside matter. The relevant processes considered, can be divided in four groups: nuclear interaction with finite cross section, Coulomb scattering, ionisation losses and hard electro-magnetic processes. The latter are actually marginal below proton energies of 10 TeV, hence they can be neglected for the energy range of interest, i.e. 450 GeV to 7 TeV.Starting from the same assumptions, the new scattering routine mainly uses the same physical model implemented in *SixTrack extended for collimation* (also taking into

account updated cross-sections [62] thanks to new available experimental data), although different features are also included. For instance, the possibility to apply a very wide set of imperfections to each collimator jaw independently is implemented. It can be interfaced with MADX-PTC and perform thick lens tracking; particles escaping the collimator jaw before its end can be tracked also using the exact Hamiltonian in the remaining drift space.The scattering routine lives as a function in the Python package `pycollimate`, which also includes all the tools to communicate with MADX, as well as classes and functions to characterise the scenario under analysis. This lets the user customise the simulation environment very easily and offers also the possibility to extend it without needing to modify the library source code directly; this is only one of the many advantages carried by a reusable generic library. Also, the complete independence of the scattering routine makes it usable with virtually any other accelerator tracking codes. The flexibility of the Python language allows a user of the `pycollimate` library to provide his/her own implementation of the scattering process and have it automatically invoked by the library scattering routine itself.
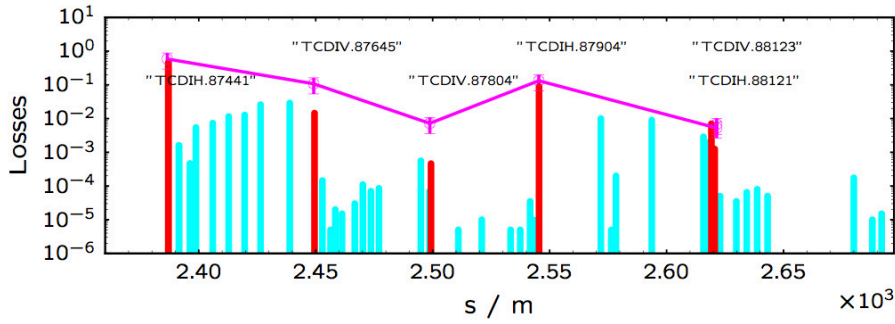
Figure 7.8 – Example of simulated TL loss map. The two different histograms (red and cyan) in the loss map refer to two different kind of losses: the red ones refer to protons that have undergone to an inelastic scattering inside the collimator jaws, the cyan ones refer to protons lost inside the machine elements that are not collimators. In magenta the BLM readings expressed in particle lost.

In Fig. 7.8 an example of simulated and measured TL loss map is shown; this corresponds to the horizontal oscillation at $\phi_x = 60°$ (maximum of the oscillation at $\phi_x = \phi_x^{MSI} + n2\pi$, where ϕ_x^{MSI} is the horizontal phase-advance at the MSI) with $5\,\sigma$ amplitude. To obtain such a loss pattern, a bivariate distribution is tracked from the SPS extraction to the MSI entrance. The tracking is performed keeping the collimator at $5\,\sigma$. From the simulated loss maps, the collimator apertures as a function of the oscillation phase can be calculated. In order to account also for the TCDI imperfections, a sample of 20 seeds (20 different collimator settings taken from a Uniform distribution truncated at $1.4\,\sigma$, Table 7.3) has been used. This gives the range of collimator apertures that one should expect for a single oscillation phase. The collimator aperture seen by the beam as a function of the

oscillation phase can be calculated with the assumption that the beam is transversally Normally distributed. Under this assumption, the proton lost at one collimator can be used to retrieve its distance from the beam. In Fig. 7.9, a comparison of the measurements obtained during the Run 2 commissioning in 2015 and simulations is shown. This plot shows the measured and simulated apertures of the different collimators (identified with the phase of the oscillation as reported in Table 7.6). For the measurements of the horizontal collimators in TI8, it is clearly visible a mismatch between simulations and measurements. This was due to the wrong settings of the correctors used to generate the oscillations in the line. Thanks to the just described model, such an error could be discovered and fixed. This was one of the main improvements, since the distribution cut method was not able to detect erroneous oscillation parameters. To note, the experimental results of the validation procedure were re-analysed using the measured TL trajectories and, compensating for the discrepancy, the TCDI settings were validated.

Table 7.6 – Collimators at which the maximum losses are recorded as a function of the oscillation phase.

| | **Collimators** | | | |
Oscillation phase	TI2 Hor	TI2 Ver	TI8 Hor	TI8 Ver
0°	TCDIH.29465	TCDIV.29509	TCDIH.88121	TCDIV.88123
30°	TCDIH.29050	TCDIV.29012	TCDIH.87441	TCDIV.87645
60°	TCDIH.29050	TCDIV.29012	TCDIH.87441	TCDIV.87645
90°	TCDIH.29205	TCDIV.29234	TCDIH.87904	TCDIV.87804
120°	TCDIH.29205	TCDIV.29234	TCDIH.87904	TCDIV.87804
150°	TCDIH.29465	TCDIV.29509	TCDIH.87904	TCDIV.88123

The collimator aperture estimation, as just described, has an intrinsic inaccuracy coming from scattered protons and non-parallel beam trajectory to the collimators. This can be observed in Fig. 7.9 for the ideal case (black line). This represents the simulated collimator aperture, resulting from the procedure described above, as a function of the different oscillation phases. One would expect to have a flat line at 5 σ; this is not the case due to primary protons that can escape the collimators, secondary protons coming from previous interactions and primary protons lost in the machine apertures that are not collimators. In fact, as expected, the most accurate estimation of the collimator apertures are for the collimators most upstream in the lines, e.g. $\Delta\phi = 60°$ for TI2 horizontal.

Comparison of validation methods

The main differences between the two described methods can be summarised as following:
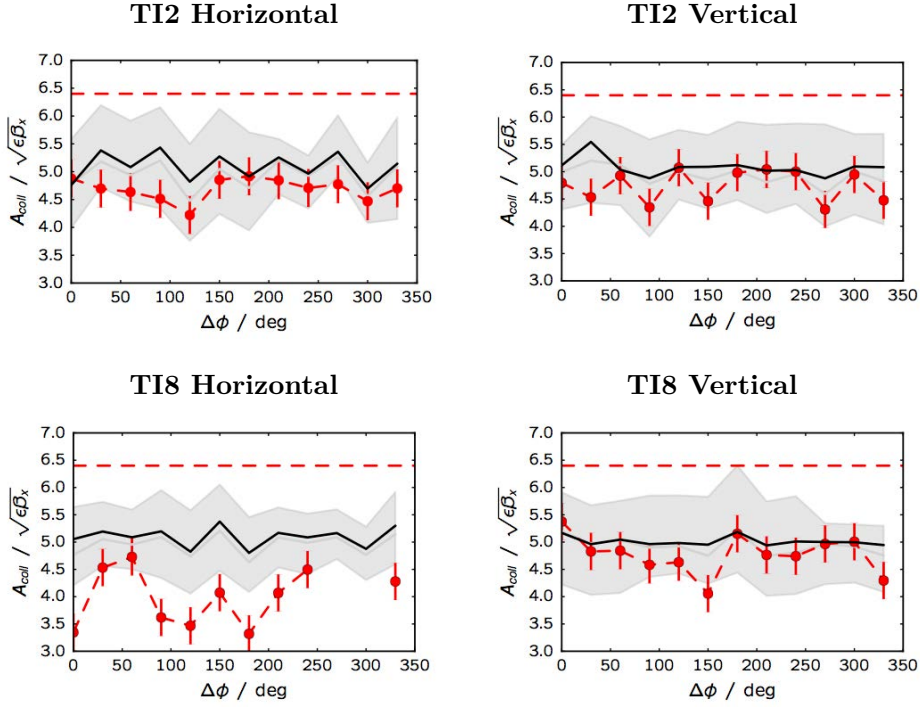
Figure 7.9 – Results of the new validation procedure (loss map methodology) for the horizontal plane of TI2. Here the BLM normalised readings (red dots) and simulations are compared. The black line represents the simulation results for the ideal TI2 configuration, instead the grey shaded area represents the expected range of values that the validation procedure can give. This area has been obtained simulating 20 different possible collimator configurations (maximum half gap error of $1.4\,\sigma$).

- The available simulated loss maps permit to avoid the three steps in amplitude previously needed each time due to the uncertainty on the expected loss pattern. This translates in an almost factor of three reduction in the time needed for the set-up validation procedure [1];

- With the loss map method, there is no arbitrary selection of BLMs because all BLMs at the collimators are used to evaluate the set-up;

- For the distribution cut method, the maximum theoretical oscillation amplitude in the line is considered, although this is not the case in general. This can be a critical assumption in case the oscillations are far from the ideal one, e.g. corrector setting errors, which can translate in significant errors in the validation of the collimators set-up (see results shown in the previous subsection);

- Used calibration factor: $1\,\sigma$ impact parameter from the distribution cut method and $5\,\sigma$ impact parameter for loss map method. For the first case, this translates

---

[1]Two amplitudes have been checked do evaluate the effectiveness of such a method, i.e. $[5,6]\sigma$

in a large error due to the shot-to-shot variation of the TL.

The two methods have been used together during the commissioning of the SPS-to-LHC transfer lines for comparison. The new proposed method permitted to discover an error in the hardware settings, which instead was not observed with the distribution cut method. Also, it has been shown that the new methodology permits to significantly reduce the beam time needed for the validation process.

7.4 HL-LHC injection protection system

The beam coming from the SPS trough the two transfer lines is horizontally deflected by the injection septum, MSI, and vertically by the injection kicker, MKI. The injected beam has to be deflected by $\theta_{MKI} \approx 850\,\mu\text{rad}$ to be brought onto the nominal orbit.

The injection kicker system is composed by four magnets per ring. The total integrated field, for the nominal deflection required, is $1.2\,\text{T m}$, and the field flat-top length is $\approx 8\,\mu\text{s}$ (for nominal injection of 288 bunches). The rise and fall time of the MKI magnetic field have to be very short, i.e. $0.9\,\mu\text{s}$ and $3.0\,\mu\text{s}$ respectively. The reason of such tight requirements (on fall and rise time) is because this defines the minimum possible space between LHC batches and hence the maximum number of bunches usable for LHC physics. To preserve the beam emittance during the injection process, the MKI flat top ripples amplitude must be below $\pm 0.5\,\%$ the nominal field [16].

Each MKI tank is equipped with its own Pulse-Forming Network (PFN). Two resonant charging power supplies (RCPS) per system are used to charge the PFNs and a main and a dump switch are required at both ends of the PFN to control the pulse duration (Fig. 7.10). A well matched high bandwidth system is required to satisfy these requirements. This is achieved with a multi-cell PFN and a multi-cell travelling wave kicker magnet, both connected via a transmission line terminated by a matched resistor [14].

Due to the very short time scale at which the kickers operate, dedicate systems are protecting the machine against its failures. The main systems responsible for the MKI surveillance are: the Beam Energy Tracking System (BETS), the re-triggering in case of erratics and a set of passive protection devices. The BETS controls the voltage of the PFN with respect to the expected beam energy (estimated from the main magnets current). In case of discrepancy between the measured and the reference value of more than $0.5\,\%$, the MKI pulse (hence the injection) will be inhibited and the incoming beam will be dumped on to the TDI. This is possible up to $250\,\text{ns}$ before the moment of injection.

 The re-triggering system is responsible for the triggering of the whole system in case of a spontaneous trigger of one of the main switches. The re-triggering of the whole system is done in order to minimise the number of bunches that could escape the passive injection protection system.

As already introduced in Sec. 7.2, the LHC needs to be protected by possible MKI failures.
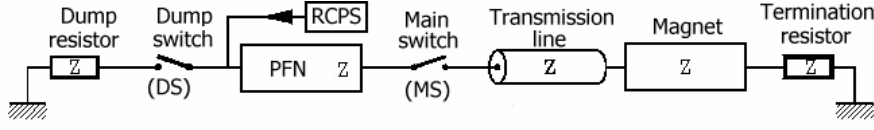
Figure 7.10 – Schematic representation of the LHC injection kicker circuit. [16].

The passive injection protection system is composed by a main absorber, TDI, and by two auxiliary devices TCLIA and TCLIB. The TDI is a 4 m long device made of two jaws (above and below the beam CO). Each of them comprises a first block 157.7 cm of graphite R4550 (density of $1.83 \, g/cm^3$), followed by one 600 mm long aluminium block and one 700 mm copper block. The TCLIA is 1 m long and is made of R4550. The TCLIB, instead, is 1 m long as well, but completely made of lower density graphite than R4550, i.e. $1.65 \, g \, / \, cm^3$.

The TDI is the main protection against MKI failures - it is installed at about 90° vertical phase-advance from the MKI to maximise the guaranteed protection. The TCLIA and TCLIB protect against possible phase-advance errors between the MKI and the TDI; they are placed at $\Delta\mu_y \approx 180° + 20°$ and $\Delta\mu_y \approx 360° - 20°$ from the TDI respectively. A schematic view of the LHC injection protection system is shown in Fig. 7.11. The aperture of the injection protection elements has to be $n_{setting} \leq 7$ [57, 23] to guarantee the protection of the LHC cold bore aperture of $7.5 \, \sigma$. All LHC injection protection elements are then set to $n_{setting} = 6.8 \, \sigma$.
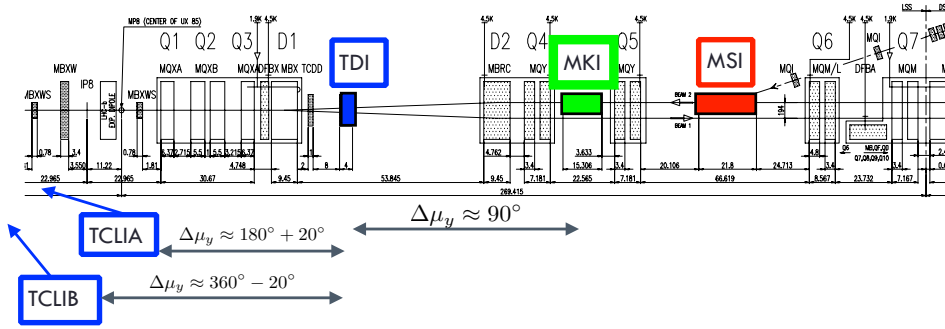
Figure 7.11 – Schematic representation of the LHC injection system [16].

7.4.1 MKI failures

In case of charging failure, erratic or missing triggering of one switch and timing error, the circulating (or the injected) beam could be swept across the LHC aperture or completely dumped onto the TDI. This could happen any time during the PFN charging process, hence the resulting MKI waveform could have a shorter flat-top (4.1 µs) at any field value up to the maximum. This yields to a maximum of 186 bunches (considering 225 ns

batch spacing and 25 ns bunch spacing) that can be deflected at any angle. An electrical breakdown, i.e. a sudden transition from dielectric to conductor of the vacuum in the magnet, needs also to be included among the possible failures. Depending on the longitudinal location of the breakdown, the field seen by the beam can be either reduced or amplified. A short circuit is created and the pulse is reflected - if this happens right at the beginning of the magnet, the current in that magnet will be zero; if it happens at the end instead, the current is doubled and so the field. This can affect the whole injected beam (maximum of 288 bunches for 25 ns operation) as well as the circulating one. In case of flash-over in more than one magnet simultaneously, the system can provide up to a maximum of twice the design field (i.e. 200 %). Failures of the MKI have a periodicity of a few events per year [63]. Due to the relatively low probability (accounting for the number of pulses per year) of a single failure, the odds of an event where two or more failures happen at the same time becomes negligible. For this reason, a kick of $2\,\theta_{\mathrm{MKI}}$ is only possible on the injected beam. The maximum erroneous deflection that the MKI can give to the circulating beam in case of a spurious trigger is θ_{MKI}. FIg. 7.12 shows the possible trajectories that can be originated from an MKI failure.
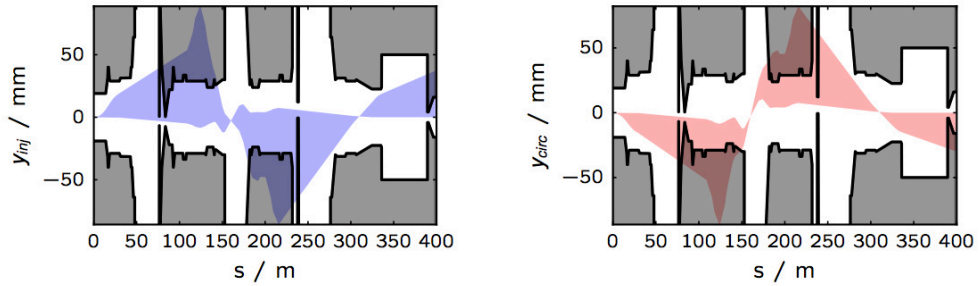
Figure 7.12 – Range of trajectories originated from MKI single failures for Beam 1. Left, possible trajectories for a failure of the MKI on the injected beam. Right, possible trajectories for a failure of the MKI on the circulating beam.

This possible range of kicks, defining the deflection as $k_{MKI} \equiv p\theta_{MKI}$, can be categorised according to the machine components that will be put more at risk (assuming injection protection element settings of $n_{setting} = 6.8\,\sigma$) as a function of p:

- $0 \leq p \leq 6.7\,\%$: The oscillation amplitudes are below $6.5\,\sigma$ and do not represent a treat for the LHC aperture. This oscillations will be caught by the primary collimators in IR7.

- $6.7 < p \leq 14.2\,\%$: *grazing* and *quasi-grazing* impact on the TDI. In this case, the impact parameter of the miss-kicked beam on the TDI is $0 \pm 2\,\sigma$. The grazing corresponds to an impact parameter on the TDI of exactly $0\,\sigma$ (Fig. 7.13). The rest of the range is identified as quasi-grazing impact. this is the worst case for stresses induced in the material of the TDI and the TCLIA/B. Also, this range of kicks is the

most critical for all the machine components downstream of the injection protection system. The reasons of such statements are given in the following subsection.

- $14.2 \leq p \leq 100\,\%$ (only circulating beam): The impact parameter on the TDI is large enough to reduce the beam intensity to a safe value. Due to the TDI composition, its nuclear interaction length at injection energy is $\sum_i L_{\lambda,i} \approx 13$, where $L_{\lambda,i}$ are the nuclear interaction lengths of the i-th material that composes the TDI. Hence the probability for a primary proton to not perform an inelastic collision is given by:

$$P(\lambda) = e^{-(\sum_i N_{\lambda i})} = 2 \times 10^{-4}\,\%. \tag{7.7}$$

This means that the amount of secondary protons escaping the TDI, in case of a large impact parameter, is basically negligible.

- $p > 100\,\%$: This deflection translates in a beam impact parameter that could compromise the integrity of the TDI tank. The kicked beam could reach sensitive parts of the TDI tank and hence damage it.
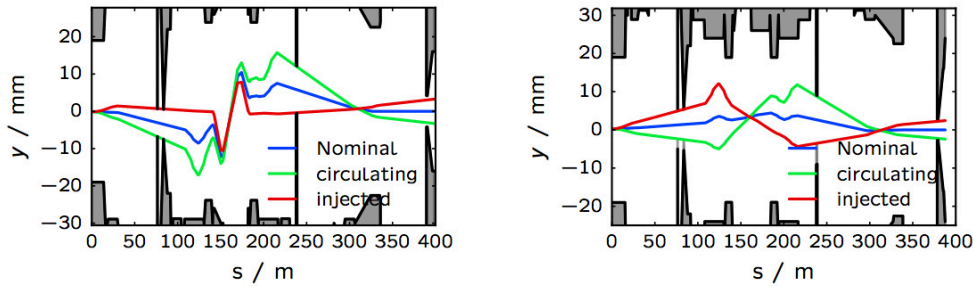
Figure 7.13 – Grazing trajectories of B1 (left) and B2 (right) for k_{MKI} equal to $11\,\%$ and $9.5\,\%$ for B1 and B2, respectively. The blue line represent the nominal closed orbit. The green line represents the beam trajectory, in case of failure of the MKI acting on the circulating beam. The red line represents the beam trajectory, in case of failure of the MKI acting on the injected beam.

7.4.2 Grazing impact on the TDI

The worst MKI failure for two cases will be evaluated in terms of:

- Primary beam load on the TCLIA and TCLIB;

- Load on the LHC elements downstream of the injection protection system.

During LHC Run 1 (2010-2012) eight failures of the MKI have been recorded (Table 7.7). More than $50\,\%$ of these failures translated in the full impact (no firing of the MKI) of
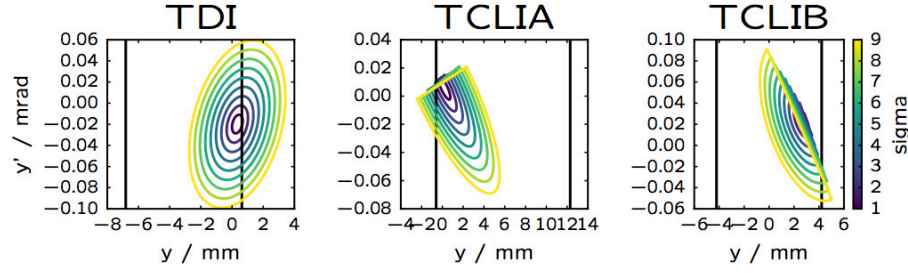
Figure 7.14 – Single particle emittances in vertical transverse phase-space at the 3 different injection protection devices for MKI failure. The colour code represents the different transverse sigma extension. The black solid lines represent the ideal aperture of the injection collimators.

the non-kicked injected beam on the TDI. No quenches were triggered and operation could continue without major problems, nevertheless the beam was dumped due to losses. In all the other cases, the MKI caused the grazing (or quasi-grazing) of the beam on the injection protection devices [63]. The energy deposited on the superconducting magnets, due to the escaping secondary showers from the TDI, was considerably high [64] and magnet quenches occurred in all these cases.

Table 7.7 – Injection kicker (MKI) failures recorded between 2010 and 2012 LHC operation [63] [64]. The resulting kick is expressed in percent of the nominal one.

Date	Beam	Kick (%)	Bunches affected
23/10/10	B1/inj.	0%	32
18/04/11	B2/inj.	$\approx 110 - 125\%$	36
23/04/11	B1/inj.	0%	36
27/04/11	B2/inj.	0%	72
28/07/11	B1/inj.	0%	144
28/07/11	B1/circ.	$\leq 12.5\%$	176
26/03/12	B2/inj.	0%	1
15/04/12	B2/inj.	$\approx 110 - 126\%$	108

In [64], two cases (28/07/11 and 18/04/11) among those in Table 7.7 have been analysed due to the number of magnets which quenched. On July 28th 2011 the circulating B1 was deflected by an erratic trigger of the MKI causing a quasi-grazing impact on the TDI ($\approx 12\%$ of nominal kick) of about 162 bunches (estimated value). The separation dipole D1, upstream of the IP, and the downstream the D2, quenched, together with the triplet quadrupoles. Also ALICE was effected by such a failure with permanent damages to the Silicon Drift Detector [64].
On April 18th 2011, a flashover in the MKI8 made the injected B2 to be miss-kicked and

causing a quasi-grazing impact on the TDI. In this case, the triplet quadrupoles closer to the MKI, 8 main dipoles downstream the TCLIB and the Q6 were directly quenched (plus other 6 main dipoles for quench propagation) by the beam losses.

Due to the number of quenched magnets downstream of the TCLIB, for the just cited events, the settings of the TCLIB were reviewed. It was thought that the tight settings $(6.8\,\sigma = 4.96\,\mathrm{mm}$ for B1 and $2.8\,\mathrm{mm}$ for B2) of this device could be potentially armful for the cold magnets placed after it, due to the scatter of primaries protons from the TCLIB. In fact, during the end of the LHC Run 2, the TCLIB jaws were set at $8.3\,\sigma$ from the circulating beam [65]. Further analysis, though, showed that the protection of these super-conductive magnets was guaranteed also with TCLIB half-hap pf $6.8\,\sigma$ since the load due to primary protons was below the damage level.

Maximum load on TCLIA and TCLIB

The TCLIA and TCLIB are partially "protected" from direct impact of primaries from the TDI. The TCLIB is expected to see primaries, in case of grazing impact on the TDI, only if their initial amplitude is above $5\,\sigma$ (Fig. 7.14). The TCLIA, instead, is designed to see primary beam also very close to the core.

The TCLIA and B have been built to withstand the ultimate LHC beam parameters. A very conservative approach was used in the initial estimation of the possible beam that these devices should withstand; the impact of the full injected beam (288 bunches) was considered as the limit scenario. For the HL-LHC beam brightness upgrade, such an approach would mean that a re-design is needed. This scenario, though, is not realistic due the injection protection strategy. Detailed studies considering different machine configurations are needed to assess the realistic upper limit of the possible load of primary beam on these collimators.

A set of 500 randomly generated machine configurations was produced, using standard errors listed in Table 7.8, to evaluate the MKI kick for which the highest intensity is expected at the TCLIA and TCLIB. The effect of these errors translates into a r.m.s. closed orbit and β–beat as shown in Fig. 7.15.

Table 7.8 – Errors assumed for the generation of different machine configurations.

Type	Error	Standard deviation
Dipoles	B/B_0	15×10^{-6}
Quadrupoles	k/k_0	15×10^{-6}
Quadrupoles	Misalign	$33\,\mu\mathrm{m}$
Correctors	B/B_0	30×10^{-6}
Closed Orbit	$u - u_{CO}$	$0.05\,\sigma$
Beta functions	$\Delta\beta/\beta_0$	2×10^{-3}
Phase advance	$\Delta\mu/\mu_0$	1×10^{-3}
Dispersion	$\Delta D/D_0$	2×10^{-3}
TDI	Jaw gap	$0.36\,\sigma$
TCLIA/B	Jaw gap	$0.04\,\sigma$
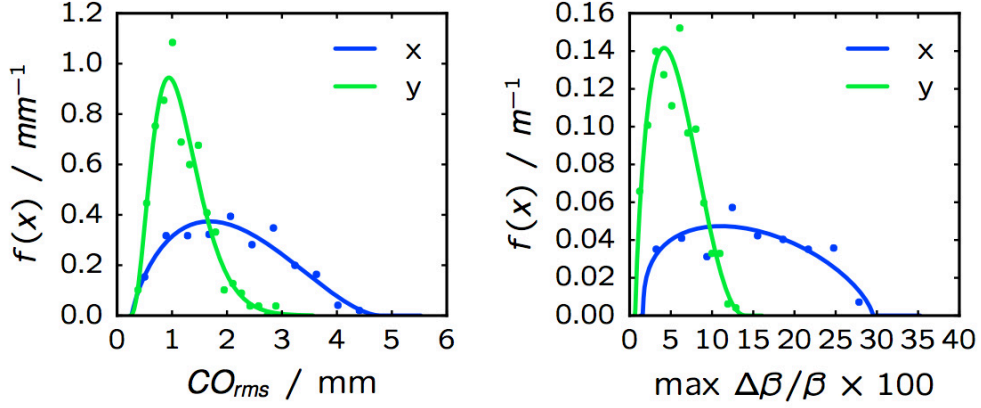
Figure 7.15 – (Left) Distribution of closed orbit rms of the whole LHC for the 500 different machine configurations simulated. (Right) Distribution of the maximum β–beating (in percent) in the whole LHC for the 500 different machine configurations simulated. The medians for the CO rms are: $x_{CO} = 1.7\,\mathrm{mm}$, $y_{CO} = 1.0\,\mathrm{mm}$. For the fractional beta-beating, the medians are: $\Delta\beta_x/\beta_x = 10\,\%$, $\Delta\beta_y/\beta_y = 4\,\%$.

For each seed, the cut from one of the injection protection devices is estimated in terms of the intercepted area of the single particle emittance, at a maximum of $6.8\,\sigma$ (collimator half aperture). This is done by numerically calculating the integral of the single particle emittance after reshaping it as a consequence of the cut induced by the interaction with a collimator (Fig. 7.14). In Fig. 7.16, the fraction of the area of the initial single particle emittance, ϵ_0, is expressed as:

$$-\frac{\Delta\epsilon}{\epsilon_0} \equiv -\frac{\epsilon_{cut} - \epsilon_0}{\epsilon_0}, \tag{7.8}$$

where ϵ_{cut} is the area of the single particle emittance intercepted at a given collimator. This gives an indication of how much beam is expected to be lost on the different injection protection devices. For a conversion in actual particle losses though, tracking simulations are needed and they will be discussed in the following section. In Fig. 7.16 the normalised emittance cut as a function of the MKI kick strength is shown for B1 (equivalent results are also obtained for B2). As shown in Fig. 7.16, the maximum load on the TCLIA and TCLIB is obtained for MKI deflections close the TDI-grazing condition.
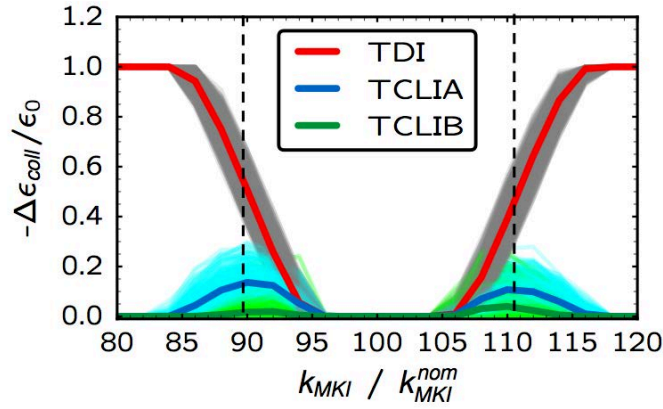
Figure 7.16 – Single particle emittance cut from the three injection protection elements as a function of the MKI kick for B1. For B2 the situation is equivalent. The solid thick lines represent the average over 500 simulated seeds (machine configurations) at a fixed MKI kick. The shaded lines represent the results from each individual seed and the dashed line indicate the kick percentage for a grazing impact.
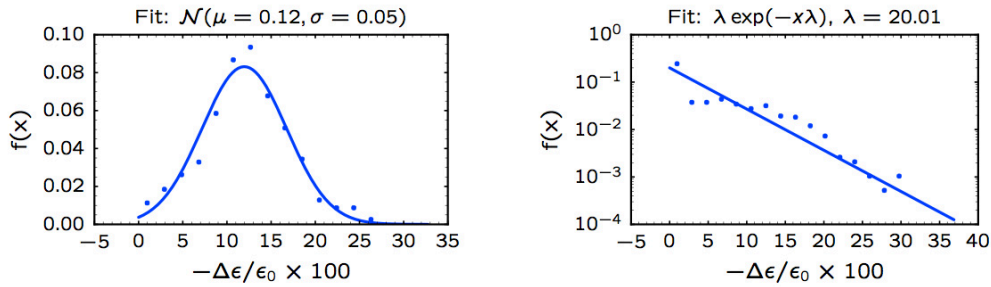
Figure 7.17 – Left (Right) - Normalised histogram (blue dots) and corresponding Gaussian fit (slid blue line) of the single particle emittance area intercepted by the TCLIA (TCLIB) for the 500 machine configurations simulated.

The results of the Monte Carlo simulation are the PDF of the fractional emittance cut, $\Delta\epsilon/\epsilon_0$, at the TCLIs (Fig. 7.17). An average of 12 % of ϵ_0 is expected to intercept the TCLIA. For the TCLIB instead (Fig. 7.17-right), the PDF shows a small likelihood of a significant number of primaries hitting it. In extreme cases, up to 30 % of the phase-space

area considered is intercepted at the TCLIA or TCLIB. This gives an indication of the maximum number of bunches which one could expect to intercept the TCLIs and their probability distributions. Concluding, in a very pessimistic situation, a maximum of 30 %, i.e. 84 bunches, of the total beam intensity is expected to hit either of the auxiliary devices.

Worst MKI failure for the rest of the LHC

Figure 7.18 – Plots of the analytical relation between intensity of the maximum amplitude surviving the TDI and deflection induced by the MKI for different beam emittances.

For the other machine components, the evaluation of the most dangerous kick can be formally done using the assumption that the beam is transversally Normally distributed and the TDI is a perfect absorber, i.e. no primary proton survives the impact. This also means that the following calculations relay on the fact that the TDI is correctly set-up at $6.8\,\sigma$.

The transverse vertical displacement Δy_{TDI} at the TDI, in nominal LHC sigma, induced by an MKI kick (k_{MKI}) can be written as:

$$\Delta y_{TDI}(k_{MKI}) \equiv \frac{\sqrt{\frac{\beta_{TDI}}{\beta_{MKI}}}(\cos(\Delta\psi) + \alpha_{MKI}\sin(\Delta\psi))y_0 + (y_0' + k_{MKI})\sqrt{\beta_{MKI}\beta_{TDI}}\sin(\Delta\psi)}{\sigma},$$

$$(7.9)$$

where β and α are the beta and alpha lattice functions at the MKI and at the TDI, and $\Delta\psi$ is the phase-advance between the MKI and the TDI. The distribution of the circulating and/or injected beam, kicked by the MKI, can be expressed as a function of

k_{MKI} replacing the mean with $\Delta y_{TDI}(k_{MKI})$. The PDF of the kicked beam is thus:

$$f(y|\mu = \Delta y_{TDI}, \sigma_N = \sigma_{real}/\sigma) \equiv \frac{1}{\sqrt{2\pi\sigma_N^2}} e^{-\frac{(y-\mu)^2}{2\sigma_N^2}} \; ; \tag{7.10}$$

where σ_{real} is the betatronic beam size calculated with the actual beam emittance and σ_N is the standard deviation of the distribution. The most dangerous MKI kick, in this case, can be defined as the one that determines the maximum intensity escaping the TDI with the largest possible amplitude. For nominal TDI settings and under the assumptions made at the beginning, the maximum amplitude that can escape the TDI is $6.8\,\sigma$. Then a function of Δy_{TDI} that gives the intensity at this amplitude can be defined as:

$$\chi(\Delta y_{TDI}, \sigma_{real}) = N_p \int_{6.8}^{\infty} f(y|\Delta y_{TDI}, \sigma_{real}/\sigma) dy \int_{-\infty}^{6.8 - \Delta y_{TDI}} f(y|0, \sigma_{real}/\sigma) dy \tag{7.11}$$

where N_p is the total intensity of the beam. In Fig. 7.18, Eq. (7.11) is plotted as a function of both emittance and MKI kick, to emphasise the fact that χ does not vary with the actual beam emittance. Hence, the maximum of Eq. (7.11) is obtained for $\Delta y_{TDI} = 6.8\,\sigma_{\text{LHC}}$ (i.e. for a grazing impact on the TDI).

7.5   Tracking simulations of injection failures

One of the main differences of the HL-LHC injection protection system is represented by the new TDI: the segmented TDI (TDIS). The present TDI will be replaced by such a new device for two main reasons:

1. Mechanical and operational issues of the present device;

2. Strength limit exceeded of the high-Z materials (last blocks) with the HL-LHC beams.

The first reason is due to difficulty in aligning and operating a 4 m block device with the present hardware. To overcome this issue, the TDI jaws will be segmented in three separated shorter blocks: the first two blocks will be 1.5 m, made of graphite (R4550 or similar), the last one instead will be made of higher Z material for 1.5 m. The last block is also 2 mm further away from the circulating beam than the others to avoid direct impact of the beam. The material composition of the TDIS blocks is still under investigation. For the following simulations, the first two blocks have been assumed made of graphite R4550 and the last made of aluminium and copper, as suggested by the design experts, due to the fact that the final design will have guarantee the same active length.

TCLIA and TCLIB: expected load and settings evaluation

The load on the auxiliary injection protection devices directly depends on the TDI misalignment. From Table 7.8, the maximum error ($>99\,\%$) on the TDI jaw (only mechanical) can be considered $1\,\sigma$. In case of such a misalignment, the TCLIA is exposed to less than $20\,\%$ of the injected beam at the first turn. The load on the TCLIB, instead, will not go above a few percent. This values are in agreement with the probability density functions obtained from the Monte Carlo simulation presented in this section. In fact, the maximum expected load on these devices can be considered as $30\,\%$ the total beam intensity, as discussed in the previous section.

In case of any MKI failure, on either circulating or injected beam, a dump request will be triggered from different interlocked elements. The delay from a dump request and the actual dump is three turns and hence the beam losses produced by such an event have to be integrated in this time interval. To assess the expected particles lost on the different machine elements and to evaluate the sharing per turn of the losses, multi-turn particle tracking was done.

As previously discussed, the maximum number of bunches that can be interested by a single failure of the MKI is 288, i.e. one full SPS train with $25\,\text{ns}$ bunch spacing. A sample of 2×10^5 particles have been tracked over 3 turns after a flashover of the MKI inducing a grazing impact on the TDI. An ideal machine was assumed, with injection protection elements at nominal settings ($6.8\,\sigma_{LHC}$) and with the TCLIB at $8.3\,\sigma_{LHC}$.
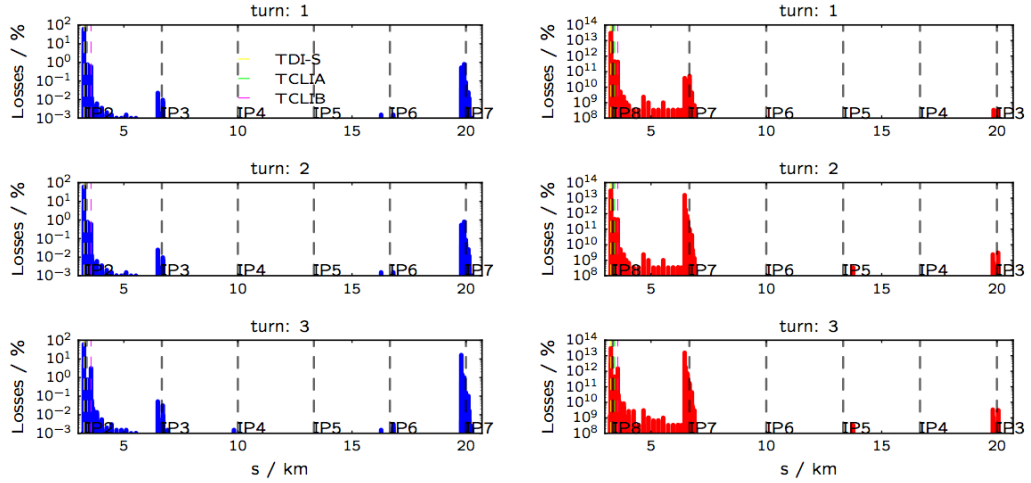
Figure 7.19 – Loss maps of the first 3 turns after MKI flashover. Blue for B1, and red for B2.

The highest losses occurred, as expected, at the first turn, for both B1 (Fig. 7.19 - left) and B2 (Fig. 7.19 - right): $70\,\%$ of the tracked particles are lost in the first machine
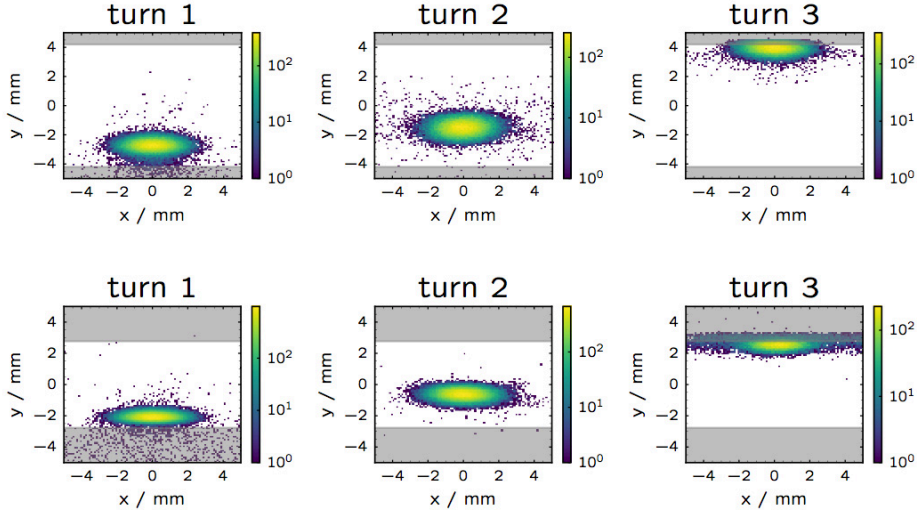
Figure 7.20 – Transverse particle distribution of B1 (top) and B2 (bottom) at the TCLIB in case od MKI flashover for 3 turns.

revolution and about 25 % in the third. The rest is sent to the dump. For B2 instead, about 45 % of the beam survives the first turn and the remaining part is shared between the collimation system ($\approx 20\,\%$) and the dump. For both beams, the particles lost at the TCLIB when is at $6.8\,\sigma_{LHC}$ at the third turn are about a factor 4 higher than at the first machine revolution due to the accumulated phase-advance (LHC vertical fractional tunes are close to 1/3). In Fig. 7.20 the tracked particle distributions at the TCLIB are shown for the first three turns following an MKI failure, for both B1 and B2. It is clear that at the third turn the impact parameter on the TCLIB is larger, translating in the highest number of protons lost at this device. No primary proton below $5\,\sigma$ is seen by the TCLIB in the first turn (see previous section), instead a few percent hits it in the third turn.

Comparing the expected losses in case of MKI flashover for the TCLIB at $6.8\,\sigma_{LHC}$ and $8.3\,\sigma_{LHC}$, it can be noticed that the larger gap allows to reduce losses in the dispersion suppressor section downstream of the injection region. The reduction of losses of secondary protons in the dispersion suppressor becomes very pronounced (about an order of magnitude) when integrating over three turns (Fig. 7.21).
In [65], the BLM signal $L[Gy/s]$ at the closest super-conducting magnet (Q6.L8 for B2) to the TCLIB as a function of the protons lost at the TCLIB was calculated:

$$L[Gy/s] = \frac{4.57 \times 10^{-13}}{40 \times 10^{-6}} N_p. \tag{7.12}$$

Using the simulation results shown in Fig. 7.21, the quench level is largely exceeded for both TCLIB settings (still well below the damage level). Hence, larger gap opening of
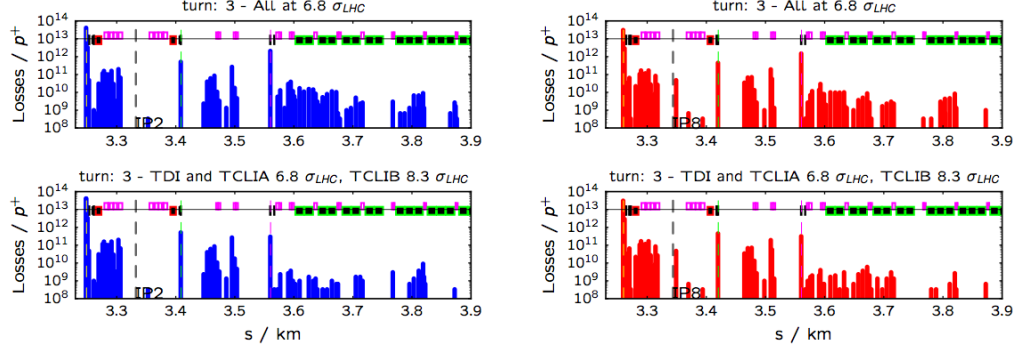
Figure 7.21 – Comparison of loss patterns in the injection regions for B1 (blue, left) and B2 (red, right) for different settings of the TCLIB three turns after an MKI failure, i.e. $6.8\,\sigma$ (top) and $8.3\,\sigma$ (bottom).

the TCLIB will only lead to a lost in protection, due its complementarity to the TCLIA. For these reasons, for the HL-LHC (and also for the current and future LHC) operation, the TCLIB should be placed at its design settings of $6.8\,\sigma$.

Evaluation of the minimum protected aperture at injection in case of injection failures

In order to evaluate the maximum amplitude with intensity above the set-up beam flag, the survival function $S(y)$ (Eq. (7.2) normalised to the beam intensity $(6.62 \times 10^{13}\,\mathrm{p}^+))$ of the tracked particles, in the cases of the above described failures, has been calculated at the exit of the injection protection system.

The amplitude at the exit of the injection system is calculated taking into account also particles transverse momenta (normalising the vertical action to the betatron beam size), that is:

$$Y = \sqrt{y^2 + (\beta_y y' + \alpha_y y)^2}/\sqrt{\epsilon \beta_y} \tag{7.13}$$

The maximum amplitude above the set-up beam flag is defined as $y = S^{-1}(5 \times 10^{11}\,\mathrm{p}^+)$. The simulations of MKI failures, as just described, have been carried out for both B1 and B2 and for different protection device configurations, as shown in Table 7.9.

The maximum error on the injection protection devices takes into account injection precision delivery [66], local orbit, optics discrepancy with respect to the nominal during setting-up and mechanical errors (Table 7.10). Optics errors corresponding to a beta-beat of maximum $10\,\%$ (Table 7.2), translate in a phase-advance error between the MKI and the TDI smaller than $10°$, hence they can be neglected. The error on the local orbit is assumed to be $\leq 0.9\,\sigma$. A bigger error will translate in high losses at one of the two jaws

Table 7.9 – Different scenarios of the protection devices configuration used to evaluate the maximum halo amplitude escaping the injection protection system.

Case	TDI (σ)	TCLIA (σ)	TCLIB (σ)
1	6.8	6.8	6.8
2	7.8	6.8	6.8
3	7.8	7.8	7.8
4	9.8	6.8	6.8
5	9.8	9.8	9.8

and a consecutive trigger of the beam dump. The errors have been added linearly and the most extreme cases were taken, in order to be as conservative as possible.

Table 7.10 – Maximum errors, at the TDI and TCLIs, assumed to evaluate the amplitude of the halo escaping the injection protection system.

Parameter set	Value (σ)
Injection precision	0.3
Mechanical tolerances	0.3
Setting-up optics	0.5
Local orbit	0.9
Total	2.0

The simulations were done for a 450 GeV beam with normalized emittance of $\epsilon_{x,y}^N = 1.37$ mm mrad. The simulated loss patterns for the three different protection device configurations are shown in Fig. 7.22 for both B1 and B2. Evaluating the survival function at the exit of the injection protection system (Fig. 7.23), the worst case is represented by the scenario with all protection devices misaligned by $2\,\sigma$ for B2. This gives the maximum amplitude of the halo with intensity equal to the set-up beam flag, that is $8.7\,\sigma$. Hence the maximum dangerous amplitude of the halo originated by the SPS extraction, transport and injection process shall be considered to be $8.7\,\sigma$, which corresponds to $10.3\,\sigma$ for a normalised emittance of 2.5 mm mrad. As shown in [51] this is not the worst case for the HL-LHC aperture. The minimum allowed aperture is in fact given by the asynchronous beam dump and it is $9\,\sigma$.

Figure 7.22 – Losses distribution on the HL-LHC elements in case of failure of the MKI for the protection devices configurations 1, 2, and 3. Left, for Beam 1 and right for Beam 2.
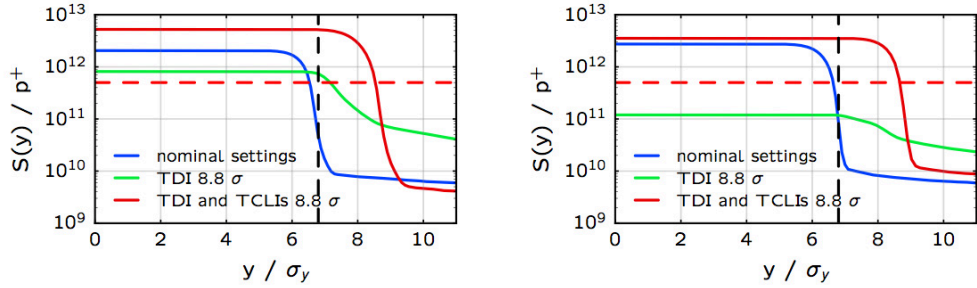
Figure 7.23 – Survival function of the tracked particle distribution at the exit of the HL-LHC injection protection system for B1 (left) and B2 (right) for the cases: 1, 4 and 5.

7.6   Experimental data from the present LHC injection protection system

In order to benchmark the simulations presented in this chapter, the experimental data taken on the present LHC injection protection system, for the validation with beam of the TDI settings, were used.

All injection protection devices were set to $6.8\,\sigma$ and centred around the established machine closed-orbit. Pilot beams (one bunch of $\leq 1 \times 10^{10}$ protons) are then injected and sent directly to the dump without completing a full revolution. Two super-conductive correctors, positioned between the MSI and the TDI, are used to steer the beam on to the TDI, simulating an MKI miss-kick. Such correctors are used to control the beam displacement at the TDI. The actual aperture of the TDI can be retrieved varying the
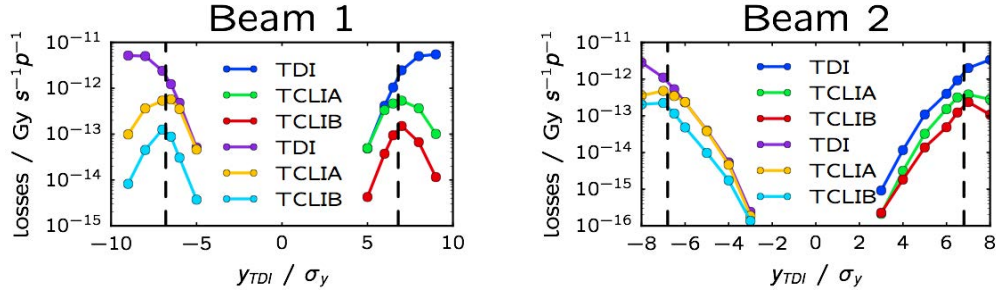
Figure 7.24 – Measured losses at the TDI, TCLIA and TCLIB during 2016 commissioning as a function of the theoretical beam displacement at the TDI. The BLM readings have been normalised with the measured beam intensity at the SPS extraction.
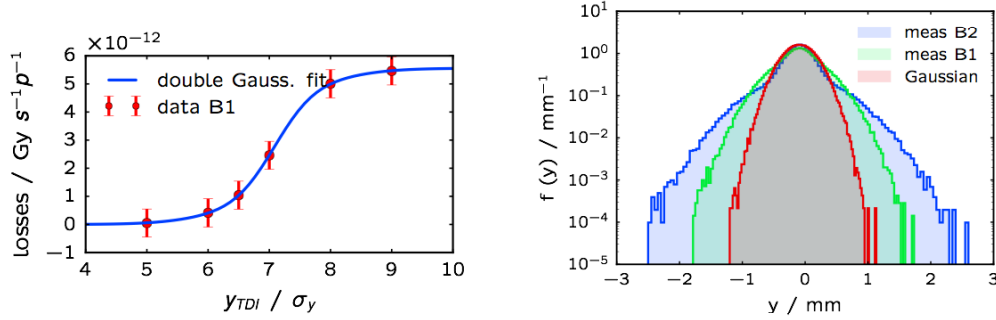
Figure 7.25 – (Left) Measured normalised losses at the TDI in IP2 (red dots) as a function of the theoretical beam displacement the the TDI. The solid blue line is a least square fit of the measurement point with a double Gaussian CDF. (Right) Reconstructed vertical beam profile distribution (for B1 and B2) with the data shown in Fig. 7.24 at the IP1. These are compared with the ideal Gaussian distribution (red) at the same location.

corrector strengths and recording the losses at the TDI, TCLIA and TCLIB. In Fig. 7.24, the measurements taken during the Run 2 commissioning are plotted. Here the signal of the closest BLM at each protection device was used. Their readings were normalised with the extracted intensity from the SPS. The black dashed line represents the theoretical settings of the collimators; the losses trend, at the TCLIA and TCLIB, is reverted between 6.5 and 7 σ (half nominal sigma was the resolution of the measurements), confirming that the aperture of the TDI jaw was between these values.

From these data, the beam profile at the TDI can be inferred. At the time of the measurements, the beam was not scraped in the SPS. As suggested in literature [58], the beam delivered in this way to the LHC is more likely to have a double Gaussian profile than being normally distributed. In fact, the TDI BLM data can be fitted with
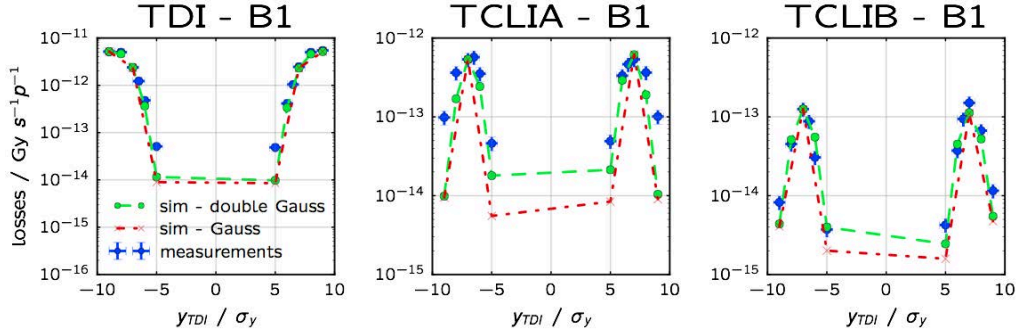
Figure 7.26 – Comparison of measurements (blue dots), form Fig. 7.24, and simulations (dashed lines) of losses induced by different MKI kick at the three injection collimators. In red are plotted the results from particle tracking starting with a Gaussian transversally distributed beam, in green the same tracking has been performed but using the beam vertical profile obtained from Fig. 7.25.

the function (Fig.7.25–left):

$$f(x) = c_1(1 - c_2)\frac{1}{\sqrt{2\pi}\sigma_1}e^{-\frac{(x-\mu_0)^2}{2\sigma_1^2}} + c_2 c_1 \frac{1}{\sqrt{2\pi}\sigma_2}e^{-\frac{(x-\mu_0)^2}{2\sigma_2^2}}, \tag{7.14}$$

where the same average, μ_0, is used for both Gaussian distributions due to the assumption of symmetric beam; c_1 and c_2 are scaling factors and σ_1, σ_2 the standard deviations of the two Gaussian distributions. The same procedure was repeated for both B1 and B2. The resulting distribution is plotted in Fig. 7.25 and compared with the ideal Gaussian distribution at the chosen location. The observable difference between the fit of B1 and B2 is thought to be originated from the impossibility to measure losses with high impact parameter in IP8 (B2). This was due the interlock triggering of the LHC-b experiment, which can inhibit the following injection in case of high recorded losses. Although the intensity used for these measurements was safely below any damage limit, the sensitivity of LHC-b monitors were systematically triggering the interlock. The data recorded were also sufficient to conclude of the well positioning of the injection protection elements.

To be able to compare simulations and measurements, a conversion from proton undergone inelastic scattering in the collimators and BLM signal has to be done. Previous studies [65] show the complexity in obtain reliable calibration factors for the injection collimator BLM data, hence the comparison is based on the ratio among different BLMs. In Fig. 7.26, the measurements form 2016 commissioning have been compared with two beam configurations: ideal Gaussian (red dashed line) and double Gaussian (green dashed line) beam. As expected, the main difference between the types of transverse beam distribution is visible for small displacements. At the TCLIA, the discrepancy with simulations reach the maximum for $9\,\sigma$ deflection of about an order of magnitude. The main source of disagreement between BLM readings and simulations is originated from

the fact that the simulations only account for primary and secondary protons lost at the different devices and not for electromagnetic showers.

7.7 The HL-LHC injection protection system

Failures of the MKI are a serious machine protection concern. The increase in brightness will translate in an increased danger if no countermeasures are put in place. The TDI properly protects, and still will, the downstream elements (mainly the D1 and the triplet), although its mechanical integrity can be compromised in case of direct impact of the full SPS train. A completely redesigned device, the TDIS, will replace the current TDI.

A model for the HL-LHC injection system has been developed and possible failure cases studied in detail. The settings for the injection collimators have been evaluated. The TCLIB settings were also explicitly checked due to the two different values used during LHC Run 1. Hence, following the results shown in this chapter, the TCLIB half-gap is suggested to be kept at $6.8\,\sigma$.

The maximum load, of primary and secondary protons, on the TCLIs is expected not the exceed $30\,\%$ of a full SPS $25\,\text{ns}$ beam. The probability of intercepting any primary proton is much higher for the TCLIA than the TCLIB in the first turn after an MKI failure. In the last turn before dumping, the TCLIB will be exposed to much more primaries, but this will not exceed the above quoted value.

A very good qualitative agreement between BLM readings and particle tracking has been shown. Due to the similarities with the model developed for HL-LHC and LHC, the prediction presented in this chapter for the new injection protection system can be considered validated.

CHAPTER 8

Conclusions and Outlook

The CERN physics program for the next decades includes exploitation of the LHC, its upgrade (HL-LHC) and a non-collider program being revised in the PBC framework. The upgrade of the LHC and its injectors (LIU) will push the reachable peak luminosity in the LHC by almost an order of magnitude, while the SHiP experiment proposed in the PBC context require at least a factor two increase in the number of protons slowly extracted from the SPS per year.

One of the main limitations to the maximum achievable brightness in the SPS is the instability caused by impedance. The SPS kickers are among the main systems responsible for the impedance of the SPS. In this PhD work, the feasibility of halving the contribution from the extraction kickers by removing one of the two kicker systems of the SPS and extracting one beam by means of the non-local extraction scheme was demonstrated. The simulated set-up was reproduced in the SPS and the non-local extraction of LHC beam 1 was performed using the kicker normally used for beam 2. The non-local extraction is intrinsically more prone to shot-to-shot variations, but extrapolation from available data showed a transfer line trajectory stability very similar to the present local extraction. The main contribution to the stability was, in fact, shown to originate in the overall the machine reproducibility and not from the extraction technique itself. The main drawback of this concept is in the complexity of the machine interlock strategy, which should be completely changed due to the necessity to extract two beams with the same energy with the same kicker system, via two different and widely-separated septa systems.

To properly protect the LHC machine components from the higher energy in the HL-LHC beams at injection, upgrades of different protection devices are needed. Two of those are the TL collimators and the LHC injection protection system. The TL collimators will be upgraded to protect the LHC against the 60 MJ beam transported in the TLs. Such devices are being redesigned and the optics of the lines rematched to accommodate the hardware changes and satisfy the protection requirements. In order to validate the TCDI jaw positions and gaps, an accurate and reliable method was required. Also, to

reduce the setting-up time, the present eight hours needed for such procedure had to be reduced. This thesis presents the simulation tools and the developed new methods, based on particle tracking. The new method relies on more accurate and faster calibration of the BLM readings, the use of real TL trajectories and direct comparison with tracking simulations. The new method demonstrated a faster set-up validation (by about a factor three) and much more sensitivity to jaw position errors (for example, an error in the validation measurements during the 2014 LHC commissioning was found and solved). This new methodology can now be used for future TCDI set-up validation. An operational tool was also developed, to make this procedure completely automatic and a first version is already available.

In addition to the upgrades of the HL-LHC injection system to cope with the new beam parameters, a revision of the criterion and tolerances used to evaluate the LHC apertures has been made, taking account of the measurements made in LHC Run 1. The new criteria exploit tracking simulations of the most critical loss scenarios to establish the maximum halo amplitude with an intensity above a safe limit defined as 25 % the damage limit. In this thesis, simulations of the critical injection system failures were carried out and the new proposed hardware changes evaluated. The expected load on different protection devices was also calculated. From this, it is concluded that the proposed changes will permit to keep the design protection level and the protection devices themselves will not be damaged in case of injection failures. Finally, the calculated minimum protected aperture from the injection protection system was calculated as $8.7\,\sigma$, which remains below the $9\,\sigma$ limit defined by the asynchronous beam dump scenario [51].

For the non-collider program the proposed SHiP FT experiment at the SPS will request an unprecedented 4×10^{19} protons per year, four times higher than ever achieved for the slow extraction from LSS2. For this to be feasible a significant reduction of the extraction losses has to be achieved. As an initial step the SPS slow extraction was reviewed, a model was developed and a very close agreement with beam measurements achieved.

To gain a factor of four in losses at the electrostatic septum, the novel concept of crystal assisted non-local extraction was conceived. Such a concept merges together the non-local extraction methodology, channelling process in silicon bent crystals and the resonant third-integer slow extraction. Taking advantage of the recent measurement campaigns on bent crystals, the SPS slow extraction model was adapted to include the first order physics of particle-crystal interactions. The simulated gain in terms of losses is very close to the aimed factor four, which makes this technique very promising. As the complexity of operating crystals in a resonant regime is non negligible, experimental studies are needed to conclude on the real performance reach. A first step towards the crystal assisted non-local resonant slow extraction experiment was made by benchmarking the model with measurements. The model reproduced the measurements very accurately. In the first performed beam test particles were not physically extracted due to machine protection

precautions. Nevertheless, the achieved results gave confidence in the experimental set-up and simulation model. Studies are already ongoing to benchmark the simulations with other known codes (e.g. SixTrack). The main uncertainty of the simulations presented here is in the beam-crystal interaction approximation. In the upcoming months, the complete crystal-assisted extraction in a non-resonant regime will be attempted. In the near future it is planned to develop and install a crystal, as specified in Chapter 6, for the crystal assisted non-local resonant slow extraction. These results can also help the ongoing research on the TeV-scale slow extraction, where the losses minimisation and aperture restrictions are the main concerns.

Bibliography

[1] C. Zannini, L. Rivkin, and G. Rumolo, *Electromagnetic Simulation of CERN accelerator Components and Experimental Applications.* PhD thesis, Ecole Polytechnique, Lausanne, Mar 2013. Presented 15 Apr 2013.

[2] F. M. Velotti, A. Alekou, W. Bartmann, E. Carlier, K. Cornelis, I. Efthymiopoulos, B. Goddard, L. K. Jensen, V. Kain, M. Kowalska, V. Mertens, and R. Steerenberg, "Non-local Fast Extraction from the CERN SPS at 100 and 440 GeV," *Conf. Proc.*, vol. C130512, p. MOPFI050. 4 p, Jul 2013.

[3] H. Bartosik, G. Iadarola, Y. Papaphilippou, G. Rumolo, B. Salvant, and C. Zannini, "TMCI thresholds for LHC single bunches in the CERN SPS and comparison with simulations," p. 4 p, Jun 2016.

[4] M. Fraser, O. Aberle, P. Bestmann, C. Bracco, F. Gleazzi, E. Gianfelice-Wendt, V. Kain, A. Kosmicki, F. Maciariello, M. Meddahi, F. Nuiry, J. Ferreira Somoza, G. Steele, F. Velotti, and H. Vinke, "Functional and Conceptual Design of TCDI Transfer Line Collimators for LIU Upgrade," Feb 2016.

[5] CERN, "Physics beyond colliders." PBC, https://indico.cern.ch/event/523655/, 2016.

[6] W. Bonivento, A. Boyarsky, H. Dijkstra, U. Egede, M. Ferro-Luzzi, B. Goddard, A. Golutvin, D. Gorbunov, R. Jacobsson, J. Panman, M. Patel, O. Ruchayskiy, T. Ruf, N. Serra, M. Shaposhnikov, and D. Treille, "Proposal to Search for Heavy Neutral Leptons at the SPS," Tech. Rep. CERN-SPSC-2013-024. SPSC-EOI-010, CERN, Geneva, Oct 2013.

[7] T. Asaka, S. Blanchet, and M. Shaposhnikov, "The νmsm, dark matter and neutrino masses," *Physics Letters B*, vol. 631, no. 4, pp. 151–156, 2005.

[8] T. Asaka and M. Shaposhnikov, "The νmsm, dark matter and baryon asymmetry of the universe," *Physics Letters B*, vol. 620, no. 1, pp. 17–26, 2005.

[9] S. Y. Lee, *Accelerator physics.* Singapore: World Scientific, 1999.

[10] A. W. Chao and M. Tigner, *Handbook of Accelerator Physics and Engineering.* Singapore: World Scientific, 1999.

Bibliography

[11] H. Wiedemann, *Particle accelerator physics; 3rd ed.* Berlin: Springer, 2007.

[12] H. Bartosik, Y. Papaphilippou, and M. Benedikt, *Beam dynamics and optics studies for the LHC injectors upgrade.* PhD thesis, TU Vienna, Oct 2013. Presented 13 Nov 2013.

[13] P. Muggli, E. Öz, R. Tarkeshian, C. Bracco, E. Gschwendtner, A. Pardons, A. Caldwell, O. Reimann, K. Lotov, A. Pukhov, J. Vieira, and M. Wing, "Physics of the AWAKE Project," p. TUPEA008. 3 p, 2013.

[14] L. Ducimetière, U. Jansson, G. Schröder, E. B. Vossenberg, M. J. Barnes, and G. D. Wait, "Design of the injection kicker magnet system for CERN's 14 TeV proton collider LHC," Tech. Rep. CERN-SL-95-80-BT. LHC-NOTE-337. TRI-PP-95-50. CERN-LHC-Note-337, CERN, Geneva, Aug 1995.

[15] M. Benedikt, *Optical design of a synchrotron with optimisation of the slow extraction for hadron therapy.* PhD thesis, Vienna, Tech. U., Geneva, 1997. Presented on Oct 1997.

[16] O. S. Brüning, P. Collier, P. Lebrun, S. Myers, R. Ostojic, J. Poole, and P. Proudlock, *LHC Design Report.* Geneva: CERN, 2004.

[17] G. Apollinari, I. Béjar Alonso, O. Brüning, M. Lamont, and L. Rossi, *High-Luminosity Large Hadron Collider (HL-LHC): Preliminary Design Report.* Geneva: CERN, 2015.

[18] C. Bracco, R. Assmann, and L. Rivkin, *Commissioning Scenarios and Tests for the LHC Collimation System.* PhD thesis, Ecole Polytechnique, Lausanne, Lausanne, 2009. Presented on 29 Jan 2009.

[19] J. Wenninger, "CNGS Extraction and Transfer Stability in 2007," Tech. Rep. CERN-AB-2008-002, CERN, Geneva, 2008.

[20] Y. Papaphilippou, "SPS Observations," tech. rep., CERN, Geneva, 2013.

[21] W. Scandale, G. Arduini, R. Assmann, C. Bracco, S. Gilardoni, V. Ippolito, E. Laface, R. Losito, A. Masi, E. Metral, V. Previtali, S. Redaelli, M. Silari, L. Tlustos, E. Bagli, S. Baricordi, P. Dalpiaz, V. Guidi, A. Mazzolari, D. Vincenzi, G. D. Mea, A. Lombardi, D. D. Salvador, E. Vallazza, D. Bolognini, S. Hasan, D. Lietti, V. Mascagna, A. Mattera, M. Prest, G. Cavoto, L. Ludovici, D. Mirarchi, R. Santacesaria, P. Valente, F. Murtas, A. Afonin, Y. Chesnokov, V. Maisheev, I. Yazynin, A. Kovalenko, A. Taratin, A. Denisov, Y. Gavrikov, Y. Ivanov, L. Lapina, L. Malyarenko, V. Skorobogatov, V. Suvorov, S. Vavilov, N. Mokhov, D. Still, G. Robert-Demolaize, T. Markiewicz, and M. Oriunno, "First results on the sps beam collimation with bent crystals," *Physics Letters B*, vol. 692, no. 2, pp. 78 – 82, 2010.

136

[22] L. Drosdal, V. Kain, and S. Stapnes, *LHC Injection Beam Quality During LHC Run I*. PhD thesis, Oslo U., Mar 2015. Presented 24 Aug 2015.

[23] V. Kain, O. S. Brüning, L. Ducimetière, B. Goddard, M. Lamont, and V. Mertens, "The Expected Performance of the LHC Injection Protection System," no. LHC-Project-Report-746. CERN-LHC-Project-Report-746, p. 4 p, 2004. revised version submitted on 2004-09-23 10:48:42.

[24] L. Drosdal, W. Bartmann, H. Bartosik, C. Bracco, E. Gianfelice, B. Goddard, V. Kain, Y. Papaphilippou, J. Uythoven, and J. Wenninger, "Analysis of LHC transfer line trajectory drifts," no. FERMILAB-CONF-13-125-APC, p. 3 p, 2013.

[25] L. Drøsdal, C. Bracco, K. Cornelis, B. Goddard, V. Kain, M. Meddahi, J. Wenninger, and E. Gianfelice-Wendt, "Investigations of SPS orbit drifts," p. 4 p, Jun 2014.

[26] E. Gianfelice Wendt, H. Bartosik, K. Cornelis, L. Norderhaug Drosdal, B. Goddard, V. Kain, M. Meddahi, Y. Papaphilippou, and J. Wenninger, "SPS Beam Steering for LHC Extraction," p. 3 p, Sep 2014.

[27] J. Irwin, C. Wang, Y. T. Yan, K. L. Bane, Y. Cai, F.-J. Decker, M. G. Minty, G. V. Stupakov, and F. Zimmermann, "Model-independent beam dynamics analysis," *Physical review letters*, vol. 82, no. 8, p. 1684, 1999.

[28] W. Herr, "Diffusion of particles induced by transverse noise and its application to crystal extraction experiments," Tech. Rep. CERN-SL-92-53-AP, CERN, Geneva, Nov 1992.

[29] H. Akbari, X. Altuna, S. Bardin, R. Bellazzini, V. M. Biryukov, A. Brez, M. P. Bussa, L. Busso, A. Calcaterra, G. Carboni, F. Costantini, R. De Sangro, K. Elsener, F. Ferioli, A. Ferrari, G. Ferri, F. Ferroni, G. Fidecaro, A. Freund, R. Guinand, M. Gyr, W. Herr, A. Hilaire, B. N. Jensen, J. T. Klem, L. Lanceri, K. Maier, M. M. Massai, V. Mertens, S. P. Møller, S. Morganti, O. Palamara, S. Péraire, S. Petrera, M. Placidi, R. Santacesaria, W. Scandale, R. Schmidt, A. M. Taratin, F. Tosello, E. Uggerhøj, B. Vettermann, P. F. Vita, G. Vuagnin, E. Weisse, and S. Weisz, "First results on proton extraction from the CERN-SPS with a bent crystal," *Phys. Lett. B*, vol. 313, pp. 491–497. 14 p, Jun 1993.

[30] K. Elsener, G. Fidecaro, M. Gyr, W. Herr, J. T. Klem, U. Mikkelsen, S. P. Weisse, S. P. Møller, E. Uggerhøj, and G. Vuagnin, "Proton extraction from the CERN SPS using a bent crystal," Tech. Rep. CERN-SL-95-88-AP, CERN, Geneva, Oct 1995.

[31] K. Elsener, G. Fidecaro, M. Gyr, W. Herr, J. T. Klem, U. Mikkelsen, and E. Weisse, "What did we learn from the extraction experiments with bent crystals at the CERN SPS?," p. 3 p, Jun 1998.

[32] UA9, "ColUSM - H8 Single Pass Test Data Analysis," 2014. https://lhc-collimation-upgrade-spec.web.cern.ch/lhc-collimation-upgrade-spec/H8_input.php#2d.

[33] R. Rossi, "Measurements of coherent interactions in silicon bent crystals with 400 gev proton at cern h8," in *Channeling 2014*, 2014.

[34] W. Scandale, G. Arduini, R. Assmann, C. Bracco, F. Cerutti, J. Christiansen, S. Gilardoni, E. Laface, R. Losito, A. Masi, E. Metral, D. Mirarchi, S. Montesano, V. Previtali, S. Redaelli, G. Valentino, P. Schoofs, G. Smirnov, L. Tlustos, E. Bagli, S. Baricordi, P. Dalpiaz, V. Guidi, A. Mazzolari, D. Vincenzi, S. Dabagov, F. Murtas, A. Carnera, G. D. Mea, D. D. Salvador, A. Lombardi, O. Lytovchenko, M. Tonezzer, G. Cavoto, L. Ludovici, R. Santacesaria, P. Valente, F. Galluccio, A. Afonin, M. Bulgakov, Y. Chesnokov, V. Maisheev, I. Yazynin, A. Kovalenko, A. Taratin, V. Uzhinskiy, Y. Gavrikov, Y. Ivanov, L. Lapina, V. Skorobogatov, W. Ferguson, J. Fulcher, G. Hall, M. Pesaresi, M. Raymond, A. Rose, M. Ryan, O. Zorba, G. Robert-Demolaize, T. Markiewicz, M. Oriunno, and U. Wienands, "Comparative results on collimation of the sps beam of protons and pb ions with bent crystals," *Physics Letters B*, vol. 703, no. 5, pp. 547 – 551, 2011.

[35] W. Scandale, G. Arduini, R. Assmann, F. Cerutti, S. Gilardoni, E. Laface, R. Losito, A. Masi, E. Metral, D. Mirarchi, S. Montesano, V. Previtali, S. Redaelli, G. Valentino, P. Schoofs, G. Smirnov, E. Bagli, S. Baricordi, P. Dalpiaz, V. Guidi, A. Mazzolari, D. Vincenzi, S. Dabagov, F. Murtas, G. Claps, G. Cavoto, F. Iacoangeli, L. Ludovici, R. Santacesaria, P. Valente, F. Galluccio, A. Afonin, M. Bulgakov, Y. Chesnokov, V. Maisheev, I. Yazynin, A. Kovalenko, A. Taratin, V. Uzhinskiy, Y. Gavrikov, Y. Ivanov, L. Lapina, V. Skorobogatov, W. Ferguson, J. Fulcher, G. Hall, M. Pesaresi, M. Raymond, A. Rose, M. Ryan, G. Robert-Demolaize, T. Markiewicz, M. Oriunno, and U. Wienands, "Strong reduction of the off-momentum halo in crystal assisted collimation of the sps beam," *Physics Letters B*, vol. 714, no. 2–5, pp. 231 – 236, 2012.

[36] G. Arduini, M. Calviani, K. Cornelis, L. Gatignon, B. Goddard, A. Golutvin, R. Jacobsson, J. Osborne, R. Roesler, T. Ruf, H. Vincke, and H. Vincke, "A new Experiment to Search for Hidden Particles (SHIP) at the SPS North Area," Tech. Rep. EN-DH-2014-007, CERN, Geneva, 2014.

[37] V. Kain, K. Cornelis, and E. Effinger, "New spill control for the slow extraction in the multi-cycling sps," *Proceedings of IPAC2016*, 2016.

[38] T. P. R. Linnecar, "The high frequency longitudinal and transverse pick-ups used in the sps," *IEEE Trans. Nucl. Sci.*, vol. 26, no. CERN-SPS-ARF-78-17, pp. 3409–3411, 1978.

[39] F. Velotti, C. Bracco, K. Cornelis, L. Drøsdal, M. Fraser, E. Gianfelice-Wendt, B. Goddard, V. Kain, and M. Meddahi, "Analysis of the SPS Long Term Orbit

Drifts," no. FERMILAB-CONF-16-243-APC. CERN-ACC-2016-135, p. THPOR054. 4 p, 2016.

[40] M. Giovannozzi, D. Quatraro, and G. Turchetti, "Generating unstable resonances for extraction schemes based on transverse splitting," *Phys. Rev. ST Accel. Beams*, vol. 12, p. 024003, Feb 2009.

[41] W. Scandale, R. Losito, M. Silari, E. Bagli, S. Baricordi, P. Dalpiaz, M. Fiorini, V. Guidi, A. Mazzolari, D. Vincenzi, R. Milan, G. D. Mea, E. Vallazza, A. Afonin, Y. Chesnokov, V. Maisheev, I. Yazynin, S. Afanasiev, A. Kovalenko, A. Taratin, V. Uzhinsky, A. Denisov, Y. Gavrikov, Y. Ivanov, L. Lapina, L. Malyarenko, V. Skorobogatov, V. Suvorov, S. Vavilov, D. Bolognini, S. Hasan, and M. Prest, "Probability of inelastic nuclear interactions of high-energy protons in a bent crystal," *Nuclear Instruments and Methods in Physics Research Section B: Beam Interactions with Materials and Atoms*, vol. 268, no. 17–18, pp. 2655 – 2659, 2010.

[42] J. B. Jeanneret and T. Risselada, "Geometrical Aperture in LHC at Injection," Tech. Rep. LHC-Project-Note-66, CERN, Geneva, Sep 1996.

[43] J. B. Jeanneret and R. Ostokic, "Geometrical Acceptance in LHC Version 5.0," Tech. Rep. LHC-Project-Note-111, CERN, Geneva, Sep 1997.

[44] C. Alabau Pons, M. Giovannozzi, G. Muller, S. Redaelli, F. Schmidt, R. Tomas, and J. Wenninger, "LHC Aperture Measurements. First beam-based aperture measurements in the arcs of the CERN Large Hadron Collider," p. 3 p, Jun 2010.

[45] C. Alabau Pons, R. Assmann, R. Bruce, M. Giovannozzi, E. Maclean, G. Mueller, S. Redaelli, F. Schmidt, R. Tomas, and J. Wenninger, "IR1 and IR5 aperture at 3.5 TeV," Nov 2011.

[46] R. W. Assmann, R. Bruce, M. del Carmen Alabau, M. Giovannozzi, G. Muller, S. Redaelli, F. Schmidt, R. Tomas, J. Wenninger, and D. Wollmann, "Aperture Determination in the LHC Based on an Emittance Blowup Technique with Collimator Position Scan," p. 3 p, Sep 2011.

[47] S. Redaelli, C. Alabau Pons, R. Assmann, R. Bruce, M. Giovannozzi, G. Muller, and J. Wenninger, "Aperture measurements in the LHC interaction regions," *Conf. Proc.*, vol. C1205201, p. MOPPD062. 3 p, May 2012.

[48] C. Alabau Pons, A. Arduini, R. Assmann, R. Bruce, M. Giovannozzi, J. M. Jowett, E. MacLean, G. Muller, S. Redaelli, R. Tomas, G. Valentino, and J. Wenninger, "IR2 aperture measurements at 3.5 TeV," Feb 2012.

[49] R. Bruce, M. Giovannozzi, P. D. Hermes, B. Holzer, A. A. Nosych, S. Redaelli, and J. Wenninger, "IR8 Aperture Measurements at injection energy," Apr 2013.

[50] R. Bruce, H. Garcia Morales, P. D. Hermes, R. Kwee-Hinzmann, A. Mereghetti, D. Mirarchi, S. Redaelli, B. M. Salvachua Ferrando, P. K. Skowronski, G. Valentino, and A. Valloni, "IR aperture measurement at β^*=40 cm," Sep 2015.

[51] R. Bruce, C. Bracco, M. Giovannozzi, S. Redaelli, R. Tomas, F. Velotti, and J. Wenninger, "Parameters for aperture calculations at injection," Mar 2016.

[52] R. Bruce, R. De Maria, S. Fartoukh, M. Giovannozzi, S. Redaelli, R. Tomas, and J. Wenninger, "Parameters for HL-LHC aperture calculations and comparison with aperture measurements," Tech. Rep. CERN-ACC-2014-0044, CERN, Geneva, Mar 2014.

[53] G. Robert-Démolaize and R. W. Assmann, *Design and Performance Optimization of the LHC Collimation System*. PhD thesis, Joseph Fourier U., Grenoble, 2006. Presented on 20 Nov 2006.

[54] R. Bruce, R. W. Assmann, V. Boccone, C. Bracco, M. Brugger, M. Cauchi, F. Cerutti, D. Deboy, A. Ferrari, L. Lari, A. Marsili, A. Mereghetti, D. Mirarchi, E. Quaranta, S. Redaelli, G. Robert-Demolaize, A. Rossi, B. Salvachua, E. Skordis, C. Tambasco, G. Valentino, T. Weiler, V. Vlachoudis, and D. Wollmann, "Simulations and measurements of beam loss patterns at the CERN Large Hadron Collider," *Phys. Rev. Spec. Top. Accel. Beams*, vol. 17, p. 081004. 16 p, Sep 2014.

[55] D. Wollmann, "Multi-turn losses and cleaning," 2010.

[56] G. Valentino, R. W. Assmann, G. Bellodi, R. Bruce, F. Burkart, M. Cauchi, D. Deboy, J. M. Jowett, L. Lari, S. Redaelli, A. Rossi, B. Salvachua Ferrando, and D. Wollmann, "Multi-turn losses and cleaning in 2011 and 2012," 2012.

[57] V. K. Verena Kain and R. Rudiger Schmidt, *Machine Protection and Beam Quality during the LHC Injection Process*. PhD thesis, Vienna Tech. U., Viena, 2005. Presented on 14 Oct 2005.

[58] L. Drøsdal, K. Cornelis, B. Goddard, V. Kain, M. Meddahi, O. Mete, B. Salvachua, G. Valentino, and E. Veyrunes, "SPS Scraping and LHC Transverse Tails,"

[59] J. e. a. Holmes, "Objective Ring Beam Injection and Tracking Code," tech. rep., BNL.

[60] N. Catalan-Lasheras, *Transverse and Longitudinal Beam Collimation in a High-Energy Proton Collider (LHC)*. PhD thesis, Zaragoza U., Geneva, 1998. Presented on 16 Nov 1998.

[61] G. Robert-Démolaize and R. W. Assmann, *Design and Performance Optimization of the LHC Collimation System*. PhD thesis, Joseph Fourier U., Grenoble, 2006. Presented on 20 Nov 2006.

[62] C. Tambasco, S. Redaelli, M. B. Salvachua Ferrando, and G. Cavoto, *An improved scattering routine for collimation tracking studies at LHC*. PhD thesis, Rome U., Dec 2014. Presented 21 Jan 2014.

[63] C. Bracco, W. Bartmann, M. J. Barnes, E. Carlier, L. N. Drosdal, B. Goddard, V. Kain, M. Meddahi, V. Mertens, and J. Uythoven, "Injection and Dump Systems," 2012.

[64] A. Lechner, A. Alnuaimi, C. Bracco, F. Cerutti, A. Christov, L. S. Esposito, N. V. Shetty, and V. Vlachoudis, "Energy Deposition Studies for Fast Losses during LHC Injection Failures," *Conf. Proc.*, vol. C130512, p. TUPFI027. 4 p, May 2013.

[65] C. Bracco, W. Bartmann, M. J. Bednarek, E. Nebot Del Busto, B. Goddard, E. B. Holzer, A. Nordt, M. Sapinski, R. Schmidt, M. Solfaroli Camillocci, and M. Zerlauth, "Experiments on the margin of beam induced quenches a superconducting quadrupole magnet in the LHC," *Conf. Proc.*, vol. C1205201, p. MOPPC004. 5 p, Aug 2012.

[66] B. Goddard, M. Gyr, J. B. Jeanneret, V. Kain, M. Lamont, V. Maire, V. Mertens, and J. Wenninger, "Aperture and Delivery Precision of the LHC Injection System," p. 4 p, Aug 2004. revised version submitted on 2004-09-23 11:07:49.

Acknowledgements

First, I would like to thank my CERN supervisor Chiara Bracco. I want to thank her for choosing me as her student, for proposing me a very interesting and wide topic, for guiding me in this long and tortuous path, for the everyday discussions, for every advice and for the countless time she has read these pages. I could not have been luckier.

I sincerely thank my EPFL supervisor Leonid Rivkin for accepting me as his student, for his wise guidance and for giving me the possibility to join EPFL for these years.

Thanks to Brennan Goddard who first brought me here at CERN and gave me the chance to discover this incredible and deeply interesting world of accelerator physics. I really thank him especially for what I have learnt from him, for all the advices, suggestions, incredible ideas and rugby discussions. Also, thank you, Brennan, to manage to find the time to read this thesis.

I would like to thank my section leader Malika Meddahi, Wolfgang Bartmann and the all BTP section for their support in these years. I especially want to thank Matthew Fraser for actively participating at my supervision and for his ideas, discussions, suggestions and of course for reading this thesis.

During all the MD and commissioning time, the help of the LHC and especially the SPS operation crew has been fundamental. A special thanks to Verena Kain and Karel Cornelis for helping me learning to know and love (a lot) such an incredible machine as the SPS.

I thank all the ABT colleagues: Mike Barnes, Etienne Carlier, Jan Borburgh, Nicolas Magnin, Viliam Senaj and Thomas Kramer for showing me the beauty of the extraction/injection systems hardware.

I would like to thank the colleagues of the collimation team, Roderik Bruce and Stefano Redaelli, for the help and discussions regarding the HL-LHC injection studies. Also, thanks to the UA9 collaboration colleagues, especially Walter Scandale, Simone Montesano and Francesca Addesa, for their indispensable expertise put in for the crystal-related studies. Of course, I would like also to thank the colleague of the EN/STI group, Francesco Cerutti and Anton Lechner.

Now, I would like to profit to finally thank all the friends that I had the luck to have around during these years, and especially: Sara (thanks for making the thesis writing a bit less horrible), Charlie (thanks for the help with the French abstract and everything

Acknowledgements

else), Matteo (thanks for listening to all my complains), Nik (thanks for the fika and kanelbullar) and Justin (thanks for trying to teach me some English and coding). Infine, ma solo per ragioni di simmetria, vorrei ringraziare la mia famiglia tutta, soprattutto Giovanni e Kent, per l'enorme sostegno sempre dimostratomi.

Francesco

Francesco M. **Velotti**

Rue de la Prairie, 15, 1202 Geneve, Switzerland

(+41) 787454715 | francesco.velotti@me.com | fvelotti

Education and Academic Experience

Senior fellow at CERN in the operation group *Geneve, Switzerland*

CERN *2016 - Present*

- Operation of the CERN Super Proton Synchrotron

Ph.D. in Accelerator Physics *Lausanne, Switzerland*

École Polytechnique Fédérale De Lausanne (EPFL) and CERN *Jul. 2013 - Jan. 2017*

- Thesis title: "Higher brightness beams from SPS as an injector for HL-LHC upgrade"
- EPFL Advisor: Prof. L. Rivkin;
- CERN Supervisor: Dr. C. Bracco

Teaching assistant of the Master course "Introduction to Particle Accelerators" *Lausanne, Switzerland*

École Polytechnique Fédérale De Lausanne (EPFL) *Sept. 2015 - Jan. 2016*

Preparation and supervision of class tutorials, MADX tutorials and final exam for post-graduate students

Technical Studentship *Geneve, Switzerland*

CERN, affiliated with Università degli Studi del Sannio *2012 - 2013*

- CERN Supervisor: Dr. B. Goddard
- Beam dynamics projects:
    - Review and upgrade studies of the SPS internal dump system
    - Studies of feasibility of non-local extraction from SPS
    - Upgrade of the SPS ion injection system
    - Design of the AWAKE electron beam line

Master of Science in Electronic Engineering for Telecommunications and Automation - grade 110/110 with honours *Benevento, Italy*

Università degli Studi del Sannio *2010 - 2012*

- Thesis title (carried on at CERN): "Non-local Fast Extraction from the SPS"
- University Advisor: Prof. S. Petracca;
- CERN Supervisor: Dr. B. Goddard

Erasmus Programme *Gothenburg, Sweden*

Chalmers University of Technology *Jan. 2010 - Jul. 2010*

Bachelor of Science in Telecommunication Engineering - grade 110/110 *Benevento, Italy*

Università degli Studi del Sannio *2005 - 2009*

- Thesis title (carried on at INFN): "Effect of the Electron Could on the Particle Beam Dynamics in Accelerators"
- University Advisor: Prof. S. Petracca
- INFN Supervisor: Dr. T. Demma

High School in Science - grade 100/100 *Benevento, Italy*

Istituto Magistrale Guacci (Liceo Scientifico Tecnologico prog. Brocca) *2000 - 2005*

Technical Skills

Accelerator Physics

- Transfer lines and rings lattice design: high and intermediate energy (hadrons and electrons)
- Extraction and injection systems design: single-turn injection and extraction, slow resonant and non-resonant extraction, crystal assisted extraction, non-local extraction
- Operation of high-energy accelerators
- Particle tracking simulations: linear and non-linear dynamics, collimation (Monte Carlo particle tracking inside matter), extraction, injection and beam transport
- Data analysis of standard and non-standard beam behaviour: analysis of closed orbit variations, damage of machine components, beam based measurements
- Machine protection system design: beam dump system (SPS, LHC, FCC)
- Collective effects: electron cloud, space charge
- RF systems measurements

Telecommunication Engineering

- Multimedia and video communication system design: satellite systems, compression algorithms, data and signal processing, mobile device networks, WiFi networks
- Radar system design: tomography, signal propagations
- Microwave devices design: Chebyshev transformer, multi-port devices
- Antenna design

Simulations and Numerical Analysis Tools

- **Accelerator Physics:** MADX (MADX-PTC), PTC-ORBIT (PyOrbit), PyCollimate for MADX and MADX-PTC, SixTrack, Trace3D
- **General physics:** ANSOFT Designer, Sonnet, COMSOL, Simulink
- **General Data Analysis:** Python (numpy, matplotlib, pandas), Mathematica, Matlab, Mathcad
- **Programming Language:** Python, C, C++, Java, Fortran, Bash
- **OS:** Linux, Mac OS, Windows
- **Documentation Tools:** Latex, Mac suite (Keynote, Pages, Numbers), Microsoft Office suite

Miscellaneous

Meeting Organisation

- Scientific secretary of the "LIU-SPS Beam loss, protection and transfer lines Working Group" meetings. Chaired by V. Kain;
- Scientific secretary of the "Fast extraction from LSS2 - SPS" meetings. Chaired by B. Goddard;

International Particle Accelerator Conference 2015

- Awarded with Student Scholarship

Languages

Italian	Native Language
English	Full professional proficiency
French	Intermediate
Spanish	Beginner

Courses and Trainings

2015	**CERN Accelerator School**, Advanced Accelerator Physics	*Warsaw, Poland*
2014	**Joint International Accelerator School (JAS)**, Beam Loss and Accelerator Protection	*Newport Beach, California (USA)*
2013	**United States Particle Accelerator School (USPAS)**, Fundamentals of Accelerator Physics and Technology with Simulations and Measurements Lab	*Fort Collins, Colorado (USA)*
2015	**CERN Course**, Advanced Hands-on: Python	*Geneve, Switzerland*
2015	**CERN Course**, Making Engaging Presentations	*Geneve, Switzerland*

Invited Talks

2015	**Tracking for Collimation Workshop**, Injection protection studies for HL-LHC	*CERN, Switzerland*
2015	**5th Joint HiLumi LHC-LARP Annual Meeting 2015**, Aperture and protection tolerance for the injection into HL-LHC	*CERN, Switzerland*
2015	**Machine Studies Working Group Meeting (MSWG)**, SPS tune-orbit stability	*CERN, Switzerland*
2013	**AWAKE Collaboration meeting**, Electron beam-line design	*CERN, Switzerland*

Publications

[1] FM Velotti, C Bracco, O Aberle, M Meddahi, J Uythoven, P Chiggiato, JA Ferreira Somoza, B Goddard, E Carlier, and V Senaj. Performance improvements of the sps internal beam dump for the hl-lhc beam. In *Conf. Proc.*, volume 130512, page THPEA041, 2013.

[2] FM Velotti, C Bracco, M Meddahi, K Cornelis, W Bartmann, B Goddard, V Kain, and E Carlier. Feasibility studies for the extraction of both lhc beams from cern sps using a common kicker. Technical report, 2014.

[3] Francesco Velotti, Wolfgang Bartmann, Chiara Bracco, Matthew Fraser, Brennan Goddard, Verena Kain, Anton Lechner, and Malika Meddahi. The new hl-lhc injection and transport protection system. In *57th ICFA Advanced Beam Dynamics Workshop on High-Intensity and High-Brightness Hadron Beams (HB'16), Malmö, Sweden, July 3-8, 2016*, pages 81–86. JACOW, Geneva, Switzerland, 2016.

[4] Francesco Velotti, Matthew Fraser, Karel Cornelis, Chiara Bracco, Brennan Goddard, Wolfgang Bartmann, Verena Kain, Linda Stoel, and Thomas Bohl. Characterisation of the sps slow-extraction parameters. 2016.

[5] Francesco Velotti, Matthew Fraser, Karel Cornelis, Malika Meddahi, Chiara Bracco, Lene Drøsdal, Brennan Goddard, Verena Kain, and Eliana Gianfelice-Wendt. Analysis of the sps long term orbit drifts. Technical report, 2016.

[6] Francesco Maria Velotti, Thomas Kramer, and Jan Uythoven. Transverse emittance blow-up of the heavy ion beam injected into the sps from the proposed msi-v septum. Technical report, 2014.

[7] Francesco Velotti, Ramon Folch, John Osborne, Francesco Cerutti, Viliam Senaj, Karel Cornelis, Malika Meddahi, Jose Luis Abelleira, Chiara Bracco, Brennan Goddard, et al. Feasibility study of a new sps beam dump system. 2015.

[8] FM Velotti, M Kowalska, K Cornelis, LK Jensen, I Efthymiopoulos, W Bartmann, R Steerenberg, B Goddard, V Mertens, A Alekou, et al. Non-local fast extraction from the cern sps at 100 and 440 gev. In *Conf. Proc.*, volume 130512, page MOPFI050, 2013.

[9] Francesco Velotti, Matthew Fraser, Malika Meddahi, Chiara Bracco, Brennan Goddard, Wolfgang Bartmann, and Verena Kain. Sps-to-lhc transfer lines loss map generation using pycollimate. 2015.

[10] FM Velotti, C Bracco, O Aberle, L Ducimetiere, K Cornelis, M Meddahi, R Losito, F Pasdeloup, GE Steele, F Cerutti, et al. Performance studies of the sps beam dump system for hl-lhc beams. Technical report, 2014.

[11] SK Agarwalla, L Agostino, M Aittola, A Alekou, B Andrieu, F Antoniou, R Asfandiyarov, D Autiero, O Bésida, A Balik, et al. Optimised sensitivity to leptonic cp violation from spectral information: the lbno case at 2300 km baseline. *arXiv preprint arXiv:1412.0593*, 2014.

[12] Chiara Bracco, Edda Gschwendtner, Alexey Petrenko, Helga Timko, Theodoros Argyropoulos, Hannes Bartosik, Thomas Bohl, Juan Esteban Müller, Brennan Goddard, Malika Meddahi, et al. Beam studies and experimental facility for the awake experiment at cern. *Nuclear Instruments and Methods in Physics Research Section A: Accelerators, Spectrometers, Detectors and Associated Equipment*, 740:48–53, 2014.

[13] Brennan Goddard, T Argyropoulos, H Bartosik, W Bartmann, T Bohl, F Caspers, K Cornelis, H Damerau, L Drøsdal, L Ducimetière, et al. Progress with the upgrade of the sps for the hl-lhc era. *arXiv preprint arXiv:1409.5821*, 2014.

[14] LAGUNA-LBNO Collaboration, SK Agarwalla, L Agostino, M Aittola, A Alekou, B Andrieu, F Antoniou, R Asfandiyarov, D Autiero, O Bésida, et al. The lbno long-baseline oscillation sensitivities with two conventional neutrino beams at different baselines. *arXiv preprint arXiv:1412.0804*, 2014.

[15] C Bracco, E Gschwendtner, M Meddahi, FM Velotti, A Petrenko, and B Goddard. The challenge of interfacing the primary beam lines for the awake project at cern. Technical report, 2014.

[16] Verena Kain, Chiara Bracco, M Meddahi, Fausto Maciariello, G Steele, E Gianfelice-Wendt, B Goddard, A Mereghetti, and F Velotti. The new transfer line collimation system for the lhc high luminosity era. Technical report, 2014.

[17] V Kain, F Velotti, et al. Concerns with low emittance beam operation. *CERN Yellow Reports*, 2(00):176, 2016.

[18] Ö Mete, O Aberle, F Cerutti, K Cornelis, B Goddard, V Kain, R Losito, FL Maciariello, M Meddahi, J Uythoven, F Velotti, et al. Upgrades of the sps, transfer line and lhc injection protection devices for the hl-lhc era. *arXiv preprint arXiv:1409.5812*, 2014.

[19] Janet Schmidt, Owain Rhodri Jones, Patric Muggli, Matthew Fraser, Lars Jensen, Bartolomej Biskup, Edda Gschwendtner, Enrico Bravin, Alexey Vorozhtsov, Chiara Bracco, et al. The awake electron primary beam line. 2015.

[20] H Bartosik et al. Other means to increase the sps 25 ns performance–transverse plane. *CERN Yellow Reports*, 2(00):180, 2016.

[21] W Bartmann, M Kowalska, F Velotti, A Kosmicki, and B Goddard. Design study of a 100 gev beam transfer line from the sps for a short baseline neutrino facility. In *Conf. Proc.*, volume 130512, page MOPFI055, 2013.

[22] C Bracco, M Meddahi, G Le Godec, P Muggli, LK Jensen, A Kosmicki, J Bauche, C Mutin, H Vincke, K Papastergiou, et al. Beam transfer line design for a plasma wakefield acceleration experiment (awake) at the cern sps. In *Conf. Proc.*, volume 130512, page TUPEA051, 2013.

[23] T Kramer, L Sermeus, J Borburgh, J Uythoven, L Ducimetière, B Goddard, and FM Velotti. Upgrade of the sps injection kicker system for the lhc high luminosity operation with heavy ion beam. Technical report, 2014.

[24] M Fraser, E Gianfelice-Wendt, V Kain, F Velotti, and G Steele. Functional and conceptual design of tcdi transfer line collimators for liu upgrade. Technical report, SPU.

[25] A Caldwell, E Adli, L Amorim, R Apsimon, T Argyropoulos, R Assmann, A-M Bachmann, F Batsch, J Bauche, VK Berglyd Olsen, et al. Path to awake: Evolution of the concept. *Nuclear Instruments and Methods in Physics Research Section A: Accelerators, Spectrometers, Detectors and Associated Equipment*, 829:3–16, 2016.

[26] E Gschwendtner, C Bracco, M Meddahi, H Timko, E Shaposhnikova, A Pardons, B Goddard, H Vincke, and F Velotti. Feasibility study of the awake facility at cern. In *Conf. Proc.*, volume 130512, page TUPEA053, 2013.

[27] Magdalena Kowalska, Francesco M Velotti, Chiara Bracco, Marzio Nessi, Rende Steerenberg, Brennan Goddard, and Wolfgang Bartmann. Feasibility studies for 100 gev beam transfer lines for a cern neutrino facility. 2014.

[28] Jan Uythoven, Jean-Marc Cravero, Fausto Maciariello, Thomas Kramer, Jan Hansen, Django Manglunki, Jan Borburgh, Stephane Burger, Francois-Xavier Nuiry, Enrico Bravin, et al. Upgrade of the sps ion injection system. 2015.

[29] Wolfgang Bartmann, Janne Holma, Matthew Fraser, Linda Stoel, Malika Meddahi, Attilio Milanese, Thomas Kramer, Brennan Goddard, Werner Herr, Verena Kain, et al. Beam transfer to the fcc-hh collider from a 3.3 tev booster in the lhc tunnel. 2015.

[30] Vera Chetvertkova, Ruediger Schmidt, Francesco Velotti, and Daniel Wollmann. New method for validation of aperture margins in the lhc triplet. 2015.

[31] Mike Lamont, Paul Laycock, RS Thorne, Tomas Hreus, H Menjo, Tancredi Carli, Matthew Nguyen, Natalia Rossiyskaya, Sercan Sen, Roberto Covarelli, et al. Cern accelerating science. 2013.

[32] Thomas Kramer, Francesco Cerutti, Jan Borburgh, Linda Stoel, Brennan Goddard, Wolfgang Bartmann, Laurent Ducimetière, Francesco Velotti, Roberto Losito, Genevieve Steele, et al. Considerations for the beam dump system of a 100 tev centre-of-mass fcc hh collider. 2015.

[33] Jan Borburgh, Matthew Fraser, Cedric Baud, Fausto Maciariello, Verena Kain, Bruno Balhan, Genevieve Steele, Francesco Velotti, and Michael Barnes. Upgrade of the cern sps extraction protection elements tps. 2015.

[34] SK Agarwalla, L Agostino, M Aittola, A Alekou, B Andrieu, F Antoniou, R Asfandiyarov, D Autiero, O Bésida, A Balik, et al. Optimised sensitivity to leptonic cp violation from spectral information: the lbno case at 2300 km baseline. *arXiv preprint arXiv:1412.0593*, 2014.

[35] Sanjib Kumar Agarwalla, L Agostino, M Aittola, A Alekou, B Andrieu, D Angus, F Antoniou, A Ariga, T Ariga, R Asfandiyarov, et al. The mass-hierarchy and cp-violation discovery reach of the lbno long-baseline neutrino experiment. *Journal of High Energy Physics*, 2014(5):1–38, 2014.

[36] LAGUNA-LBNO Collaboration, SK Agarwalla, L Agostino, M Aittola, A Alekou, B Andrieu, F Antoniou, R Asfandiyarov, D Autiero, O Bésida, et al. Optimised sensitivity to leptonic cp violation from spectral information: the lbno case at 2300 km baseline. *arXiv preprint arXiv:1412.0593*, 2014.

[37] Chiara Bracco, Jennifer Jentzsch, Matthew Fraser, Nicolas Magnin, Jan Uythoven, Linda Stoel, Malika Meddahi, Jose Luis Abelleira, Lene Drøsdal, Brennan Goddard, et al. Lhc transfer lines and injection tests for run 2. 2015.

[38] V Kain, C Bracco, O Aberle, M Fraser, F Maciariello, FX Nuiry, A Kosmicki, E Gianfelice-Wendt, F Galleazzi, G Steele, et al. Changes to the transfer line collimation system for the high-luminosity lhc beams. Technical report, 2015.

[39] Anton Lechner, Chiara Bracco, Fausto Maciariello, Nikhil Vittal Shetty, Francesco Velotti, Antonio Perillo Marcone, Genevieve Steele, Jan Uythoven, Brennan Goddard, and Michael Barnes. Protection of superconducting magnets in case of accidental beam losses during hl-lhc injection. 2015.

[40] M Barnes, L Ducimetiere, T Kramer, L Sermeus, E Carlier, B Goddard, W Höfle, R Noulibos, G Kotzian, B Salvant, et al. Mkp-i kicker system.

[41] Jan Uythoven, Oscar Frasciello, Benoit Salvant, Luca Gentini, Chiara Bracco, Brennan Goddard, Nicolo Biancacci, Nikhil Vittal Shetty, Mikhail Zobov, Antonio Perillo Marcone, et al. Injection protection upgrade for the hl-lhc. Technical report, 2015.

[42] Genevieve Steele, Ramon Folch, Antonio Perillo-Marcone, Verena Kain, Cesare Maglioni, Roberto Losito, Florian Pasdeloup, Ivo Leitao, and Francesco Velotti. Comparison between measured and computed temperatures of the internal high energy beam dump in the cern sps. 2015.

[43] Verena Kain, Karel Cornelis, Malika Meddahi, Brennan Goddard, Mike Lamont, Cesare Maglioni, Roberto Losito, Florian Pasdeloup, Genevieve Steele, Ivo Leitao, et al. Origin of the damage to the internal high energy beam dump in the cern sps. 2015.

[44] JS Schmidt, J Bauche, B Biskup, C Bracco, S Doebert, B Goddard, E Gschwendtner, LK Jensen, OR Jones, S Mazzoni, et al. Status of the proton and electron transfer lines for the awake experiment at cern. *Nuclear Instruments and Methods in Physics Research Section A: Accelerators, Spectrometers, Detectors and Associated Equipment*, 829:58–62, 2016.

[45] RM Margineanu, B Andrieu, A Mefodiev, A Balik, T Hasegawa, P Kuusiniemi, E Shaposhnikova, G Vankova-Kirilova, F Sanchez-Galan, A Gendotti, et al. The lbno long-baseline oscillation sensitivities with two conventional neutrino beams at different baselines. Technical report, 2014.

[46] Alvaro Ferrero Colomo, Peter Burkel, Thomas Kramer, Denis Comte, Laurent Ducimetière, Francesco Velotti, Viliam Senaj, and Luc Sermeus. Feasibility study of the fast sps ion injection kicker system. 2016.

[47] Brennan Goddard, Laurent Ducimetière, Gerd Kotzian, Etienne Carlier, Jan Uythoven, and Francesco Velotti. Sps injection and beam quality for lhc heavy ions with 150 ns kicker rise time. 2016.

[48] C Bracco, LD Amorim, R Assmann, F Batsch, R Bingham, G Burt, B Buttenschön, A Butterworth, A Caldwell, S Chattopadhyay, et al. Awake: a proton-driven plasma wakefield acceleration experiment at cern. *Nuclear and Particle Physics Proceedings*, 273:175–180, 2016.

[49] Matthew Fraser, Nicolas Magnin, Chiara Bracco, Brennan Goddard, Wolfgang Bartmann, Verena Kain, Francesco Velotti, Jan Uythoven, and Etienne Carlier. A beam-based measurement of the lhc beam dump kicker waveform. 2016.

[50] Michael Barnes, Antonios Adraktas, Lorena Vega Cid, Thomas Kramer, Giuseppe Bregliozzi, Hugo Day, Luc Sermeus, Carlo Zannini, Chiara Pasquino, Jose Ferreira Somoza, et al. Studies of impedance-related improvements of the sps injection kicker system. 2016.

[51] Verena Kain, Raffaele Esposito, Malika Meddahi, Matthew Fraser, Brennan Goddard, Francesco Velotti, Antonio Perillo Marcone, and Genevieve Steele. Upgrades to the sps-to-lhc transfer line beam stoppers for the lhc high-luminosity era. 2016.

[52] C Bracco, J Coupard, H Damerau, A Funken, B Goddard, K Hanke, AM Lombardi, D Manglunki, S Mataguez, M Meddahi, F Velotti, et al. Lhc injectors upgrade for the hllhc. *Proc. HB'16*, 2016.

[53] Roderik Bruce, Stefano Redaelli, Rogelio Tomas Garcia, Chiara Bracco, Massimo Giovannozzi, Riccardo De Maria, Francesco Maria Velotti, and Jorg Wenninger. Parameters for aperture calculations at injection for hl-lhc. Technical report, 2016.

[54] Wolfgang Bartmann, Mike Barnes, Linda Stoel, Gerd Kotzian, Christoph Wiesner, Francesco Maria Velotti, and Vasileios Vlachodimitropoulos. Measurement report on the lhc injection kicker ripple denition and maximum pulse length (md 1268). Technical report, 2016.